

2012-01-01

# Development Of Nanocomposites For Energy Storage Devices

Md Ashiqur Rahaman Khan

University of Texas at El Paso, ashik.me05@gmail.com

Follow this and additional works at: [https://digitalcommons.utep.edu/open\\_etd](https://digitalcommons.utep.edu/open_etd)

 Part of the [Materials Science and Engineering Commons](#), [Mechanics of Materials Commons](#), and the [Nanoscience and Nanotechnology Commons](#)

---

## Recommended Citation

Khan, Md Ashiqur Rahaman, "Development Of Nanocomposites For Energy Storage Devices" (2012). *Open Access Theses & Dissertations*. 2121.

[https://digitalcommons.utep.edu/open\\_etd/2121](https://digitalcommons.utep.edu/open_etd/2121)

This is brought to you for free and open access by DigitalCommons@UTEP. It has been accepted for inclusion in Open Access Theses & Dissertations by an authorized administrator of DigitalCommons@UTEP. For more information, please contact [lweber@utep.edu](mailto:lweber@utep.edu).

# DEVELOPMENT OF NANOCOMPOSITES FOR ENERGY STORAGE DEVICES

MD ASHIQUR RAHAMAN KHAN

Department of Mechanical Engineering

APPROVED:

---

Yirong Lin, Ph.D., Chair

---

Chintalapalle V. Ramana, Ph.D.

---

Norman Love, Ph.D.

---

Tzu-Liang (Bill) Tseng, Ph.D.

---

Benjamin C. Flores, Ph.D.  
Dean of the Graduate School

Copyright  
by  
Md Ashiqur Rahaman Khan  
2012

## **Dedication**

To my parents and siblings.

# DEVELOPMENT OF NANOCOMPOSITES FOR ENERGY STORAGE DEVICES

by

MD ASHIQUR RAHAMAN KHAN, B.S.M.E.

THESIS

Presented to the Faculty of the Graduate School of

The University of Texas at El Paso

in Partial Fulfillment

of the Requirements

for the Degree of

MASTER OF SCIENCE

Department of Mechanical Engineering

THE UNIVERSITY OF TEXAS AT EL PASO

December 2012

## **Acknowledgements**

I want to express my gratitude to my supervisor Dr. Yirong Lin for providing motivation, advice, encouragement and all kinds of support for this thesis work. I am very grateful to him for his guidance and knowledge that he sheared throughout my thesis. I am very thankful to Dr. C. V. Ramana, Dr. Norman Love and Dr. Tzu-Liang (Bill) Tseng, my committee members for their support. I am very thankful to all the members of Dr. Lin's research group for their cooperation and help throughout my thesis work. I would like to thank Travis Wilson and Miguel Mendoza for their help and cooperation. I want to especially thank Mohammad Shuvo for his help and encouragements that kept me going. I want to express my gratitude to Jerred Chute for his kind help regarding the glove box. I would like to thank Katherine Thomas and Ruth Doasry for their kind help. I want to thank my parents and siblings, with their support I have accomplished whatever I have. I missed them very much, while staying far away from them. Lastly I would like to thank Sajib Barman, my roommate for tolerating me and encouraging me for the last one and half years.

Finally, I would like to thank Department of Mechanical Engineering, The University of Texas at El Paso for sponsoring my research presented in this work.

## **Abstract**

With the ever-increasing need in improving the performance and operation life of future mobile devices, developing higher power density energy storage devices has been receiving more attention. Lithium ion battery (LIB) and capacitor are two of the most widely used energy storage devices and have attracted increasing interest from both industrial and academic fields. Batteries have higher power density than capacitor but significantly longer charge/discharge rates. In order to further improve the performance of these energy storage devices, one of the approaches is to use high specific surface area nano-materials. Among all the nano-materials developed so far, one-dimensional nanowires are of special interests because of their high surface-to-volume ratio and aligned pathway for electron diffusion and conduction. Therefore, in this thesis work, zinc oxide nanowires are implemented as an anode along with carbon fiber/graphene to increase the performance of LIB while lead titanate nanowires are used to improve the energy density of capacitors.

For batteries, zinc oxide nanowires are grown on carbon cloth by low temperature hydrothermal method. X-ray diffraction (XRD) and scanning electron microscopy (SEM) are used to analyze morphology and crystal structures of samples. The performances of LIB using zinc oxide nanowire coated carbon cloth and bare carbon cloth are compared to show the improvement induced by zinc oxide nanowires. For capacitors, lead titanate (PTO) nanowires are used with Polyvinylidene fluoride (PVDF) to make nanocomposites of high dielectric constants. Lead titanate nanowires are synthesized by low temperature hydrothermal method. XRD and SEM are used to analyze as synthesized nanowires. Different volume fraction of PTO nanowires is used with PVDF to make dielectric for capacitor. Dielectric constant and breakdown voltage at variable frequency are determined to calculate energy density and specific energy density. The influence of temperature on energy densities of different volume fraction PTO nanocomposites is also determined in this thesis work.

## Table of Contents

Acknowledgements.....	v
Abstract.....	vi
Table of Contents.....	v
List of Tables .....	vii
List of Figures.....	viii
Chapter 1: Introduction.....	1
1.1 Lithium Ion Battery .....	1
1.2 Capacitors .....	6
Chapter 2: Literature Review.....	8
2.1 Cathode materials for LIB .....	8
2.2 Electrolytes for LIB .....	9
2.3 Anode material for LIB .....	10
2.4 Dielectric Capacitors .....	15
Chapter 3: Motivation and Significance .....	23
3.1 ZnO NWs as anode for LIB.....	23
3.2 Zinc oxide: Material properties .....	25
3.3 Zinc Oxide: Piezoelectric Effect.....	25
3.4 ZnO nanowires: Growth mechanism .....	27
3.5 Lead Titanate NWs for Dielectric Capacitor .....	31
3.6 Lead Titanate: Material Properties .....	32
3.7 Lead Titanate Nanowires Synthesis.....	33
Chapter 4: Experimental Details.....	37
4.1 Graphene synthesis .....	37
4.2 Zinc Oxide Nano Particle Solution.....	39
4.3 Coating Substrate with ZnO nanoparticles .....	41
4.4 ZnO nanowires: Hydrothermal growth.....	42
4.5 Anode Preparation .....	43
4.6 Coin Cell Assembly.....	45
4.7 Lead Titanate Nanowires .....	46
4.8 Pto Nws-Pvdf Nanocomposite.....	49



4.9 Sample Characterization.....	49
Chapter 5: Results and discussion .....	56
5.1 ZnO NWs coated Electrodes for LIB .....	56
5.2 PTO-PVDF Nanocomposites.....	66
Chapter 6: Conclusion .....	76
References.....	77
Curriculum Vita.....	90

## **List of Tables**

Table 1.1: Dielectric permittivity of different polymers . .....	19
Table 1.2: Breakdown strength and energy density of commonly used film polymers for capacitor .....	20

## List of Figures

Figure 1.1 Comparison of the different battery technologies in terms of volumetric and gravimetric energy density .....	1
Figure 1.2 Schematic details of Lithium ion cell during discharging .....	3
Figure 1.3 Schematic presentation of the operation in lithium ion battery .....	4
Figure 1.4 Voltage versus capacity for positive- and negative-electrode materials presently used or under serious considerations for the next generation of rechargeable Li-based cells .....	5
Figure 1.5 Simplified Ragone plot of the energy storage domains for the various electrochemical energy conversion systems compared to an internal combustion engine and turbines and conventional capacitors .....	7
Figure 2.1 Schematic structure of LiCoO <sub>2</sub> for lithium-ion batteries, (110) plane .....	8
Figure 2.2 schematic drawing of the crystal structure of hexagonal graphite, showing the AB layer stacking sequence and the unit cell .....	10
Figure 2.3 schematic drawing showing lithium intercalation into the graphite structure .....	11
Figure 2.4 Atomic structure of graphene. (a) Schematic structure of honeycomb lattice structure. (b) Schematic of sp <sup>2</sup> hybrid c-c bond structure containing in plane $\sigma$ bond and perpendicular $\pi$ bond .....	13
Figure 2.5 Graphene is 2D building material that can be wrapped to 0D buckminsterfullerene, rolled into 1D carbon nanotube and stacked to graphite .....	14
Figure 2.6 Schematic of a conventional capacitor .....	16
Figure 2.7 Schematic arrangement of electrolytic capacitor .....	17
Figure 2.8 Relationship of dielectric permittivity and electric field to the energy density of the dielectric. Organic dielectrics (O) have high breakdown strength and low permittivity. Ceramic-based inorganic dielectrics (I) have high permittivity and low breakdown strength. Composites (C) offer the potential for high permittivity and breakdown strength .....	18
Figure 2.9 Self-healing mechanism in polymer dielectric capacitor .....	21
Figure 2.10 Dielectric constant and dielectric strength of the common dielectric materials and their correlation for high energy density .....	22
Figure 3.1 Schematic view of the ZnO nanowire/Graphene hybrid and ZnO nanowire arrays/ carbon cloth anode material testing .....	24
Figure 3.2 (a) Schematics showing the piezoelectric effect in a tetrahedrally coordinated cation-anion unit (b) The wurtzite structure model of ZnO. The tetrahedral coordination of Zn–O is shown .....	26
Figure 3.3 Experimental setup and procedures for generating electricity by deforming a piezoelectric ZnO NW with a conductive AFM tip. The base of the NW is grounded and an external load of RL is applied, which is much larger than the resistance RI of the NW. The AFM scans across the NW arrays in contact mode .....	27
Figure 3.4 SEM images showing nucleation and growth behavior of ZnO nanowires on a Si substrate for reaction times of (a) 30 s, (b) 1 min, (c) 5 min, and (d) 60 min. The inset in (d) is a SEM image of the interfacial region of the nanowires and the substrate .....	28
Figure 3.5 Bright-field TEM images of ZnO seeds on a Si substrate grown for (a)–(c) 30 s and (d)–(f) 1 min. (g) HRTEM image of the region indicated by a dotted rectangle in (f). The seeds are clearly shown at the bottom of the ZnO nanowires, as indicated by black arrows in (d)–(f). Contrasts at the Si substrate below the seeds are indicated by white arrows in (a)–(d) .....	29
Figure 3.6 Analysis of ZnO nanowire arrays grown in water with zinc nitrate and HMTA at 90 °C. (A) Cross-sectional SEM image of an array grown for 1.5 h on a silicon wafer. (B) TEM image of a cluster of ZnO nanowires removed from an array grown for 1.5 h on a silicon wafer. (C) SEM cross section of a cleaved nanowire array grown with the addition of PEI on a fluorine-doped tin oxide substrate .....	30

Figure 3.7 Crystal lattice structure of $\text{PbTiO}_3$ : (a) projection of ionic sites on the (001) plane; (b) environment of the Ti ion; (c) environment of the Pb ion .....	33
Figure 3.8 SEM micrographs of nanowires formed by liquid-phase deposition method using 200-nm alumina template membranes. (a) Top view image of the $\text{PbTiO}_3$ nanowire arrays grown within an AAO template. (b) Side view image of $\text{PbTiO}_3$ nanowires bundle together after removing the AAO template .....	34
Figure 3.9 SEM image of PX-phase Pb–Ti–O nanowires synthesized by hydrothermal method .....	35
Figure 4.1 Graphite oxidization in water bath at 35 °C .....	37
Figure 4.2 Schematic presentation of the graphene synthesis steps a) Natural graphite with inter layer spacing 3.34 Å <sup>23</sup> b) Organic surface groups take place within the layers for oxidation and inter layer spacing becomes about 7.37 Å <sup>23</sup> c) Graphite oxide solution is exfoliated by sonication and becomes dispersed graphene oxide solution d) Freeze dried graphene oxide solution is reduced to graphene .....	39
Figure 4.3 ZnO Nanoparticle solutions are mixing on hot plate under vigorous stirring at 55 °C .....	40
Figure 4.4 Bare carbon cloth on the left hand side; ZnO NWs coated carbon cloth glued on the edges ..	42
Figure 4.5 ZnO nanowire growths on carbon fiber at 80 °C .....	43
Figure 4.6 Casting slurry on Cu foil to make anode and cut later by 12 mm diameter punch .....	44
Figure 4.7 Cross sectional view of LIB coin cell shows the sequence of components .....	45
Figure 4.8 Setup for PTO nanowire growth by hydrothermal method.....	47
Figure 4.9 Schematic diagram of the manufacturing process of nanocomposites .....	48
Figure 4.10 Bruker D8 Advance X-ray diffractometer used to characterize samples .....	50
Figure 4.11 Hitachi S-4800 Scanning Electron Microscope used to characterize samples.....	51
Figure 4.12 Performance analyzing LIB by battery analyzer.....	52
Figure 4.13 Experimental setup to measure breakdown voltage of nanocomposites.....	53
Figure 4.14 LCR meter used to measure dielectric constant and dielectric tangent loss of nanocomposites.....	54
Figure 4.15 Nanocomposite inside silicon oil for electrical testing .....	55
Figure 5.1 SEM images of ZnO nanowires on carbon cloth at different scale (a) 1 mm, (b) 40 μm, (c) 5 μm, (d) 1 μm.....	56
Figure 5.2 SEM images of ZnO nanowires on graphene at different scale (a) 10 μm, (d) 2 μm.....	57
Figure 5.3 SEM images of ZnO NWs/graphene anode surface at different scale (a) 1 μm, (b) 500 nm ..	58
Figure 5.4 Xrd result for ZnO NWs coated carbon cloth. Asterisk (*) peak is for carbon. The rest of the peaks belong to ZnO.....	59
Figure 5.5 Xrd results for graphene and ZnO NWs/graphene. Asterisk (*) peak is for graphene. The rest of the peaks belong to ZnO.....	60
Figure 5.6 Voltage Vs Specific Capacity plot for carbon cloth electrode against $\text{LiCoO}_2$ at 100 mA/g current rate .....	61
Figure 5.7 Voltage Vs Specific Capacity plot for ZnO NWs/carbon cloth electrode against $\text{LiCoO}_2$ at 100 mA/g current rate .....	62
Figure 5.8 Specific Capacity Vs cycle number for carbon cloth and ZnO NWs/ carbon cloth against $\text{LiCoO}_2$ at charging at 100 mAh/g .....	63
Figure 5.9 Voltage Vs specific capacity of graphene anode against $\text{LiCoO}_2$ cathode at 100 mA/g current rate .....	64
Figure 5.10 Voltage Vs Specific capacity plot for ZnO NWs/graphene anode against $\text{LiCoO}_2$ cathode at 100 mAh/g current rate.....	65
Figure 5.11 Specific capacity Vs cycle number for graphene and ZnO NWs/ graphene anode at 100 mA/g current in 0.01-3.7 V range.....	66
Figure 5.12 SEM images of PTO nanowires (a) Before annealing (b) After annealing at 600 °C for 2 h	67
Figure 5.13 XRD patter of PTO nanowires before and after annealing at 600 °C for 2 hours .....	68

Figure 5.14 SEM images of PTO-PVDF nanocomposites of different volume fraction of PTO nanowires (a) 5 %, (b) 10 %, (c) 20 % and (d) 30 % .....	69
Figure 5.15 Dielectric permittivity at 1 kHz of nanocomposites at different temperature as a function of PTO NWs volume fractions.....	70
Figure 5.16 Dielectric permittivity of nanocomposites for different frequency at room temperature .....	71
Figure 5.17 Dielectric loss tangent of different volume fraction nanocomposites at different temperature .....	72
Figure 5.18 Breakdown strengths of nanocomposites at various temperatures.....	73
Figure 5.19 Energy density of nanocomposites at different temperatures at 1 kHz frequency .....	74
Figure 5.20 Specific energy of nanocomposites of different volume fractions at 1 kHz at room temperature .....	75

## Chapter 1: Introduction

### 1.1 LITHIUM ION BATTERY

Battery and capacitors are widely used in portable electronics these days. Among the batteries, lithium ion battery is used by 63% of the portable electronics in the whole world [1]. Lithium ion battery offers the highest volumetric and gravimetric energy density as well as long cycle life [1]. High charge discharge rate, high reversible properties made lithium ion battery the best choice for modern electronics. Extensive research has been going on to improve the performance of lithium ion battery due to the dependency of portable electronics on it. Increased energy density and cycle life of lithium ion battery are more desirable for their use in plug in electronic vehicles [2].

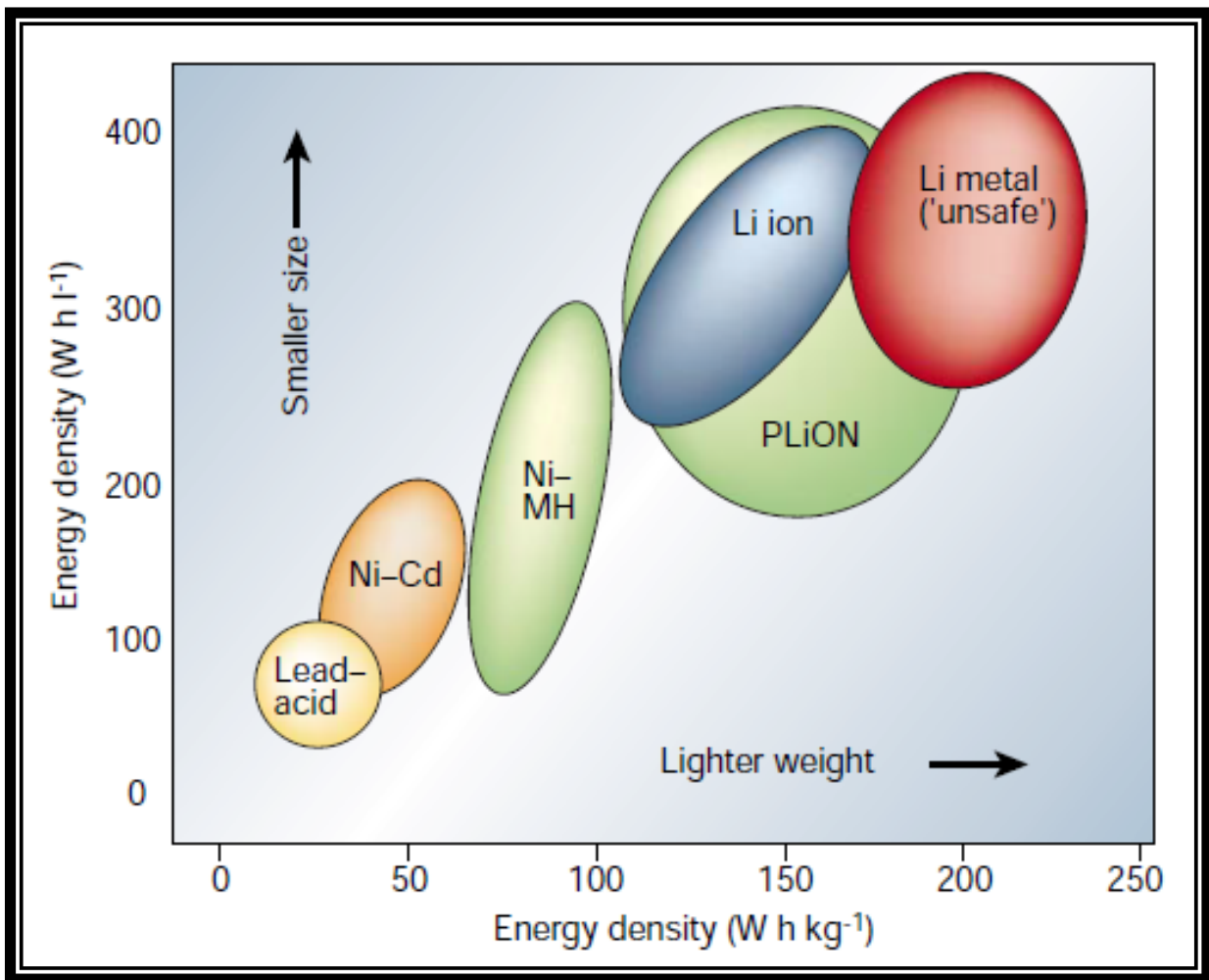


Figure 1.1 Comparison of the different battery technologies in terms of volumetric and gravimetric energy density [2]

Lithium ion batteries dominance is due to its highest electropositive and light properties suitable for energy storage device [2]. Lithium metal was first used in 1970s for non-rechargeable cell assembly. Due to their high capacity and discharge rate, application in mobile devices has increased. At the same time inorganic compounds are also found to perform reversible reaction with alkali metals. Later these materials were defined as intercalation compounds which were observed as vital for developing high energy rechargeable Li battery. In 1972 the understanding of electrochemical intercalation is defined which enabled scope of further development. Exxon [3] started a project in 1972 to use Li metal as anode and  $\text{TiS}_2$  as cathode material.  $\text{TiS}_2$  was found to have most suitable intercalation with lithium. But disadvantages of Li metal and liquid electrolyte combination were observed. Dendritic Li grown follows in every discharge charge cycle which results in explosion hazard. Dendrite problem [4] was solved by using lithium aluminum alloy but these electrodes performs for a limited number of cycle due to large change in volume while operation. Bell labs have found higher capacities and voltages for lithium oxides [5]. Later  $\text{Li}_x\text{MO}_2$  (where M is Co, Ni, Mn) [6, 7] were found to better choices for substitution for lithium metal. In order to avoid dendrite formation and use of Li metal, anode or electrolyte was modified. Substituting Li metal by second insertion material was reported by Murphy et al.[8] and later by Scrosati et al.[9] which followed the use of Li ion or rocking chair technology in early 1990s. The rocking chair technology which involves Li ion makes the battery much safer. In this rocking chair technique, Li ion moves back and forth between the anode and cathode over charge and discharge cycles. Sony Corporation commercialized lithium ion battery with C and  $\text{LiCoO}_2$  combination in 1991 [10]. This type of battery offered a potential over 3.6 V and energy density of about  $120\text{-}150 \text{ Whkg}^{-1}$ .

Electrochemical batteries can be classified as primary and secondary battery. Primary batteries are non-rechargeable but secondary batteries can be charged many times by reversing the flow of current. Common lithium ion batteries are made of electrodes, separators, electrolyte and current collectors. Two different slurries are made for anode and cathode. Active materials which participate in the electrochemical reaction are mixed with acetylene black (carbon black) and polymer (Polyvinyl Difluoride, PVDF). Organic solvents such as N-Methyl-2-pyrrolidone (NMP) or Dimethylformamide

(DMF) are used to make slurry. Carbon black is used to increase conductivity and PVDF used to hold the integrity of the structure and maintains contact between active materials and current collector.

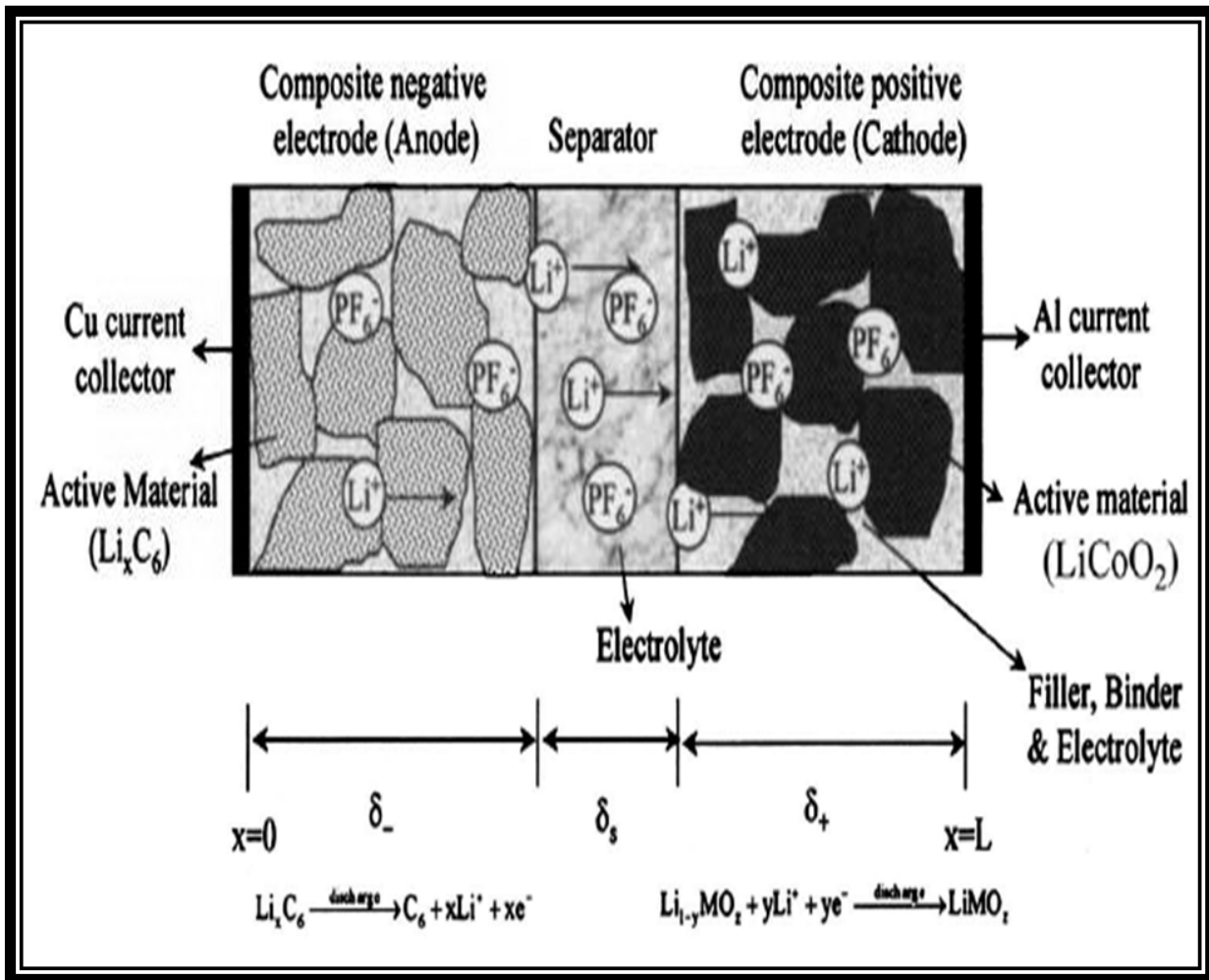


Figure 1.2 Schematic details of Lithium ion cell during discharging [11]

Copper foil and aluminum foil are used as current collectors for anode and cathode respectively. Micro porous polypropylene membranes act as separators placed in between two electrodes which keeps the battery from being shorted and permits  $\text{Li}^+$  ion to transfer from and to electrodes. Most common electrolyte solution of 1M  $\text{LiPF}_6$  in ethylene carbonate (EC)/ diethylene carbonate (DEC)/ dimethyl carbonate (DMC) in 1:1:1 volume ratio is used to fill up the rest of the void of the cell. Electrolyte carries  $\text{Li}^+$  ion between electrodes. A detailed schematic view is shown in figure 1.2 where graphite is used as anode and  $\text{LiCoO}_2$  as cathode.



Chemistry in battery can be described in two steps. Reduction occurs at cathode and oxidization occurs at anode. Electrolyte in between the cathode and anode facilitate the exchange of ions. During the charging of the battery, cathode releases electrons in the external circuit and  $\text{Li}^+$  in the electrolyte.  $\text{Li}^+$  passes through the micro porous separator to anode. This reverses during the discharge cycle. Cathode reaction can be showed as follows.

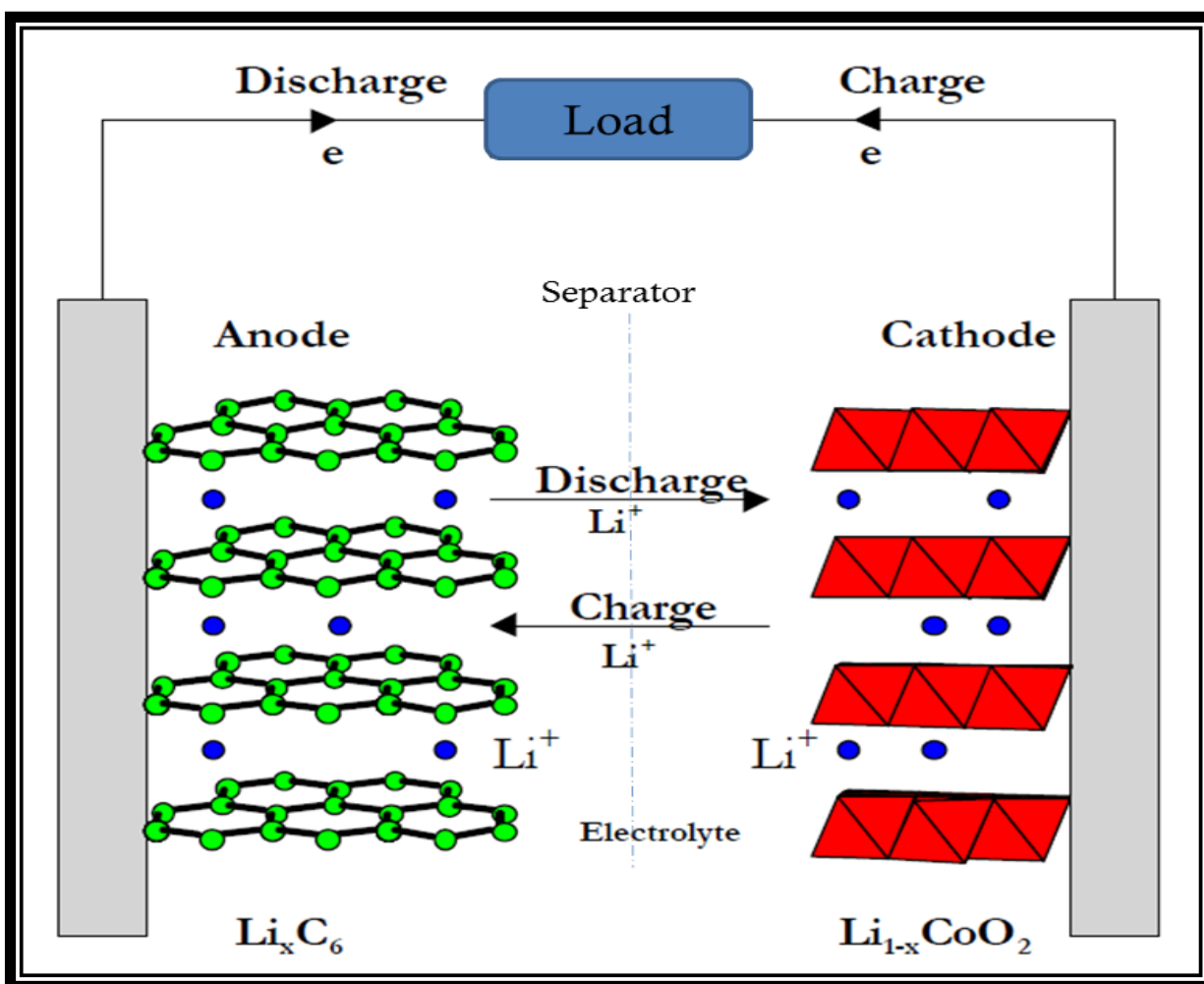
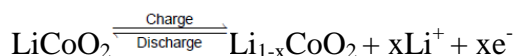
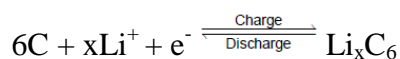


Figure 1.3 Schematic presentation of the operation in lithium ion battery

In the anode lithium intercalation occurs during the charging. The amount of  $\text{Li}^+$  stored in anode determines the energy capacity of the battery. Lithium ion released during the discharge cycle. Anode reaction can be shown as follows.



The overall reaction in a lithium ion battery cell can be shown as follows.

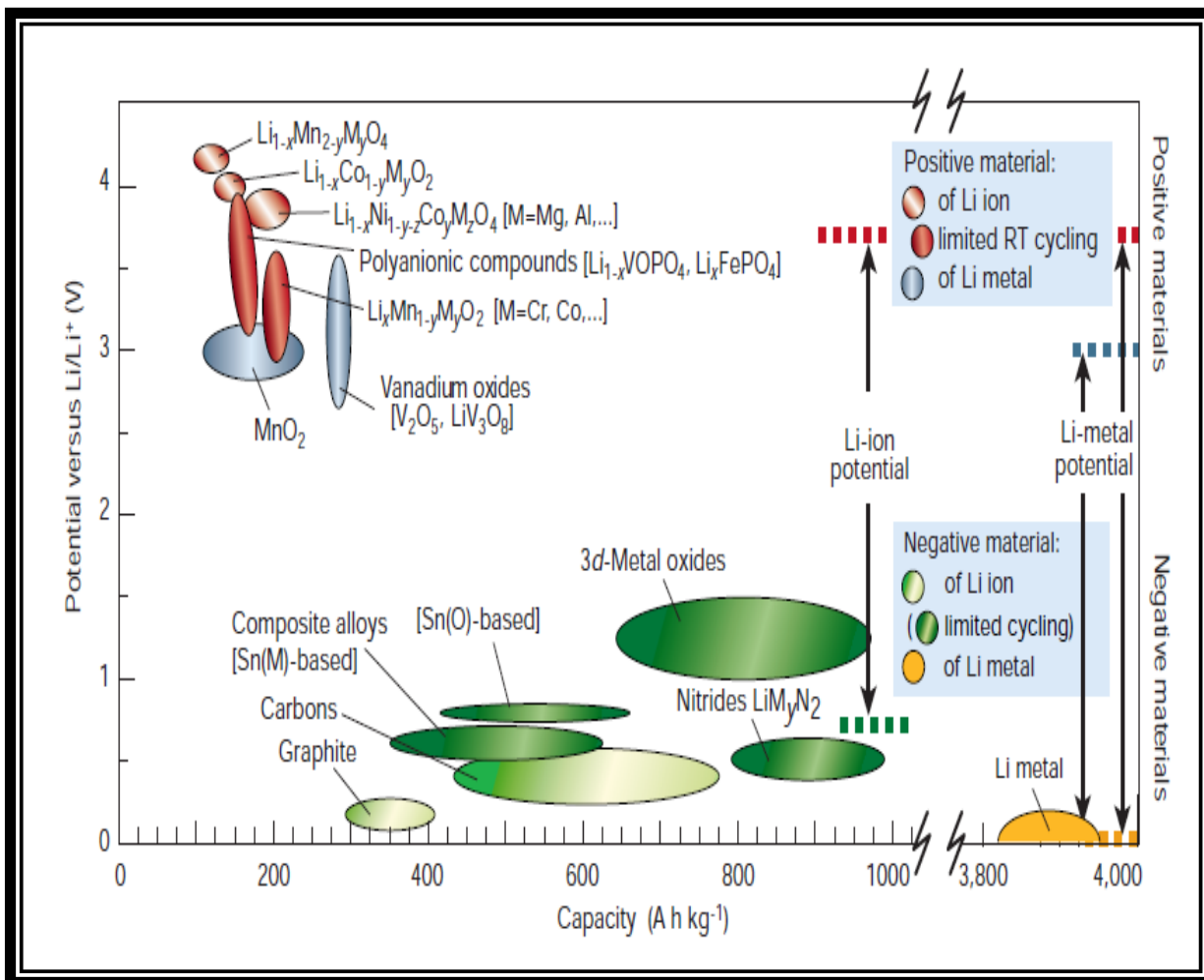
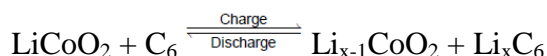


Figure 1.4 Voltage versus capacity for positive- and negative-electrode materials presently used or under serious considerations for the next generation of rechargeable Li-based cells [2]

Electrode compounds are chosen based on some characteristics. They should be accept and release lithium ion easily. Lithium intercalation- deintercalation should not change the structure of the compound. Electronic and ionic conductivity of the electrodes plays a vital role in the energy density of lithium ion battery. They should be highly conductive in this sense metallic electrodes are desirable. High porosity in electrodes are desirable since lithium ions are hosted in anode so higher surface area makes will increase the intercalation of ions. Electrodes should be stable and safe over a long period of

charging and discharging. Electrodes of low cost and environmentally non hazardous are desirable [12-15].

## **1.2 CAPACITORS**

Capacitors are widely used in electronics for storing energy. Capacitors can charge and discharge electricity very quickly. It is also used to block the flow of DC. This function is implemented where specific frequency is required. Capacitors can store little amounts of energy compared to batteries but can discharge the energy very quickly, meaning they have high power density. Pulsed power electronics needs quick power for short time that can be delivered only by capacitors. In order to scale down electronics devices development of capacitors that has high energy density and high volume efficiency is required [16].

The reason capacitors can charge and discharge quicker than batteries is that electrochemical reaction takes place in batteries where static charge is stored in capacitors. High performance lithium ion battery has limitations like low power density and low durability but capacitor can perform much longer than battery. Figure 1.5 shows energy and power densities of capacitors and batteries. Capacitors have highest specific power than any other energy storage devices.

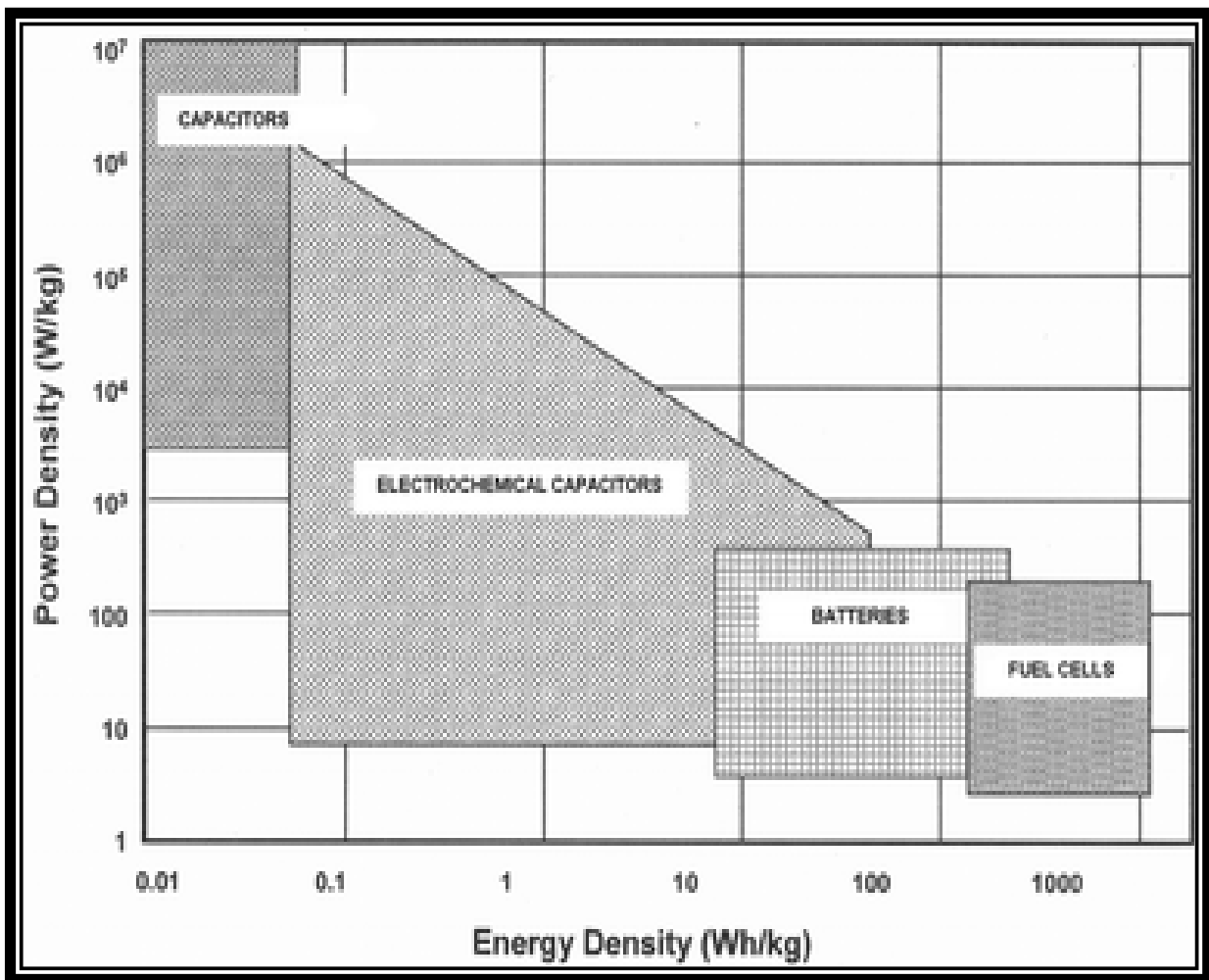


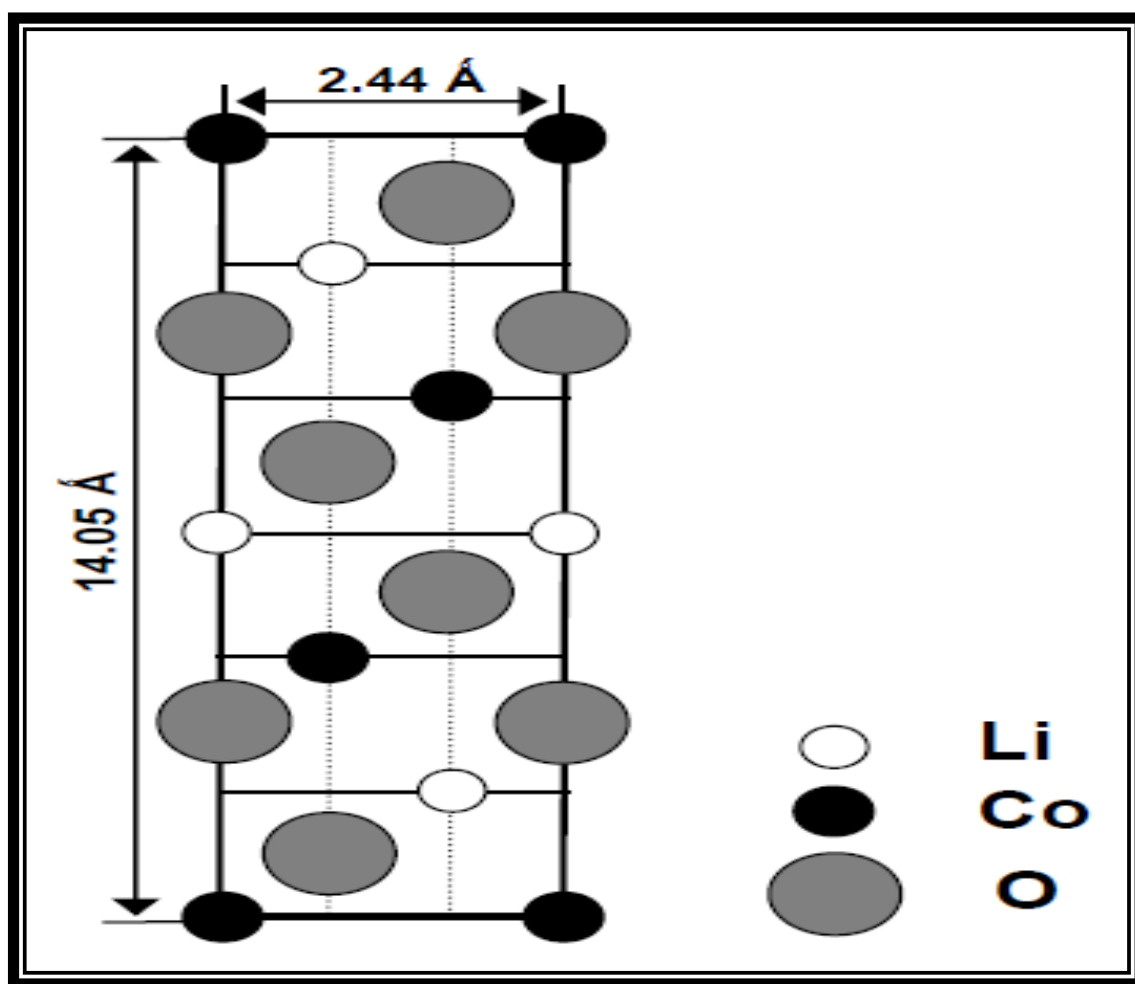
Figure 1.5 Simplified Ragone plot of the energy storage domains for the various electrochemical energy conversion systems compared to an internal combustion engine and turbines and conventional capacitors [17]

## Chapter 2: Literature Review

Previous researches done on cathode, anode and electrolyte of LIB are discussed below.

### 2.1 CATHODE MATERIALS FOR LIB

Selection of positive electrode varies for rechargeable lithium ion and lithium ion battery [18]. In lithium rechargeable batteries lithium metal is used as negative electrode and positive electrode does not require any lithiation. Lithium ion battery has carbon as the negative electrode which requires having lithium based compound to provide lithium ion. Lithium metal is very active in open air. Lithium cobalt oxide ( $\text{LiCoO}_2$ ) is widely used as cathode for commercial lithium ion battery.  $\text{LiCoO}_2$  has high volumetric energy density



$\text{LiNiO}_2$  is considered for anode in lithium ion battery because of its comparable specific capacity with  $\text{LiCoO}_2$ .  $\text{LiCoO}_2$  has a theoretical specific capacity of 140 mAh/g which is less than that of  $\text{LiNiO}_2$  at 200 mAh/g [20]. But delithiated  $\text{LiNiO}_2$  releases heat due to the reaction with electrolyte which raises safety issues. On the other hand  $\text{LiCoO}_2$  is thermally stable after delithiation.

The rhombohedra crystal structure of  $\text{LiCoO}_2$  is shown in figure 2.1. One equivalent cobalt atom and one lithium atom share two oxygen atoms in each layer of  $\text{LiCoO}_2$  [21]. The structure of layered  $\text{LiCoO}_2$  degrades because of over charge which is over 4.2 V against Li metal electrode [22]. Lithium manganese oxide ( $\text{LiMn}_2\text{O}_2$ ) and lithium iron phosphate ( $\text{LiFePO}_4$ ) have been studied as suitable substitution of lithium cobalt oxide. Manganese is cheaper and more readily available compare to cobalt. Manganese is not as environmentally hazardous as cobalt. But  $\text{LiMn}_2\text{O}_2$  has low energy density of 150-160 mAh/g [23, 24], low cyclic durability and is structurally unstable at high temperature [25].

## **2.2 ELECTROLYTES FOR LIB**

It has been reported that equal combination of alkyl carbonates which includes organic solvents of ethylene carbonate (EC), propylene carbonate (PC), dimethyl carbonate (DMC), diethyl carbonate (DEC) or ethyl-methyl carbonate (EMC) with  $\text{LiClO}_4$  or  $\text{LiPF}_6$  electrolyte salt solution is most suitable electrolyte for Li ion battery [20, 26, 27]. The desired properties for a suitable electrolyte are good ionic conductivity, low electronic permittivity to preclude self-discharge and good stability over a wide voltage window. Ethylene carbonate is very essential for electrolyte because it can bring stability to the electrolyte and can form a protective film over the anode to prevent further reduction due to the electrolyte. For carbon based anodes such as graphite, lithiation and stability of anode in electrolyte solution is depend on electrolyte composition [28].  $\text{LiPF}_6$  is very sensitive to moisture and produces hydrofluoric acid (HF) by reacting with water. HF reacts with cathode and form LiF which protects cathode from lithiation and delithiation and thus affects cell performance. Many researchers are investigating to replace the liquid electrolyte with polymer electrolytes which are solvent free and increase or maintain the specific energy density available in current Li ion batteries. Polymer electrolytes are safe and processing cost can be lowered as batteries can be made flexible [29, 30]. Also polymer electrolyte acts as separator as well as transport  $\text{Li}^+$  between electrodes. But polymer electrolyte

have ionic conductivities of  $10^{-8}$  to  $10^{-5}$  S cm<sup>-1</sup> at ambient temperature [31] which considered low when compared to liquid electrolyte which have ionic conductivities around  $10^{-3}$  to  $10^{-2}$  S cm<sup>-1</sup> [32]. Polymer electrolytes also have low power density compared to liquid electrolyte.

### 2.3 ANODE MATERIAL FOR LIB

Carbon based materials have been used as anode since 1970's but received a lot of attention in the late 80's due to its lithium ion reversibility property. The use of carbon anode is reported by Kanno et al. [33] and Mohri et al. [34] in 1989. Carbon has suitable crystallinity and structure for electrochemical insertion-extraction of lithium ion. The morphology of carbon based material is also important for the rate and amount of Li<sup>+</sup> can be stored in the anode.

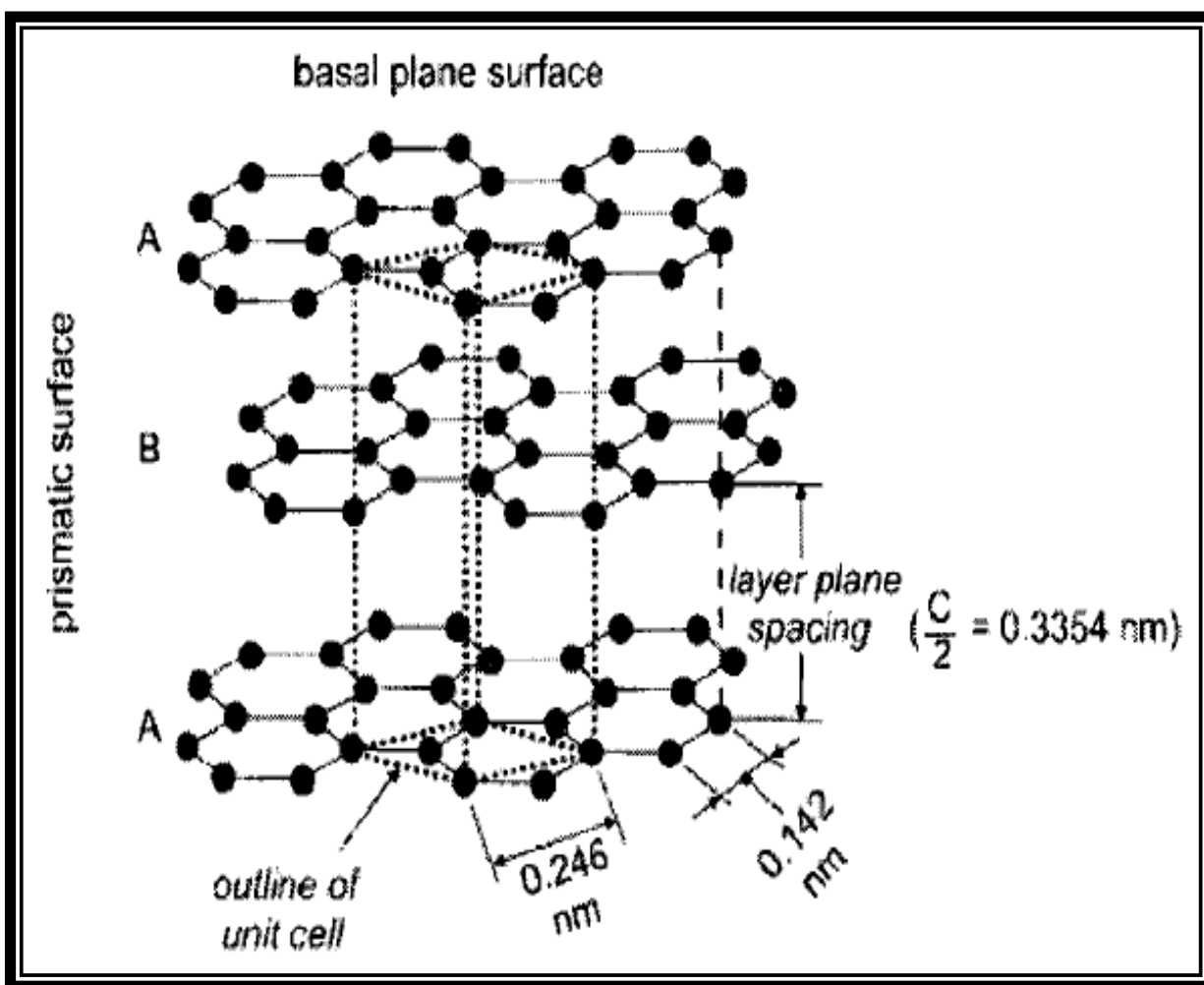


Figure 2.2 schematic drawing of the crystal structure of hexagonal graphite, showing the AB layer stacking sequence and the unit cell [35]

Schematic illustration of hexagonal graphite is shown in figure 2.2. Carbon atoms are arranged in a layer by layer fashion. Each layer of carbon atoms is called graphene which are attached due to Van der Waals forces. Graphite refers to stacking of graphene layer regardless of AB (hexagonal) or ABC (rhombohedral). The transformation energy from AB to ABC and vice versa is very low that's why perfect AB or ABC graphite is not possible to obtain. Any type of graphene layer stacking is called graphite. High crystalline graphite can host one lithium atom for every six carbon atoms. Graphene layers shift to AA stacking order while the intercalation occurs. The distance between the two graphene layers increases about 10.3% due to host Li atoms [36, 37].

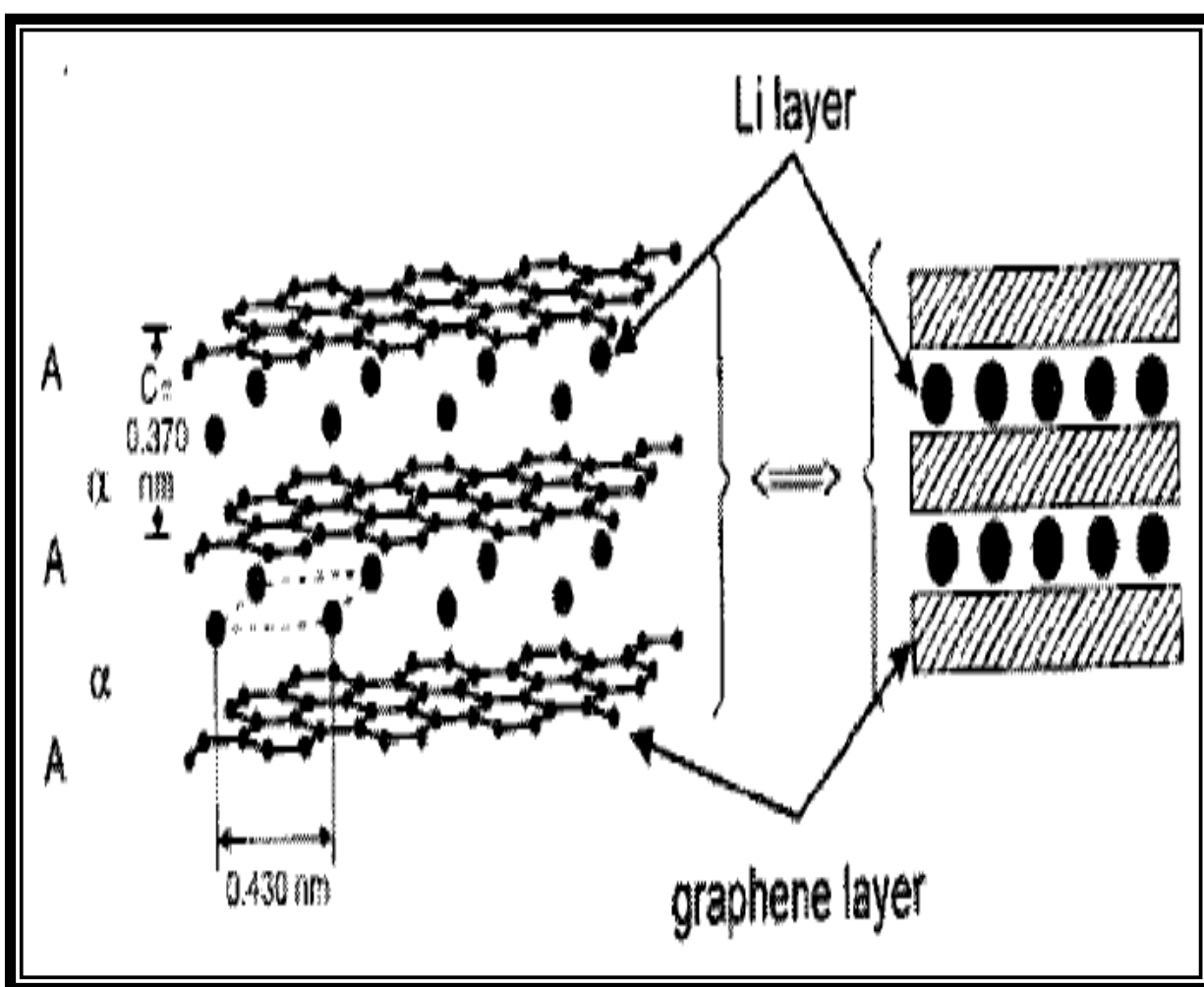


Figure 2.3 schematic drawing showing lithium intercalation into the graphite structure [35]



The stage formation happens during the first cycle of charging which requires energy. That's why 1<sup>st</sup> cycle of charging energy exceeds the theoretical specific energy of graphite (372 mAh/g) and 80-95 % of the energy is reversed by the deintercalation of Li<sup>+</sup> from the graphite layers [35].

Two dimensional layers of carbon a single atom thick, graphene have better electrical conductivity than graphite and a maximum surface area of 2600 m<sup>2</sup>/g [38]. The sp<sup>2</sup> hybridized carbon atoms are arranged in honeycomb lattice structure in each layer. There are two interpenetrating triangular sub lattices arranged as shown in figure 2.3. The atom from one sub lattice is the center of the other sub lattice. The atomic length between two carbon atoms is 1.42 Å. Two carbon atoms form a unit cell and at an

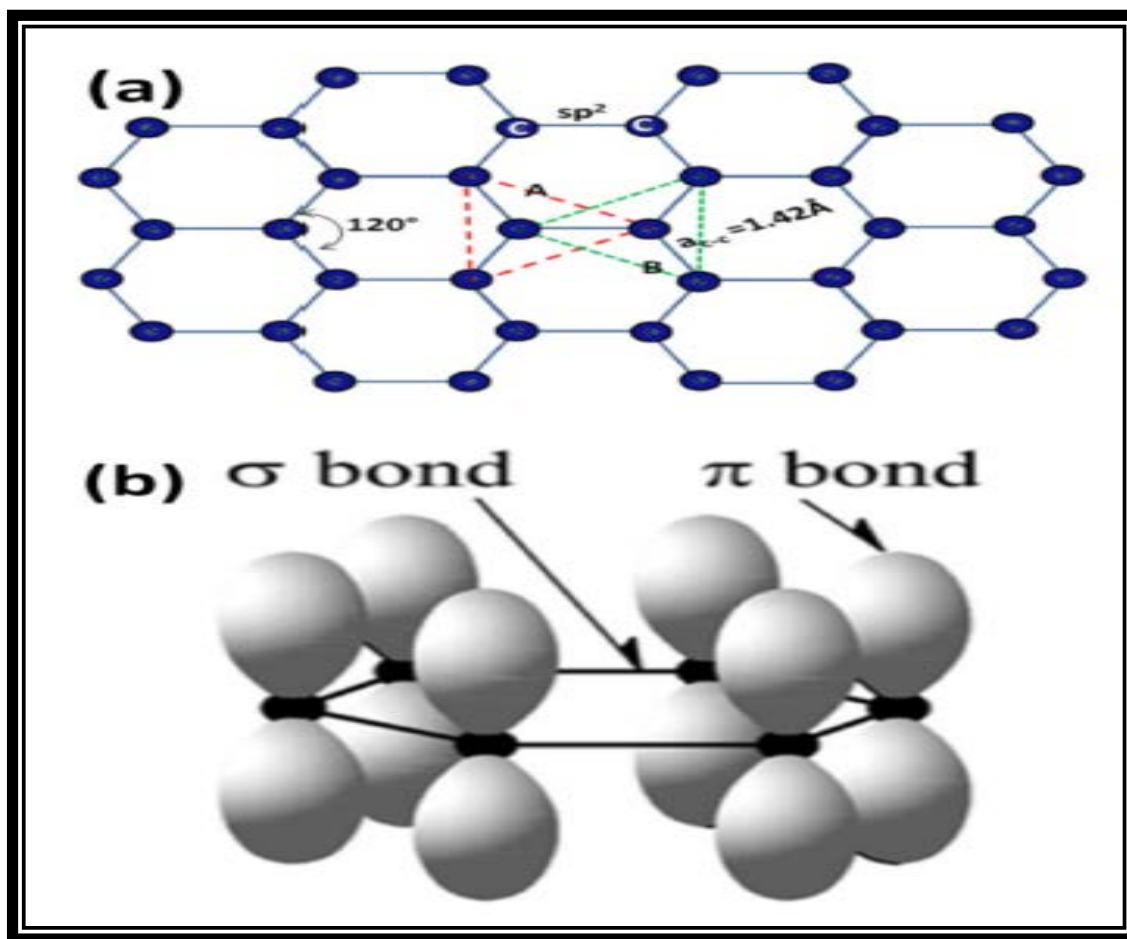


Figure 2.4 Atomic structure of graphene. (a) Schematic structure of honeycomb lattice structure. (b) Schematic of  $sp^2$  hybrid c-c bond structure containing in plane  $\sigma$  bond and perpendicular  $\pi$  bond [39]

Graphene can be rolled to form one dimensional carbon nanotubes. It can also be used to make a sphere shape called zero dimensional fullerenes as shown in figure 2.5. Multi-walled Carbon nanotubes are used as anode that showed energy capacity of 145-400 mAh/g [41-44]. But single wall carbon nanotubes have shown an energy density of 450 mAh/g [45-47]. Theoretical prediction about the  $Li^+$  intercalation in walls of nanotubes is not favorable because of its high energy barrier of 10 eV [48-50]. Opening of carbon nanotubes which become graphene improves energy density significantly [47, 51].

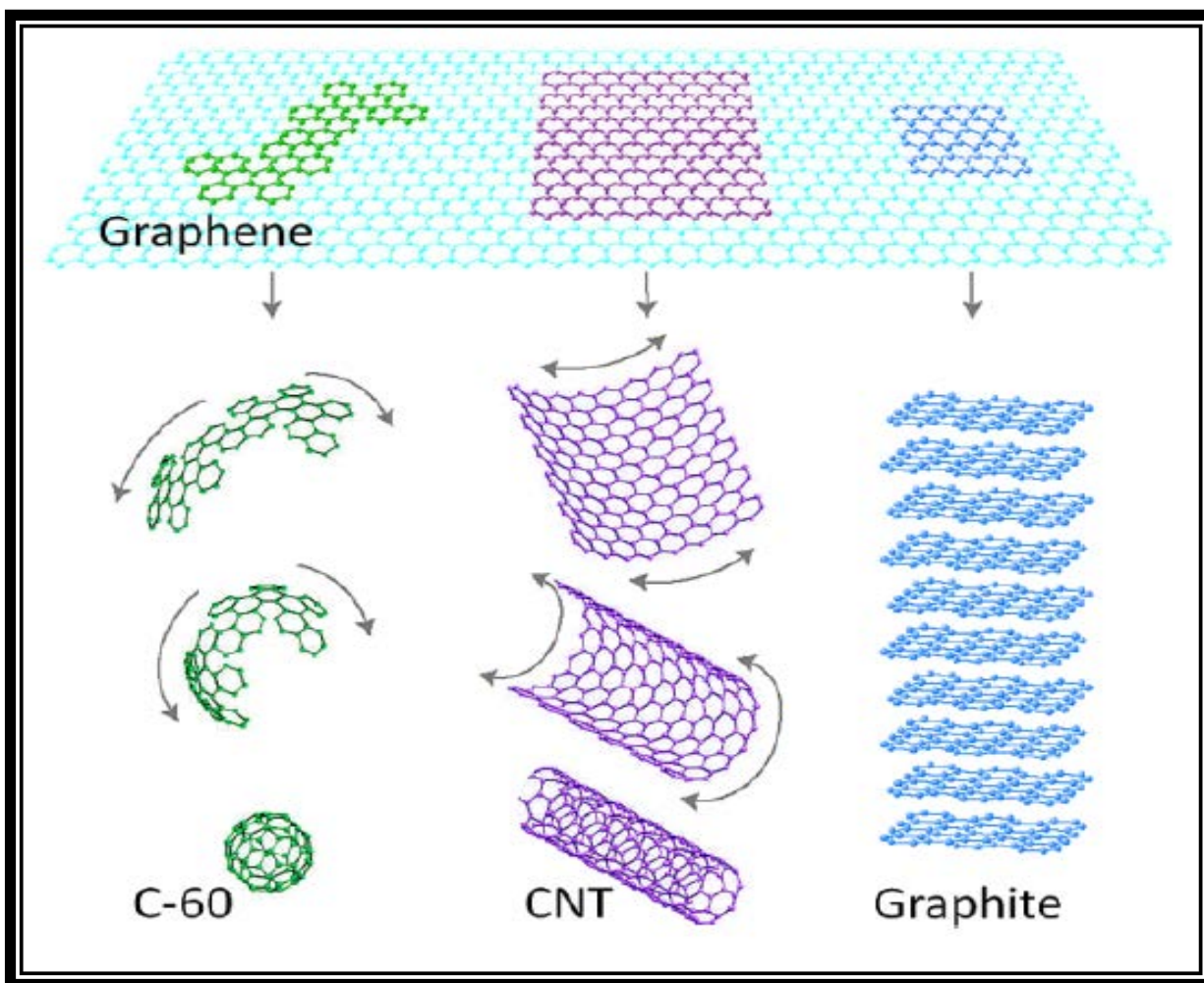


Figure 2.5 Graphene is 2D building material that can be wrapped to 0D buckminsterfullerene, rolled into 1D carbon nanotube and stacked to graphite [52]

Yoo et al. [38] and Abouimrane et al. [53] used graphene as anode in LIB and found higher energy density compare to graphite. Graphene is being used along with other material such as  $\text{Co}_3\text{O}_4$  nanoparticles by kim et al. [54] and Wu et al. [55],  $\text{TiO}_2$  by Choi et al. [56],  $\text{SnO}_2$  by Yao et al. [57],  $\text{Mn}_3\text{O}_4$  nanoparticles by Wang et al. [58], silicon nanoparticles by Lee et al. [59],  $\text{Fe}_3\text{O}_4$  by Zhou et al. [60]. Researchers are searching for suitable material that can be used along with graphene to increase the lithium ion reversible capacity. Tin based oxides such as  $\text{SnO}_2$  is an n-type semiconductor considered as anode for LIB and reported 600-712 mAh/g energy density [61-64]. Promising results of semiconductors as anodes made researchers interested about zinc oxide. Belliard et al. [65] considered zinc oxide as anode material and found 400 mAh/g reversible capacity by using 60 ( $\pm 10$ ) nm particles. Zinc oxide has a theoretical specific capacity of 978 mAh/g [65]. In another report [66] zinc oxide particles of size 1- 5

$\mu\text{m}$  are used and reversible capacity of 359 mAh/g is found in first cycle. Shenouda et al. [67] doped  $\text{LiFeO}_4$  with different concentration of zinc oxide and reported increase in reversible capacity at low concentration and decrease at high concentration. Zinc oxide nano structures have high reversible capacity and rate capacity when used in LIB as anode materials [68]. Carbon fibers are also used as anode material for LIB [69]. Egashira et al. [70] used Sn nanoparticles to increase the reversible capacity of carbon fiber from 87 to 200 mAh/g.

## **2.4 DIELECTRIC CAPACITORS**

Capacitors can be three different types: electrostatic capacitor, electrolytic capacitor and electrical double layer capacitor. Only electrostatic capacitor does not require any liquid electrolyte. Electrostatic capacitor is the most conventional capacitor consists of two electrodes separated by a dielectric material which insulates them. Dielectric separates the charges and produces electrical field, enabling capacitor to store energy. Figure 2.6 illustrates capacitor arrangement.

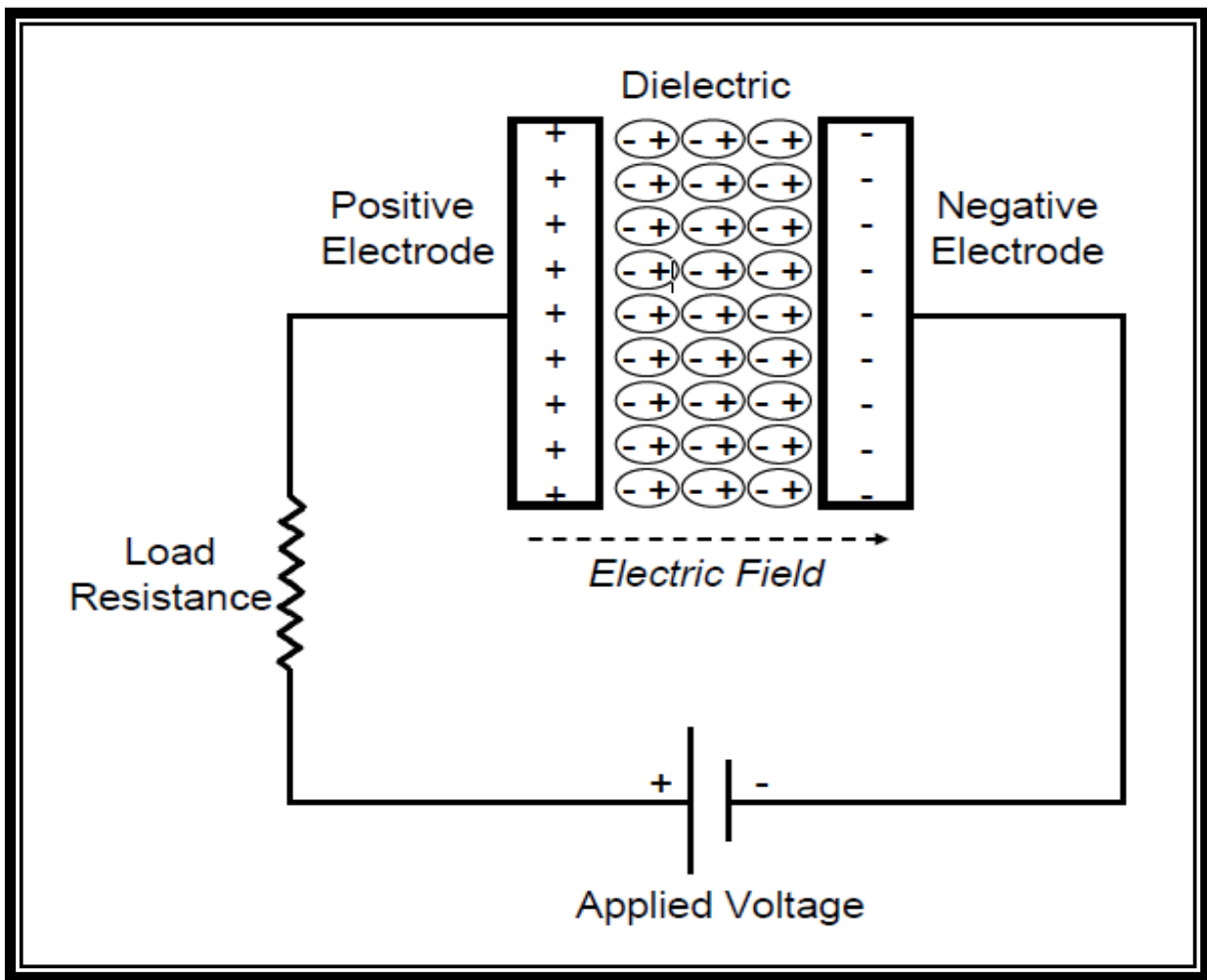


Figure 2.6 Schematic of a conventional capacitor [71]

Capacitance of a capacitor  $C$  is expressed as

$$W = \frac{1}{2} \epsilon_0 \epsilon_r E_{bd}^2$$

Loss tangent  $\tan\delta$  is the ratio of imaginary part of permittivity  $\epsilon''$  to the real part of permittivity

$\epsilon'$

$$\tan \delta = \frac{\epsilon''}{\epsilon'} \dots\dots\dots(4)$$

Higher loss tangent indicates higher energy loss of dielectric during operation.

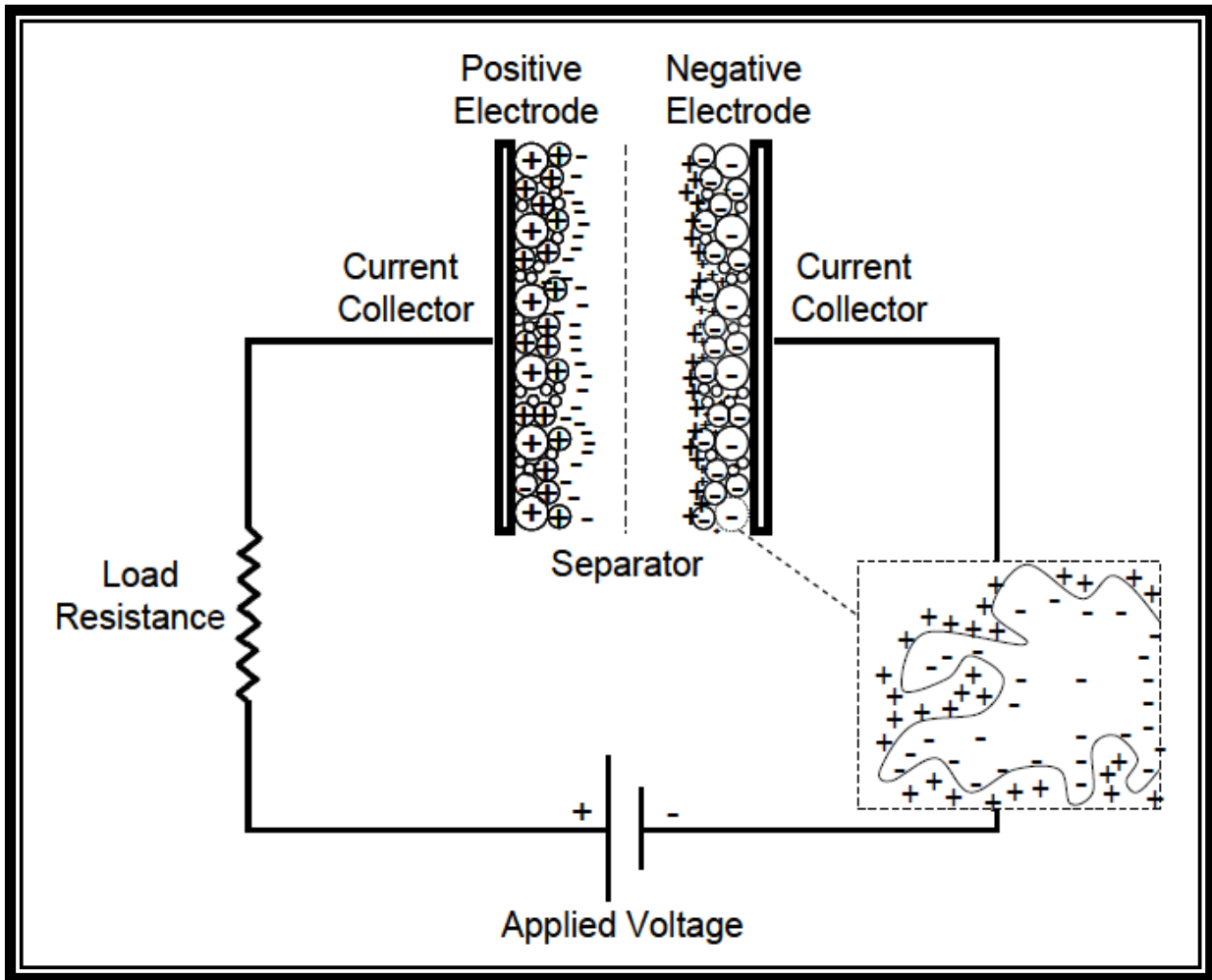


Figure 2.7 Schematic arrangement of electrolytic capacitor [71]

Arrangement of an electrolytic capacitor is shown in figure 2.7. The principle of electrolytic capacitor or supercapacitor is same as electrostatic capacitor. In supercapacitors the electrodes have high surface area, electrolyte is used and a microporous separator is placed in between the electrodes.

Supercapacitor minimizes the distance between the positive and negative charges as shown in figure 2.7. Thus shows higher energy density. But distance between the electrodes can be higher than the

solid dielectric because of the pure conductivity of the electrolyte and also super capacitors has to be sealed to protect liquid electrolyte thus prevent from implication in integrated device [72].

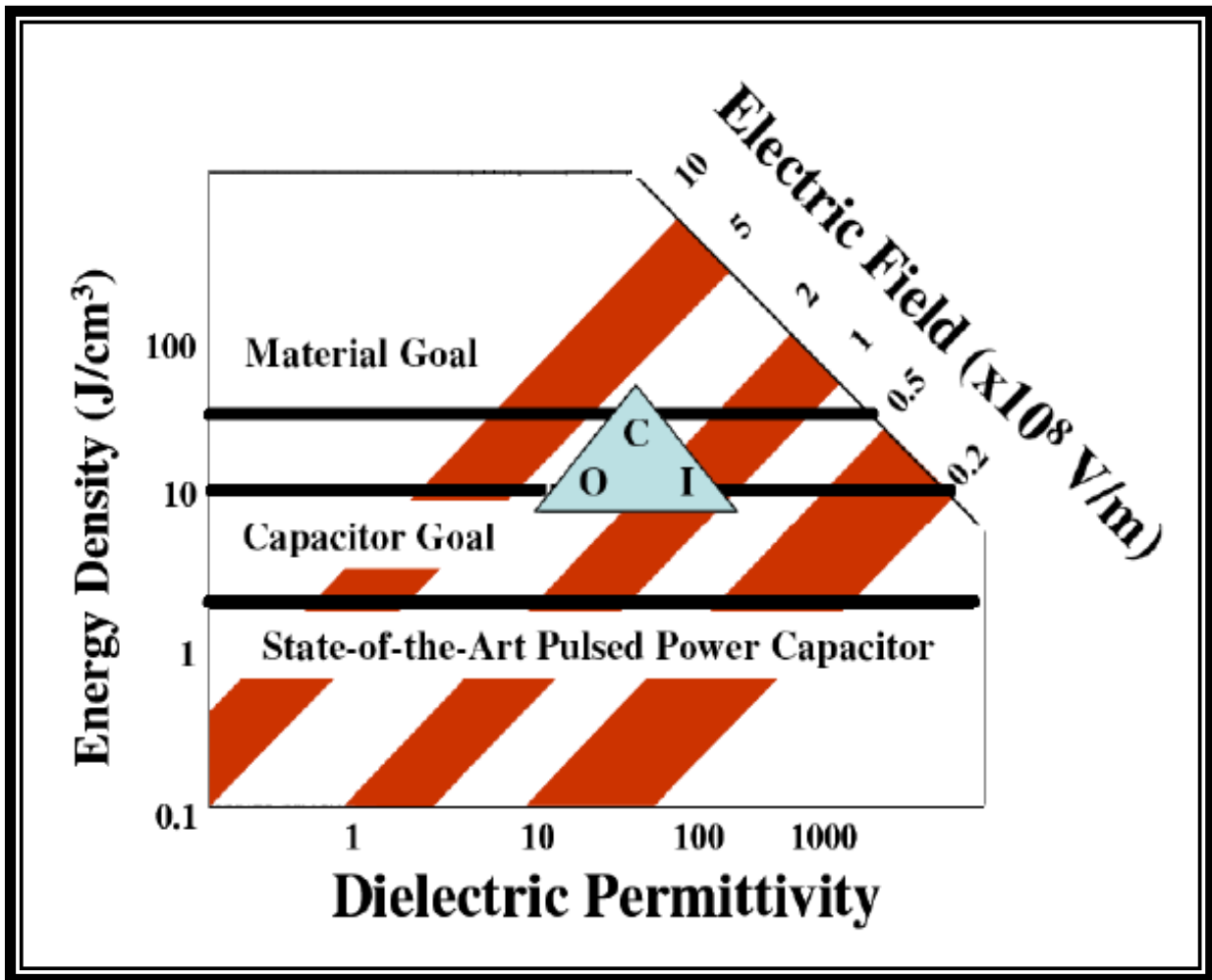


Figure 2.8 Relationship of dielectric permittivity and electric field to the energy density of the dielectric. Organic dielectrics (O) have high breakdown strength and low permittivity. Ceramic-based inorganic dielectrics (I) have high permittivity and low breakdown strength. Composites (C) offer the potential for high permittivity and breakdown strength [73]

The desired properties for capacitors are high dielectric permittivity, high breakdown strength, low dielectric loss tangent, low distance between the electrodes and high operating temperatures. Figure 2.8 shows the relationship between dielectric permittivity and breakdown strength of dielectric with energy density of the capacitor.

Research to improve energy density of capacitor is focused on development of composite dielectric material of high energy density and that can be stored in small packages [74-76]. Polymers are considered as dielectric because of their high dielectric permittivity. Polymers have very low dielectric permittivity that limits the energy density of the capacitor.

Table 1.1: Dielectric permittivity of different polymers [77, 78].

<b>Polymer</b>	<b>Dielectric permittivity</b>
Nonfluorinated aromatic polyimides	3.2-3.6
Fluorinated polyimide	2.6-2.8
Poly(phenyl quinoxaline)	2.8
Poly(arylene ether oxazole)	2.6-2.8
Poly(arylene ether)	2.9
Polyquinoline	2.8
Silsesquioxane	2.8-3.0
Poly(norborene)	2.4
Perfluorocyclobutane polyether	2.4
Fluorinated poly(arylene ether)	2.7
Polynaphthalene	2.2
Poly(tetrafluoroethylene)	1.9
Polystyrene	2.6
Poly(vinylidene fluoride-co-hexafluoropropylene)	~12
Poly(ether ketone ketone)	~3.5
Polyvinylidenefluoride (PVDF)	12



Table 1.2: Breakdown strength and energy density of commonly used film polymers for capacitor [78].

Plastic film	Dielectric permittivity,	Maximum operating temperature	Breakdown Voltage(V/ $\mu$ m)	Dissipation factor, % at 1kHz	Energy density (J/cc)
Polypropylene (PP)	2.2	105	640	<0.02	1-1.2
Polyester (PET)	3.3	125	570	<0.5	1-1.5
Polycarbonate (PC)	2.8	125	528	<0.15	0.5-1
Polyvinylidene fluoride (PVDF)	12	125	590	<1.8	2.4
Polyethylene naphthalate (PEN)	3.2	125	550	<0.15	1-1.5
Polyphenylene sulfide (PPS)	3.0	200	550	<0.03	1-1.5

Relatively high dielectric permittivity and high breakdown strength make PVDF most suitable candidate as dielectric material. Polymer film has self-healing capability which makes it better candidate for high electric field application [79]. The self-healing process is shown in figure 2.9. During the electrical breakdown, part of the stored energy will make a hole in the polymer. Also the metal electrode on the surface of the polymer gets evaporated and this way the polymer film breaks open instead of getting short. The rest of the portion of the capacitor stays functional with small drop in capacitance.

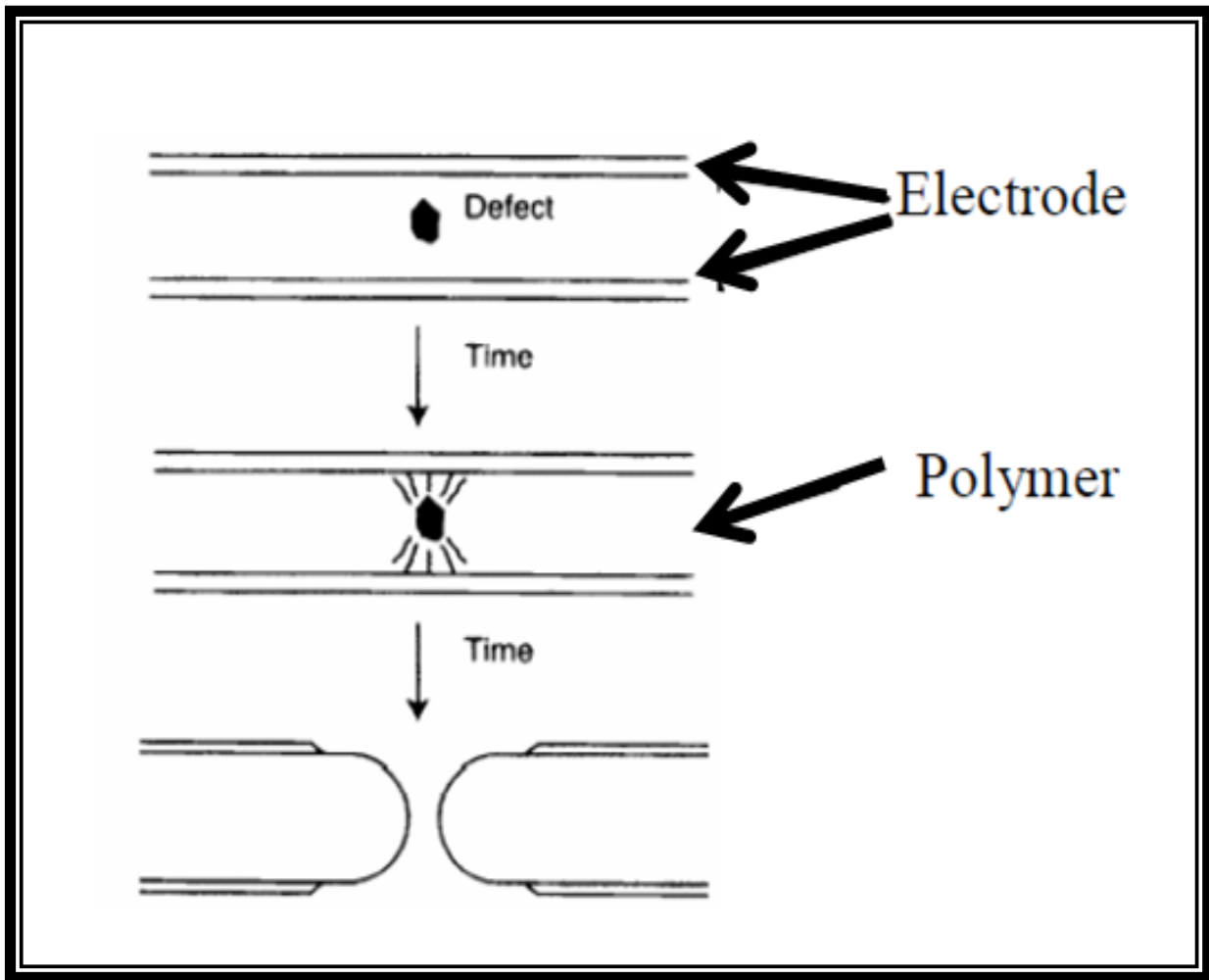


Figure 2.9 Self-healing mechanism in polymer dielectric capacitor [79]

In order to increase the dielectric permittivity of the dielectric, ceramics are considered because of their high dielectric constant. But low breakdown strength than polymer lowers the energy density of the capacitor. Ceramic capacitor does not have self-healing property which makes them less reliable. Sintering of ceramic in large scale is also very problematic because of stress formation. Figure 2.10 shows the experimental results of dielectric constant and breakdown field of different dielectric material. The straight line is shows 400 calculated from dielectric constant and square of breakdown strength from equation 3 of energy density. The rest of the terms in energy density equation are constants.



## **Chapter 3: Motivation and Significance**

Piezoelectric and semiconductor materials are suitable for energy harvesting and storage application [81-83]. One-dimensional nanostructure such as nanowire, nanorod and nanotube is drawing much research interest in recent years because of their possible applications in nano-scale devices [84]. One-dimensional nanomaterials have very high surface area with tunable dimension and crystal morphology. Optical [85], magnetic [86] and electrical [87] properties of nanostructure vary depending upon many factors such as temperature, duration of reaction, pressure, molar concentrations of chemicals used in different synthesis procedures which are responsible for the size and shape of nanostructures. Nanowires have highest aspect ratio (Length to diameter) which offers high surface area. Electrochemical performance can be greatly affected by surface area of electrodes. Lead titanate (PTO) and zinc oxide (ZnO) both are piezoelectric materials and can be used for energy harvesting and storage applications. In this thesis work, zinc oxide is used to make anode material for lithium ion battery and lead titanate is used with polyvinyl fluoride to make capacitor.

### **3.1 ZNO NWS AS ANODE FOR LIB**

Due to the limited specific surface area of graphite materials, the diffusion of the Li ions in the anode graphite is relatively slow, leading to limited energy storage density. In order to further increase the capacity, nano-structured materials have been extensively studied due to its potential in reducing Li-ion diffusion pathway. To date, one of the most promising approaches to improve the Li-ion diffusion rate is to introduce hybrid nanostructured electrodes that connect the nonconductive high surface area nanowire with nanostructured carbon materials. While there have been several research efforts investigated to fabricate nanowire-graphene hybrids, all the them were focused on randomly distributed nanostructures thus the LIB performance enhancement was limited. Therefore, this paper will introduce a novel hybrid structure with vertically aligned nanowire on graphene aerogel aiming to further increase the performance of LIB. The aligned nanowire array provides a higher specific surface area and could lead to high electrode-electrolyte contact area and fast lithium ion diffusion rate. The graphene aerogel structure is electrically conductive and mechanically robust, as well as has low specific density. The developed nanowire/graphene hybrid structure could have the potential to enhance the specific capacity

and charge-discharge rate. Smaller sized particles reduce strain during lithiation and delithiation which results better cycling performance [88, 89] which shows the potential of nanowires. Materials of nano morphology can increase the lithium ion diffusion rate as well as stabilizes the material for longer operation cycle than bulk dimension [90]. Charge and discharge rate of active materials can be increased with the use of nano scale materials. Solid state diffusion occurs in electrodes so shorter travel path for lithium ion will increase insertion and extraction rate. In the figure 3.1, schematic view of ZnO NWs/graphene and ZnO NWs/carbon cloth anode materials are shown in the lithium ion battery arrangement.

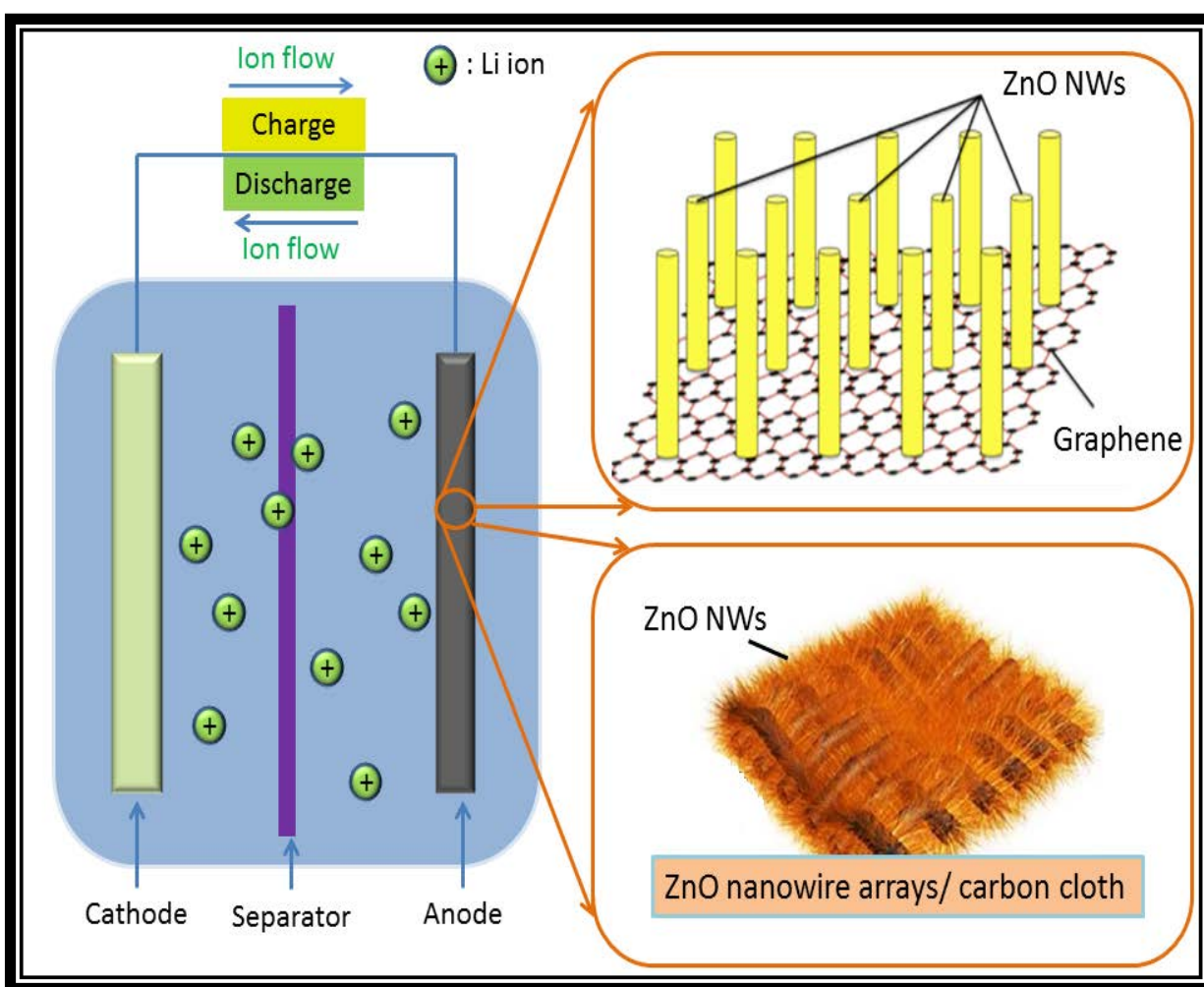


Figure 3.1 Schematic view of the ZnO nanowire/Graphene hybrid and ZnO nanowire arrays/ carbon cloth anode material testing [69]

### **3.2 ZINC OXIDE: MATERIAL PROPERTIES**

Zinc oxide is n type semiconductor which has electrical, optical, piezoelectrical, optoelectrical and many other important applications because of its wide band gap (3.37 eV) and high electron hole binding energy (60 eV)[91, 92]. Wurtzite is the most stable form of zinc oxide which lacking center of symmetry and has large electrochemical coupling. Zinc oxide has piezoelectric, pyroelectric properties, emits light of short wavelength and appropriate doping makes it electrically conductive. Zinc oxide is also biocompatible, biodegradable and nontoxic which extends the area of its biological application [93]. Discovery of zinc oxide nanobelt in 2001 has created research interest in zinc oxide nanostructure [94]. Intensive research has been done on zinc oxide nanostructures especially on nanowires because of their ease of synthesis process and better electrochemical properties. Electron diffusion rate can be heavily increased by increasing surface area of nanostructures. Zinc oxide has electron mobility of  $200 \text{ cm}^2 \text{ V}^{-1}$  at room temperature in single crystal form. Zinc oxide nanowires are single crystal and can be grown on any inexpensive substrates. Zinc oxide offers better resistance to radiation than gallium nitride which makes it more desirable for nuclear plant and space use.

### **3.3 ZINC OXIDE: PIEZOELECTRIC EFFECT**

Many wireless electrical devices require little power and self-powering will make them more consistent. Zinc oxide nanowires and lead titanate nanowires can be used for energy harvesting because of their piezoelectric properties. All the piezoelectric material has the same mechanism to produce electricity from mechanical strain. Here piezoelectric effect of zinc oxide is described. Zinc oxide has a non-centrosymmetric structure where oxygen and zinc atoms are tetrahedrally bonded. Any external mechanical pressure can cause lattice distortion leads to the displacement of positive and negative charge [95]. Local dipole moments are created and because of this a macroscopic dipole moments appears throughout the whole crystal. Zinc oxide gives the highest piezoelectric properties among the other tetrahedrally bonded semiconductor [96].

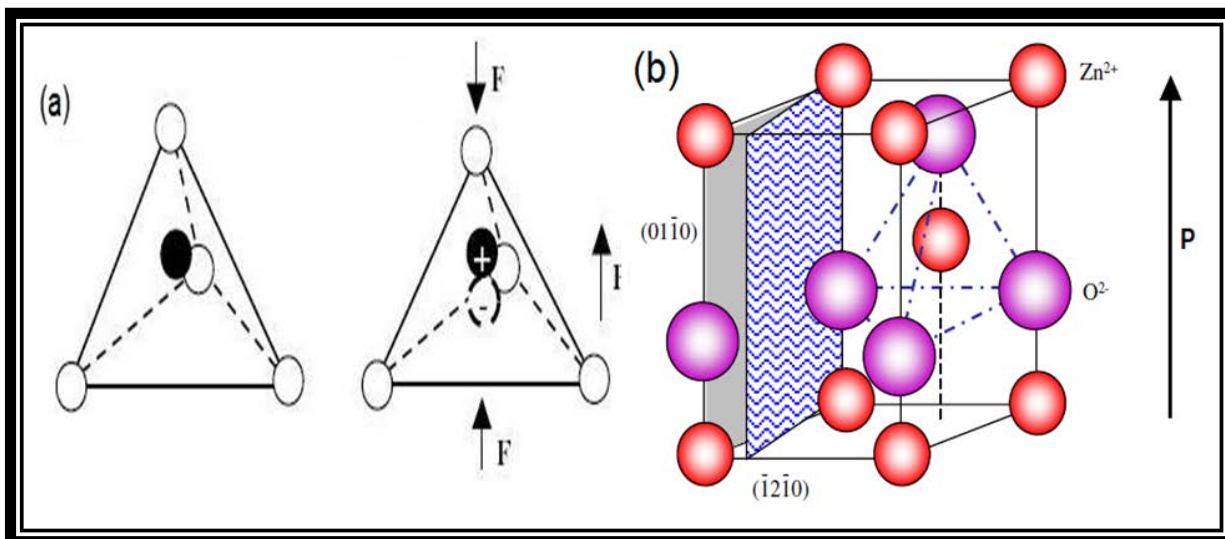


Figure 3.2 (a) Schematics showing the piezoelectric effect in a tetrahedrally coordinated cation-anion unit [96]. (b) The wurtzite structure model of ZnO. The tetrahedral coordination of Zn–O is shown [97]

Because of the opposite charged ions, positively charged Zn-(0001) and negatively charged O-(000 $\bar{1}$ ) surfaces create spontaneous polarization along the c-axis [97]. Both normal dipole moment and spontaneous polarization gives charged ZnO (0001) surface. A conductive atomic force microscope tip is used to induce elastic deformation of the nanowires. An external load is connected through which charges flow. Because of the piezoelectric and semiconducting properties of zinc oxide, Schottky barrier forms between the conductive tip and nanowire thus creates electricity [98-100]. Lu et al [99] used p type zinc oxide nanowire array grown on a silicon substrate by thermal vapor deposition method to generate 50-90 mV electrical energy from a single nanowire. Wang et al [98] grown aligned zinc oxide nanowire array on aluminum oxide substrates by vapor liquid solid method. The catalyst used in the process is Au and that's why some nanowire has Au on top of their tip. Gao et al [100] used flexible plastics as substrates which increases the application range of the nanogenerator. The growth temperature was less than 80 °C and large scale production of zinc oxide nanowire array is possible at low cost by their method.

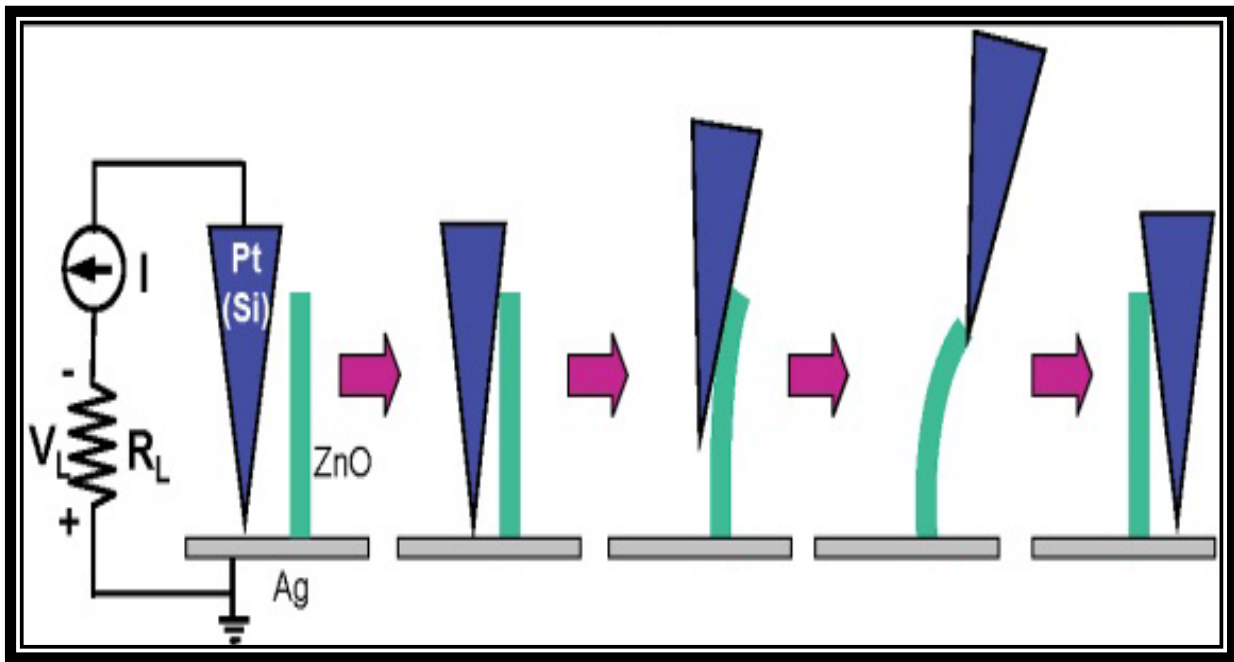


Figure 3.3 Experimental setup and procedures for generating electricity by deforming a piezoelectric ZnO NW with a conductive AFM tip. The base of the NW is grounded and an external load of  $R_L$  is applied, which is much larger than the resistance  $R_I$  of the NW. The AFM scans across the NW arrays in contact mode [98]

### 3.4 ZnO NANOWIRES: GROWTH MECHANISM

Different methods have been developed for synthesis of nanostructure in last decade. In chemical vapor deposition, zinc oxide nanowires and nanorods occurs at high temperature (500-600° C) [101] which limits the use of substrates with low melting point and damages surface of the carbon fiber used as substrate by Thostenson et al [102] because of the exposure to the catalyst. Tseng et al [103] used chemical vapor deposition method to grow zinc oxide nanowires on a selected area. Yang et al [104] has grown ZnO nanowires over Au-coated silicon substrates by vapor liquid solid mechanism. An inert gas is used to carry zinc oxide vapor over substrates on which deposition has to make. Nanowires with different diameters have been achieved by changing the thickness of the Au catalyst film.



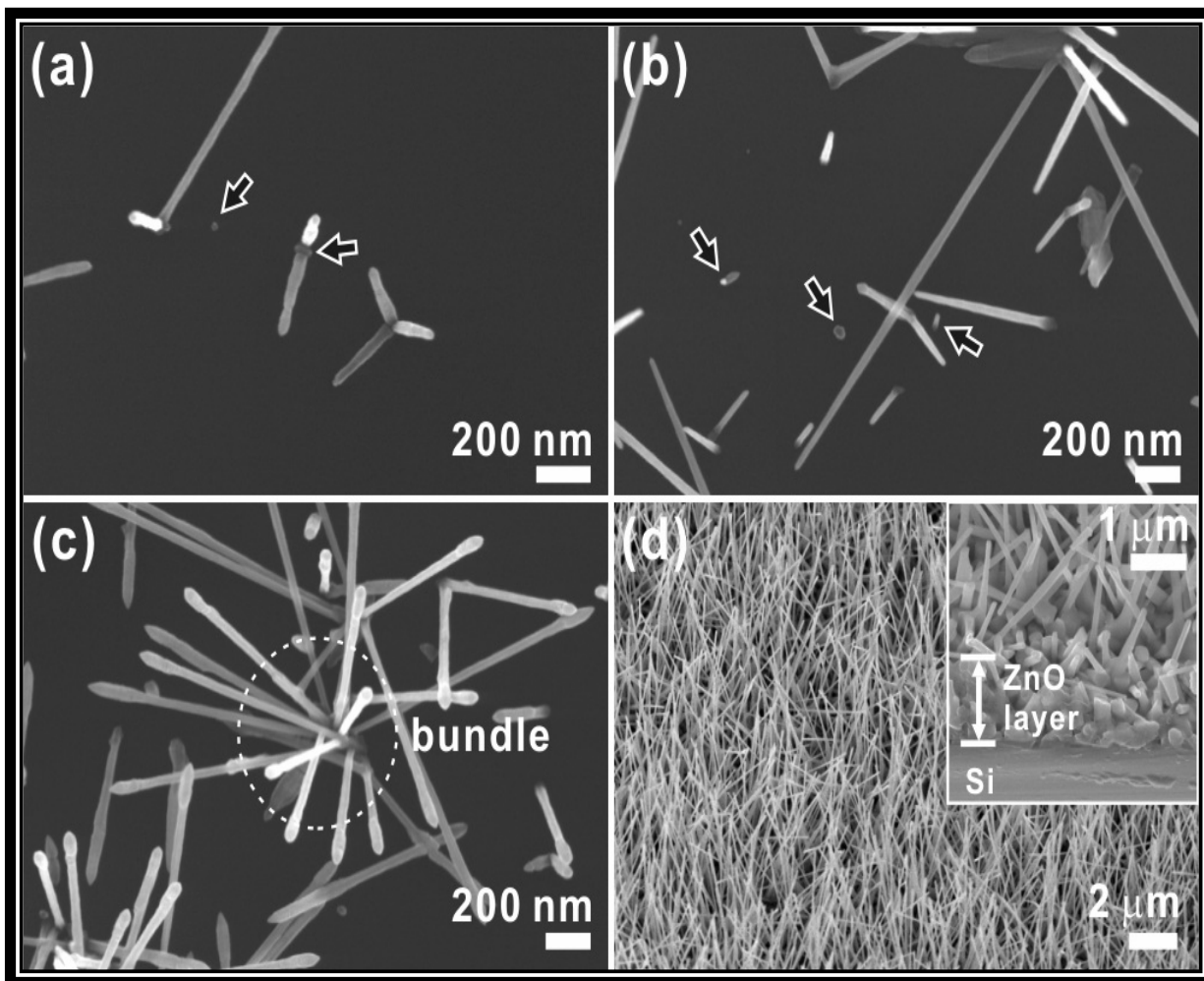


Figure 3.4 SEM images showing nucleation and growth behavior of ZnO nanowires on a Si substrate for reaction times of (a) 30 s, (b) 1 min, (c) 5 min, and (d) 60 min. The inset in (d) is a SEM image of the interfacial region of the nanowires and the substrate [105]

Yu et al [106] used double tube reactor to enrich Zn vapor which increased the nanowires dimension as well as reduced the synthesis temperature. The dimensions, morphology and crystal structure of nanowires are affected by reaction time, temperature and carrier gas flow rate in chemical vapor deposition method. Low synthesis temperature is desirable for better electrical and mechanical properties of nanocomposites. Solution based hydrothermal synthesis process deals with relatively low temperature.

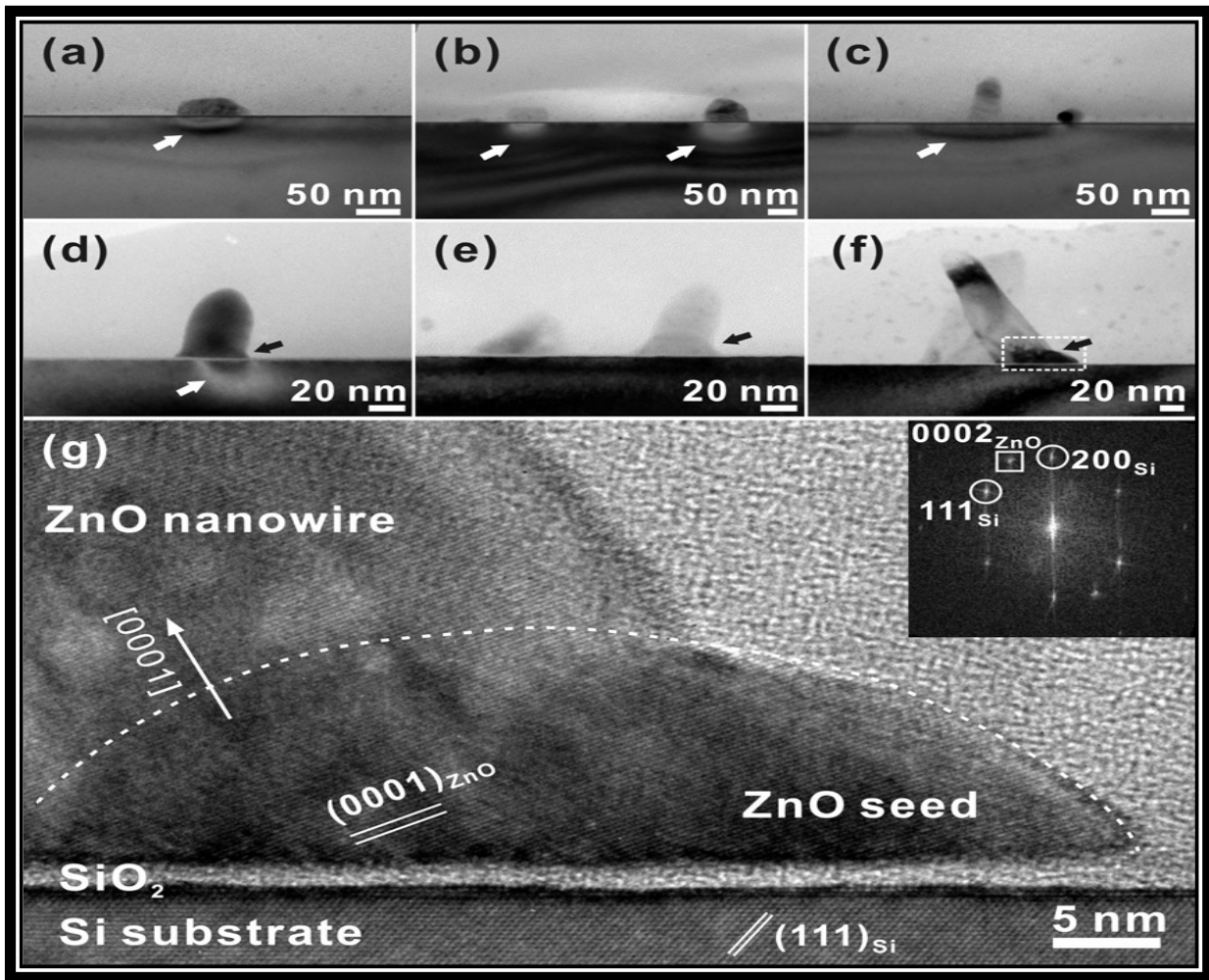


Figure 3.5 Bright-field TEM images of ZnO seeds on a Si substrate grown for (a)–(c) 30 s and (d)–(f) 1 min. (g) HRTEM image of the region indicated by a dotted rectangle in (f). The seeds are clearly shown at the bottom of the ZnO nanowires, as indicated by black arrows in (d)–(f). Contrasts at the Si substrate below the seeds are indicated by white arrows in (a)–(d) [105]

Lin et al [107] used two steps to grow zinc oxide nanowires. First step is to grow nanoparticle from zinc acetate dehydrate-ethanol and sodium hydroxide-ethanol solutions at  $55^\circ\text{C}$  temperature at a volume ratio of 18:7. Then dip coating technique is used to coat the nanoparticles over substrates. The bonding between the nanoparticles and substrates can be increased by annealing which ensures the whiskerization of nanowires. The next step is the growth of zinc oxide nanowires by using zinc nitrate hydrate and hexamethylenetetramine aqueous solution at a temperature of  $90^\circ\text{C}$  for 4 hours. Nanowire can be grown in less than five minutes by using induction heating [108]. The growth of nanowires

depends upon the concentrations of the solutions used, growth temperature. In order to obtain nanowires with better quality, substrate is rinsed with de-ionized water and dried. Nanowires can be grown in longer by changing the growth solution in a regular interval.

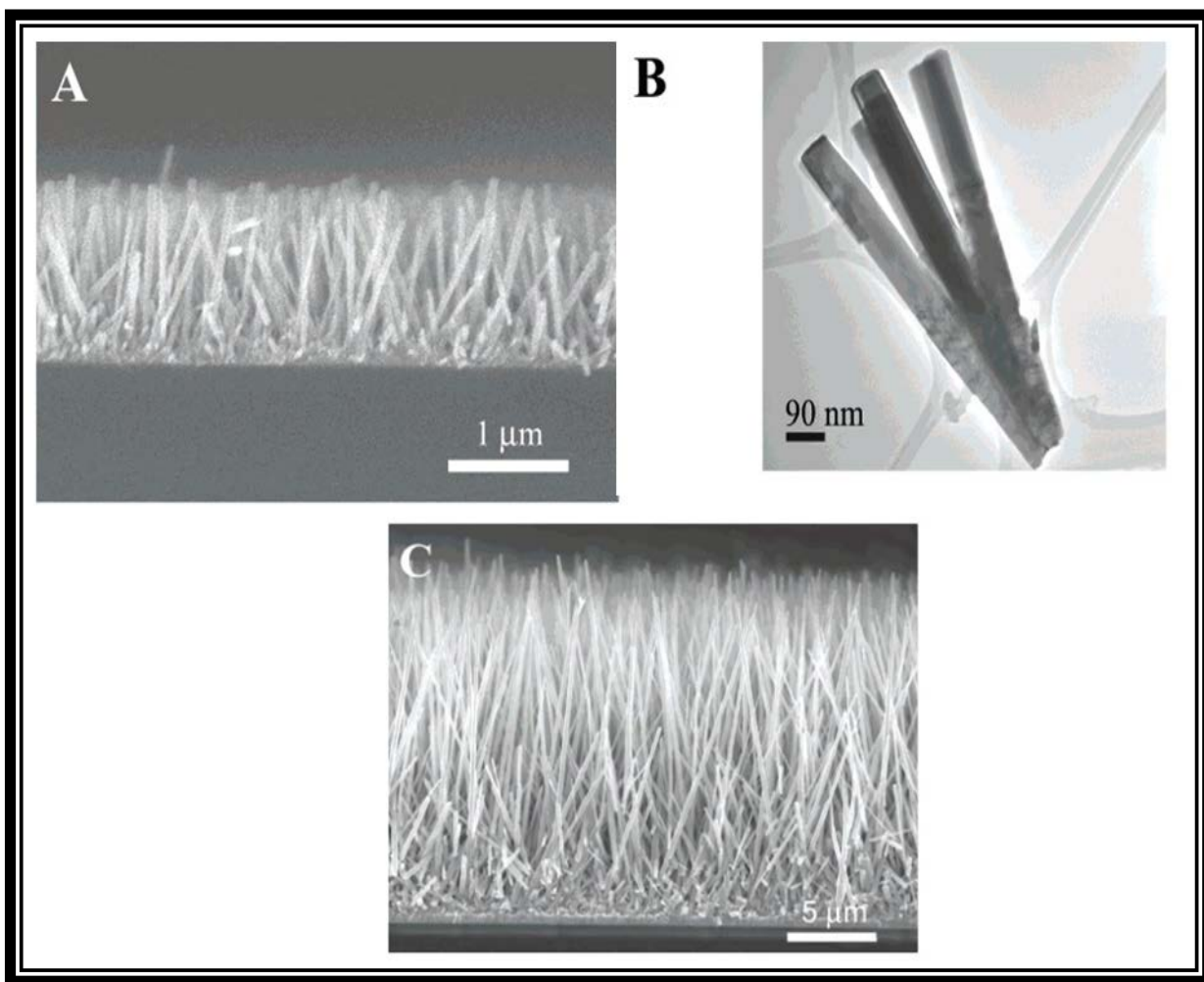


Figure 3.6 Analysis of ZnO nanowire arrays grown in water with zinc nitrate and HMTA at 90 °C. (A) Cross-sectional SEM image of an array grown for 1.5 h on a silicon wafer. (B) TEM image of a cluster of ZnO nanowires removed from an array grown for 1.5 h on a silicon wafer. (C) SEM cross section of a cleaved nanowire array grown with the addition of PEI on a fluorine-doped tin oxide substrate [109]

Greene et al [109] synthesized zinc oxide nanowires by hydrolyzing zinc nitrate with water and hexamethylenetetramine. In the zinc aqueous solution zinc can exist in many monomeric hydroxyl species such as  $\text{ZnOH}^+$ ,  $\text{Zn}(\text{OH})_2$ ,  $\text{Zn}(\text{OH})_3^-$  and their dehydration creates zinc oxide nuclei and continues to grow under condensation. Acidic or basic solution in the range of pH value 5 to 12 and

temperature range 50° C to 200° C is suitable for growth of nanowires. Basic solutions are more important because some metal with two valence ions does not readily hydrolyze in acidic solution. Nanowires can be grown without any additives in solution of pH value more than 9 but for the solution of pH value less than 9 requires HMTA or dimethylamineborane as additives. Nanowires can be grown in longer by changing the growth solution in a regular hour and the diameters will also increase until they come in contact to form thin film. Ko et al. [110], Xu et al. [111], Qui et al. [112] have used polyethyleneimine (PEI) in the growth solution and reported longer and skinner nanowires than nanowires without the polymer in the growth solution. PEI prevents the formation of zinc oxide in the bulk solution. One explanation is that the PEI absorbs the certain crystal faces of zinc oxide clusters and allows in the longitudinal direction of nanowires rather than circumferential direction [109, 113].

### **3.5 LEAD TITANATE NWS FOR DIELECTRIC CAPACITOR**

Use of bulk PTO as dielectric will decrease the energy density because of its low breakdown field strength. That's why polymer can be used as dielectric since they have relatively high breakdown field strength. But polymers have very low dielectric constants which results low energy densities of the capacitors. In order to get higher dielectric constant of ceramic materials and higher breakdown field strengths of polymers, inclusion of ceramic is made in the polymer matrix. High curie temperature and relatively high dielectric permittivity make lead titanate suitable inclusion ceramic. Lewis et al. reported that as the size of inclusion material scales down to nanoscale, the interface properties of polymer inclusion will dominant over the bulk property of the matrix [114, 115]. Poly(vinylidene fluoride) (PVDF) is piezoelectric, pyroelectric and ferroelectric polymer [116]. PVDF has relatively high dielectric constant compare to other polymer [117] and has breakdown field strength of 10.2 MV/m [118]. Inclusion of PTO NWs of high aspect ratio in PVDF can increase the dielectric constant as well as breakdown field strength of the composite. Gregorio et al. [119] reported the increase of dielectric constant of PVDF with the increase of temperature. Hu et al. [120] studied the effect of temperature on dielectric permittivity of PTO nanoceramics and found increasing with the increase of temperature up to 8330 at 1 kHz at curie temperature (490

yet to investigate. In this research work, hydrothermal method is followed to synthesis PTO NWs and PVDF are used as matrix to make polymer composite. Dielectric constant and breakdown field strength are determined to measure energy density of the nanocomposites at different temperature and operating frequency.

### **3.6 LEAD TITANATE: MATERIAL PROPERTIES**

Lead titanate ( $\text{PbTiO}_3$ ) is a ferroelectric material of perovskite tetragonal structure. It has high curie temperature of 490

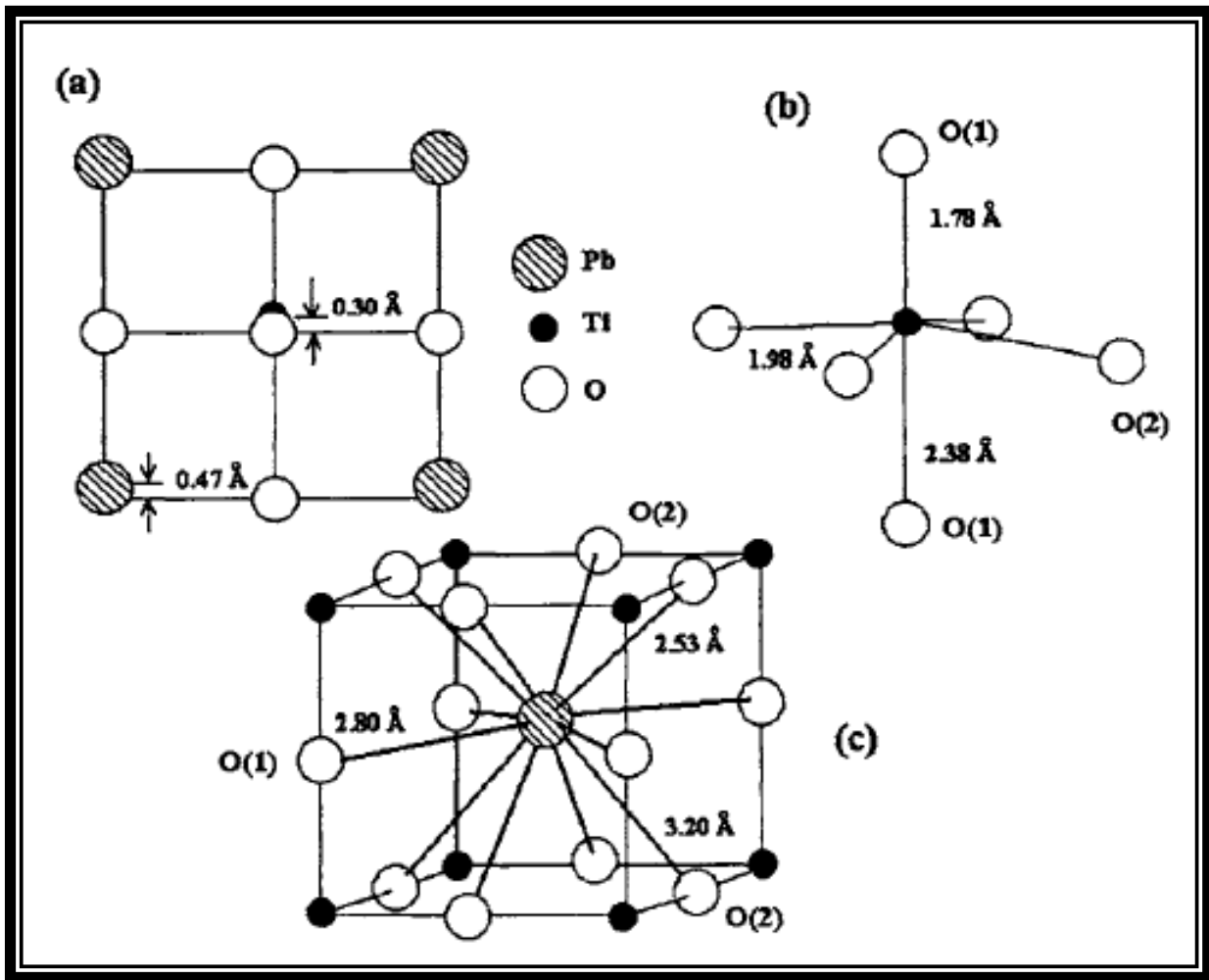


Figure 3.7 Crystal lattice structure of  $\text{PbTiO}_3$ : (a) projection of ionic sites on the (001) plane; (b) environment of the Ti ion; (c) environment of the Pb ion [77]

### 3.7 LEAD TITANATE NANOWIRES SYNTHESIS

Many methods are developed to synthesis one dimensional nanostructure i.e. nanowires, nanorods, nanofibers, nanocubes of lead titanate has been synthesized by sol gel template and molten salt method [130-136]. Sol gel method is widely used to synthesis complex materials due to convenience of experimental equipment. Hernandez et al. [130] synthesized lead titanate nanotubes of 200 nm by using alumina templates. Luo et al. [137] used silicon and alumina templates to synthesis lead zirconate titanate nanotubes of 50 nm diameters and lengths up to 100  $\mu\text{m}$ .

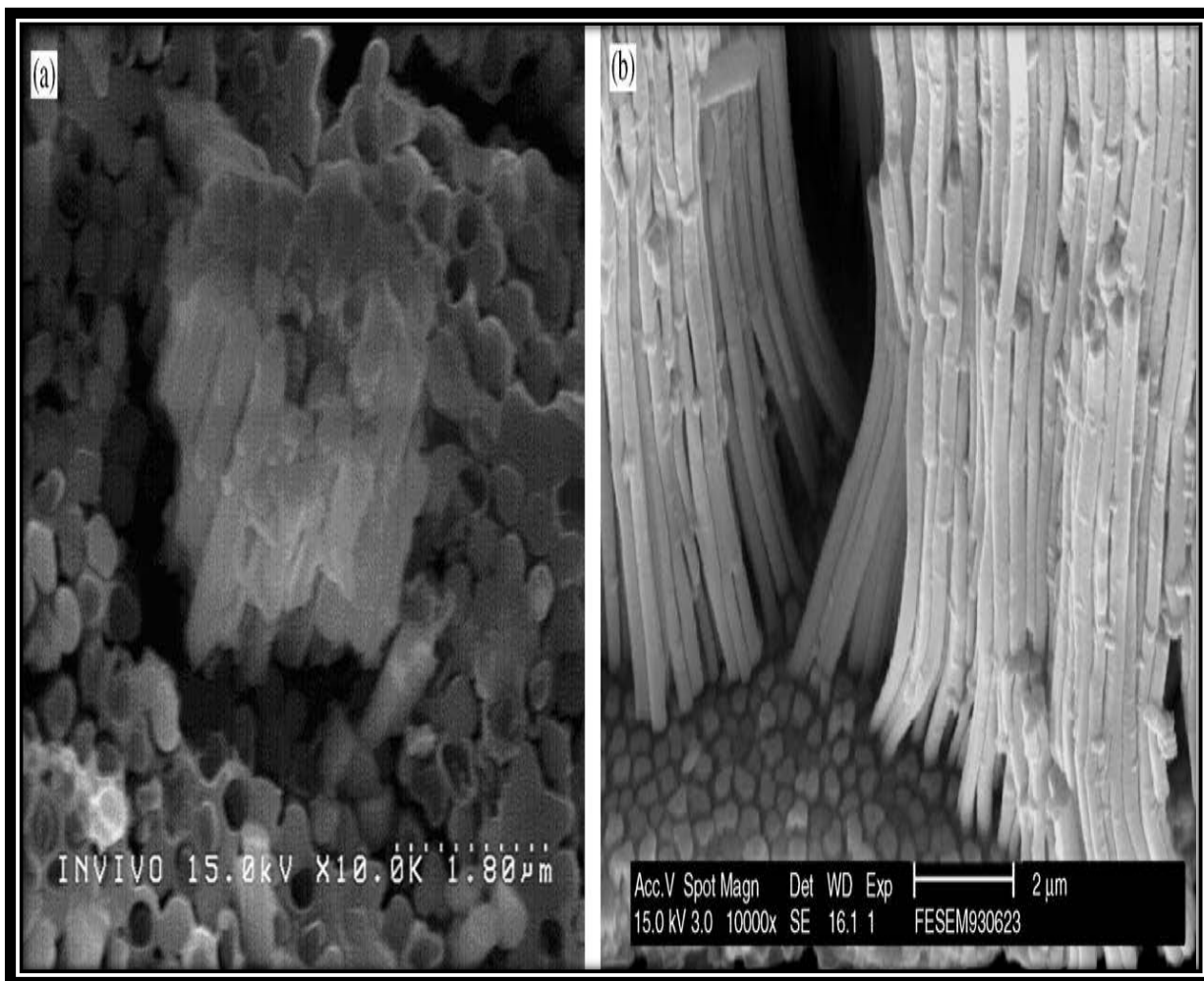


Figure 3.8 SEM micrographs of nanowires formed by liquid-phase deposition method using 200-nm alumina template membranes. (a) Top view image of the PbTiO<sub>3</sub> nanowire arrays grown within an AAO template. (b) Side view image of PbTiO<sub>3</sub> nanowires bundle together after removing the AAO template [132]

Zhang et al. [138] followed sol gel method and used alumina templates to synthesis lead zirconate titanate nanowire array of 45 nm diameters and 6 µm lengths. In the sol gel method templates are dipped in the sol by capillary actions. It becomes difficult for higher concentration sols and small pore diameter templates to fill the pores. In addition to that nanomaterial synthesized from low concentration sol causes shrinkage and crack during the annealing [139]. In order to avoid cracks in nanomaterials, Limmer et al. [139] developed a more complex method called sol–gel electrophoresis deposition which involves special equipment to synthesis lead zirconate nanowires. The precursors and solvents used to make sol gel are very unstable in ambient air and have potentially toxic to human body.

All these limitations of sol gel method lead to the development of novel method. Liquid-phase deposition (LPD) method is developed to prepare metal oxide thin films which involves aqueous solution [140]. Hsu et al. [132] have synthesized lead titanate nanowire arrays by following LPD method and using anodic aluminum oxide (AAO) templates. Hydrothermal method is a template free and most simple synthesis procedure that has been used to synthesis lead titanate nanowires.

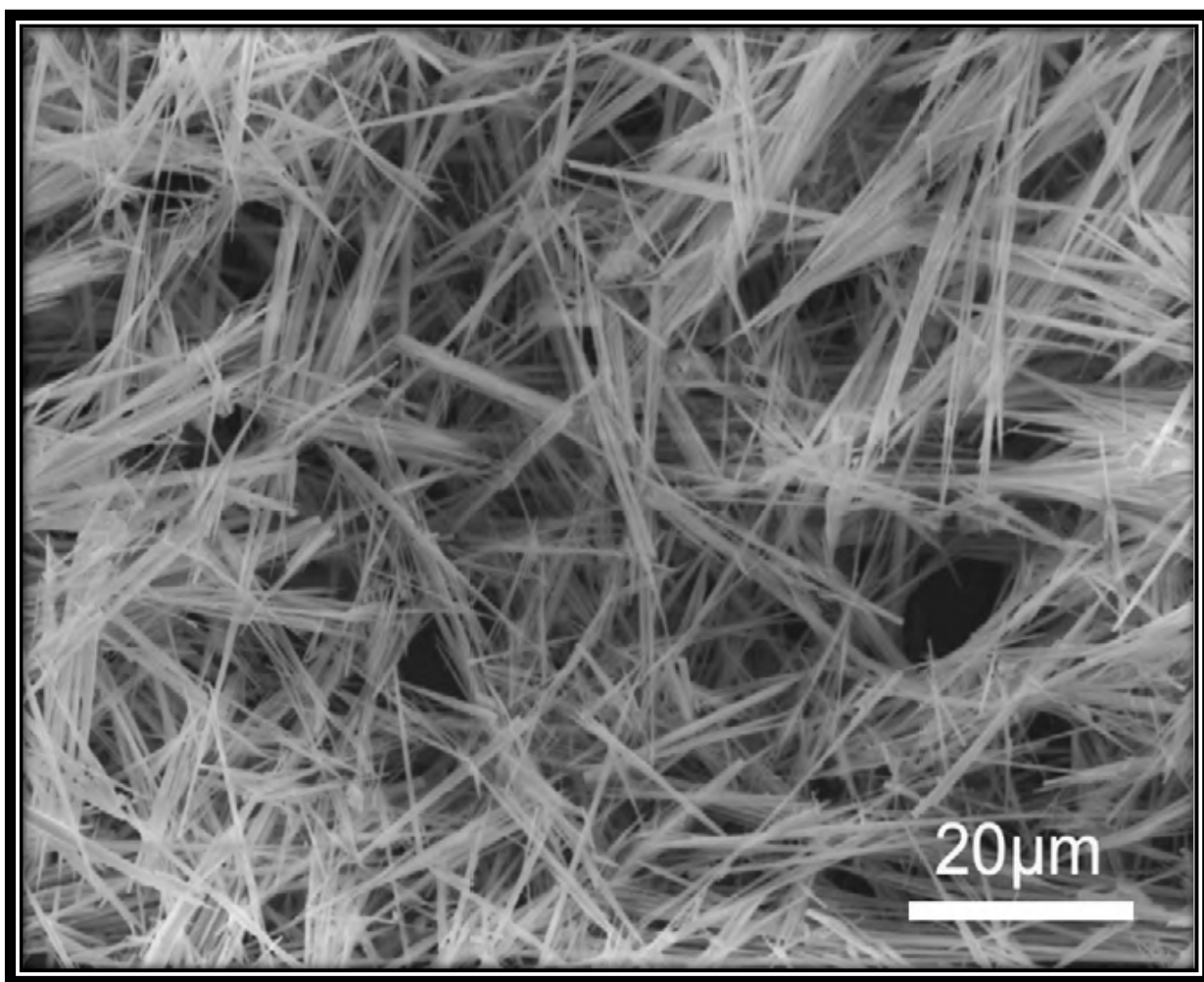


Figure 3.9 SEM image of PX-phase Pb–Ti–O nanowires synthesized by hydrothermal method [141]

It has been reported in previous research work is that the lead titanate powders synthesized by hydrothermal method possess different crystal structures which are perovskite, pyrochlore and tetragonal body centered type and has different morphology depending on reaction conditions [142, 143]. Usually they are referred as PX phase. PX phase PTO nanowires with high length to diameter ratio has potential



application for nanostructures of ferroelectrics for their ferroelectric properties [144]. Hydrothermal method has

## Chapter 4: Experimental Details

### 4.1 GRAPHENE SYNTHESIS

Hummer's method [149] is used to synthesis graphene. Graphite powder (325 mesh, 99%, Alfa Aesar) of 3 g and sodium nitrate ( $\text{NaNO}_3$ , Alfa Aesar) of 1.5 g are mixed in 69 ml of sulphuric acid under mild stirring in ice bath to lower the temperature. After 7 hours 9 g of potassium permanganate ( $\text{KMnO}_4$ , Alfa Aesar) is added in the mixture. After that the solution is heated at 35 °C for 7 hours in a water bath. Additional 9 g of  $\text{KMnO}_4$  is added and heating is continued for 12 hours. The heating setup is shown in figure 4.1.

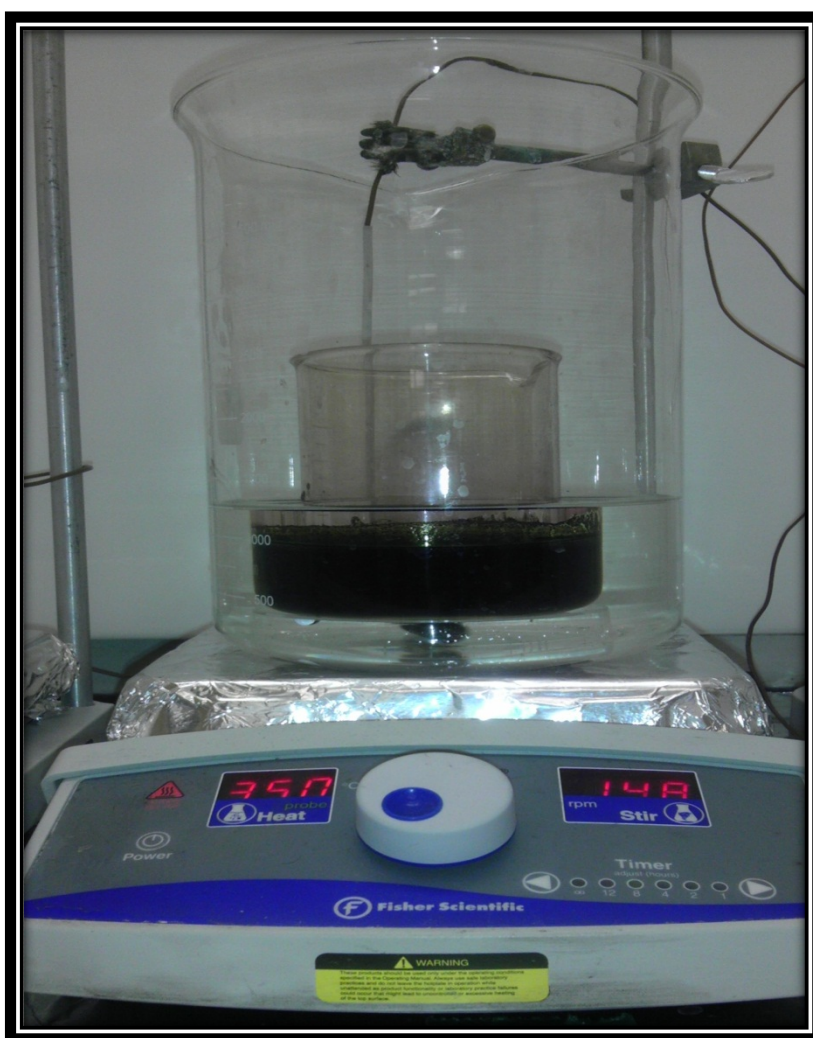


Figure 4.1 Graphite oxidization in water bath at 35 °C

Ice from 400 ml of deionized (DI) water and 3 ml of hydrogen peroxide ( $\text{H}_2\text{O}_2$ ) is mixed with the solution. After melting of ice, final solution is centrifuged at 4000 rpm for 30 min and precipitation is separated. The precipitation is washed with DI water, 30% hydrochloric acid (HCL) and three times with ethanol (200 proof, pharmco) successively. After each wash the solution is sifted and precipitation is separated by centrifuging at 4000 rpm for 30 min. In the next step, precipitation is dried overnight in a desiccator under vacuum to produce graphene oxide (GO). In order to disperse the graphene oxide, a solution of 30 mg/ml GO in DI water is made and sonicated in a bath sonication (Branson, 2510) and tip sonication (Branson, S-450A) is used for 1 h and 5 min respectively. Water is removed from the solution by freeze drying. The solution is freezed using dry ice and methanol mixture. Subsequently the mixture is brought at low pressure by a freeze dry machine which allows water vaporize without boiling. Later graphene oxide is reduced by using a tube furnace (Lindberg blue M) in argon atmosphere at 1050 °C. For the first 300 °C temperature ramp of 1 °C/min is used and from 300 °C to 1050 °C the temperature increase rate of 20 °C/min is used.

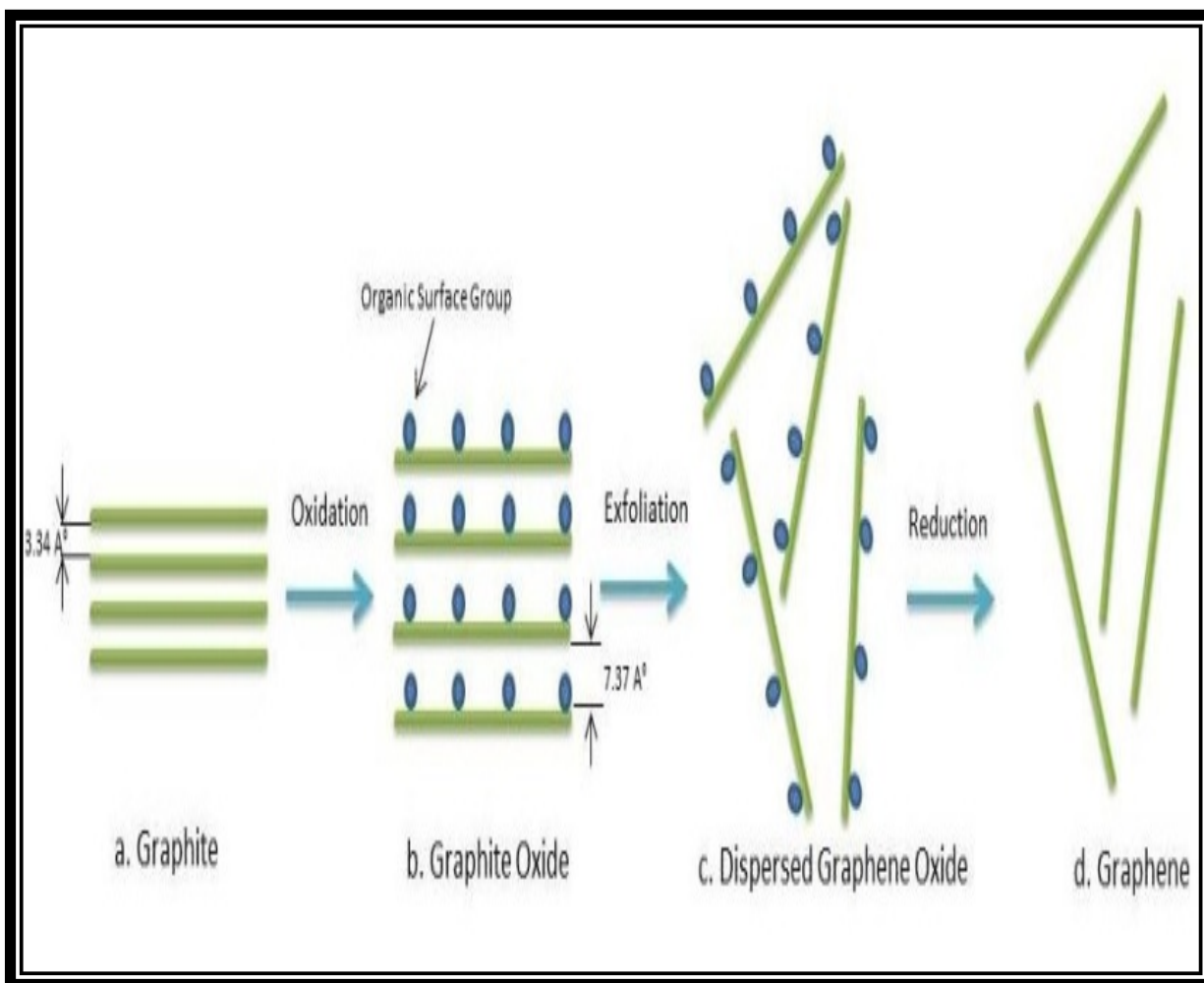


Figure 4.2 Schematic presentation of the graphene synthesis steps a) Natural graphite with inter layer spacing  $3.34 \text{ \AA}$ <sup>23</sup> b) Organic surface groups take place within the layers for oxidation and inter layer spacing becomes about  $7.37 \text{ \AA}$ <sup>23</sup> c) Graphite oxide solution is exfoliated by sonication and becomes dispersed graphene oxide solution d) Freeze dried graphene oxide solution is reduced to graphene

## 4.2 ZINC OXIDE NANO PARTICLE SOLUTION

Zinc acetate dehydrate ( $\text{Zn} (\text{CH}_3\text{COO})_2 \cdot 2\text{H}_2\text{O}$ , 99.999% purity, sigma aldrich)(12.5 mM) is dissolved in ethanol (200 proof, purity

60 °C under vigorous stirring. After cooling to room temperature, additional ethanol is added in order to dilute to make a concentration of 5.7 mM for the final solution.

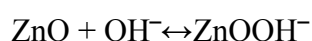
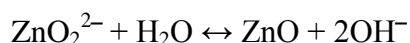
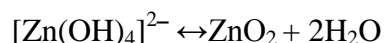
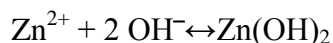


Figure 4.3 ZnO Nanoparticle solutions are mixing on hot plate under vigorous stirring at 55 °C

These two solutions are mixed at a ratio of 18:7 (zinc acetate dehydrate ethanol to sodium hydroxide ethanol) at a temperature of 55 °C for 30 minutes. In order to mix these two solutions properly, at first zinc acetate dehydrate ethanol solution is brought to 55 °C on a hot plate and

temperature is monitored by a thermocouple. When the temperature of the solution is 55 °C, sodium hydroxide ethanol solution is slowly introduced to the solution with the help of plastic pipette under vigorous stirring.

The reactions involved in formation ZnO seed particles are as follows-



In all cases, the top of the beakers are covered with aluminum foil while heating. Otherwise solvent (ethanol for nanoparticle solution and water for growth solution) could escape the solution in terms of evaporation and change the concentration of the solution. Final solution is kept inside a freezer which keeps the nanoparticle solution useable for longer time. Nanoparticle solution can be used as long as it is transparent and clear in naked eye.

### 4.3 COATING SUBSTRATE WITH ZnO NANOPARTICLES

Carbon cloth (made of carbon fiber, diameter ~7 µm) of 50 mm X 30 mm is glued (Devcon, 5 minutes epoxy) on the edges. Then carbon cloth is washed in bath sonication (Branson, 2510). Acetone, Deionized water (DI) and ethanol is used as cleaning solvent. Carbon cloth is taken in a beaker with cleaning solvent and bath sonication is performed for 10 minutes for each solvent. Then carbon cloth is dried at ambient temperature in open air. As synthesized graphene and dried carbon cloth are taken on a glass petri dish, enough nanoparticle solution is dropped to soak them for 10 min and subsequently annealed on a hot plate at 150 °C for 10 minutes to enhance adhesion between the substrates and nanoparticles. This soaking and annealing is repeated two more times to ensure the mass coating of ZnO nanoparticle all over the carbon fibers and graphene. Graphene is coated with ZnO nanoparticle without cleaning.

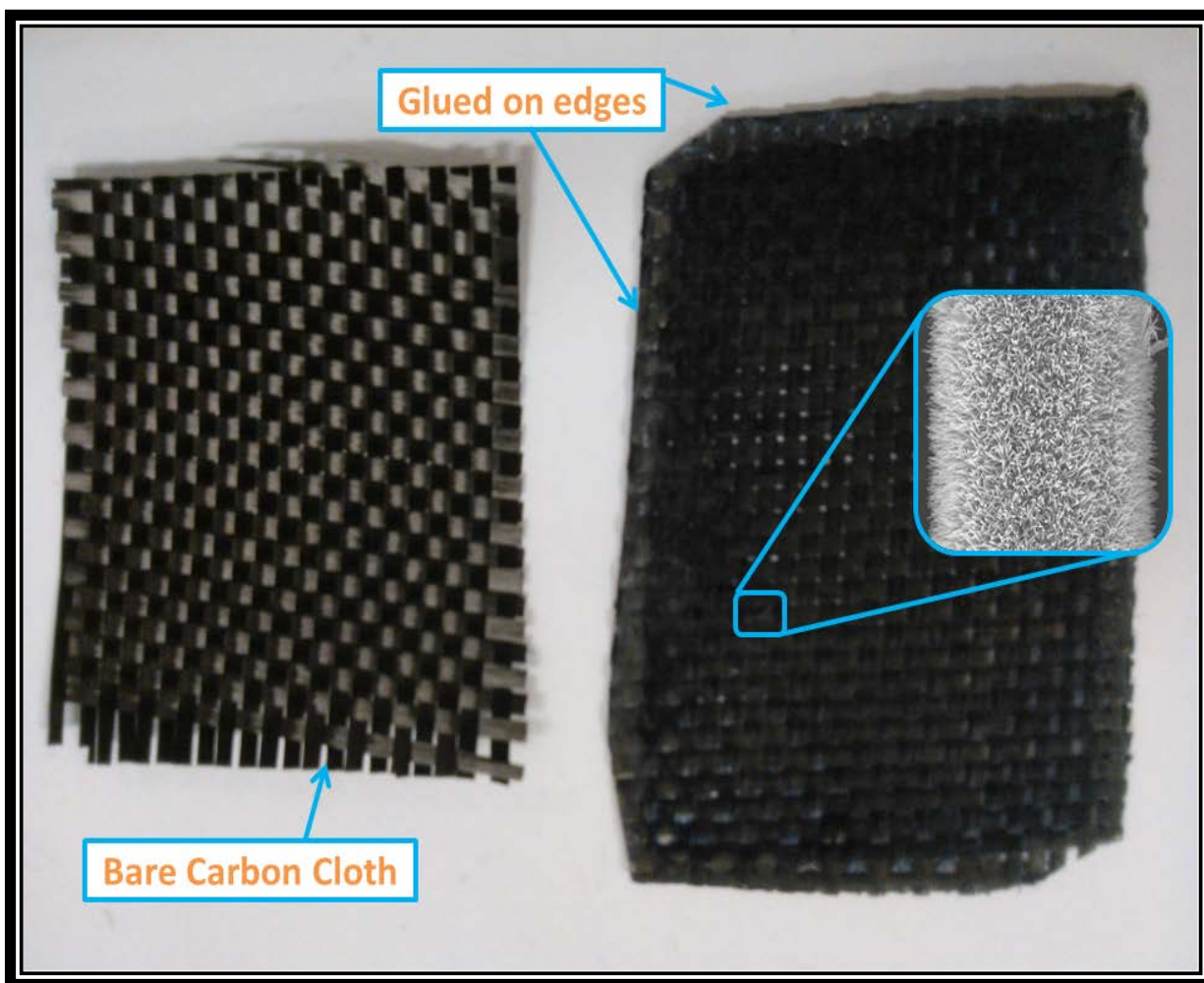


Figure 4.4 Bare carbon cloth on the left hand side; ZnO NWs coated carbon cloth glued on the edges

#### 4.4 ZnO NANOWIRES: HYDROTHERMAL GROWTH

Zinc oxide nanowires are grown by low temperature hydrothermal method [113]. An aqueous solution of 25 mM zinc nitrate hexahydrate ( $\text{Zn}(\text{NO}_3)_2 \cdot 6\text{H}_2\text{O}$ , 99.9% purity, sigma aldrich), 25 mM hexamethylenetetramine (HMTA) ( $\text{C}_6\text{H}_{12}\text{N}_4$ , 99.9% purity, sigma aldrich) and 5-7 mM Polyethylenimine (PEI, Branched, molecular weight 800 gm/mol, sigma aldrich) are prepared at room temperature. Substrates coated with ZnO nanoparticles are immersed in growth solution when the temperature is at 85 °C. The growth is done in a glass beaker and solution temperature is maintained at 85 °C by using a thermocouple and hot plate. For carbon cloth, growth time of 8h is used with a growth solution of 2 liters. Growth solution of 500 ml is used for reduced graphene for 2 hours of ZnO NWs growth. After the reaction is complete, samples are taken out of the solution to rinse with de-ionized



water and dried at 100 °C on a hot plate. Chemical reactions involved in formation of ZnO nanowires are as follows-

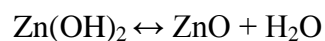
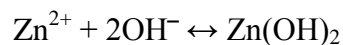
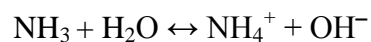


Figure 4.5 ZnO nanowire growths on carbon fiber at 80 °C

#### 4.5 ANODE PREPARATION

Bare carbon cloth of 12 mm diameter and ZnO NWs coated carbon cloth of the same diameter is used as anode for LIB. Copper foil (MTI corp., thickness 0.009 mm) of 12 mm diameter is used as



current collector placed on the carbon cloth without using any kind of binder. To make graphene and ZnO NWs coated graphene anode, Polyvinylidene fluoride (PVDF, MTI corp., purity  $\geq 99.5$ , Molecular Weight 600,000) is used as binding material. PVDF is dissolved in N-Methyl-2-pyrrolidone (NMP, MTI corp., purity  $\geq 99.5\%$ ) at a 1:10 weight ratio by heating at 80 °C. Slurry of 90 wt% of graphene and 10 wt% of PVDF is made by using PVDF-NMP solution. For ZnO NWs/graphene, 80: 20 wt% ratio is used with PVDF. Excess NMP is used to ease the mixing of slurry. Both horn and bath sonication is used to make a homogeneous mixture. A micrometer adjustable film applicator (MTI corp.) is used to cast the slurry on copper foil wrapped on glass plate (MTI corp.). Small amount of ethanol is dropped between copper foil and glass plate to get perfectly plane surface. The casting is dried in an oven at 120 °C for 12 hours in air environment. After drying, cut into 12 mm diameter to use as anode in LIB.

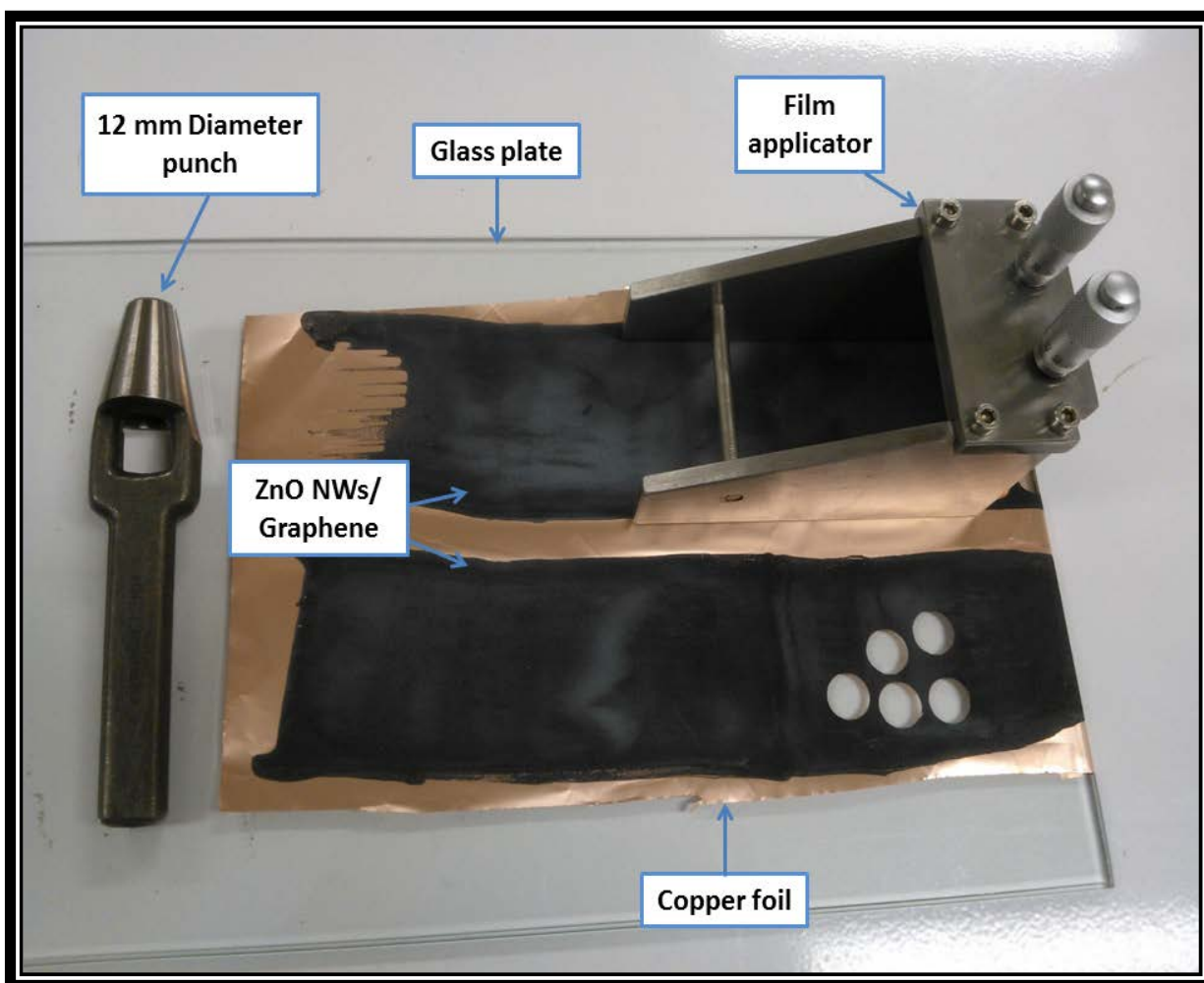


Figure 4.6 Casting slurry on Cu foil to make anode and cut later by 12 mm diameter punch

#### 4.6 COIN CELL ASSEMBLY

Coin cell CR 2032 is assembled using bare carbon cloth, ZnO NWs arrays/carbon cloth, graphene and ZnO NWs arrays/graphene anode. Each of the anodes is investigated against 12 mm diameter single side LiCoO<sub>2</sub> coated on Al foil (MTI corp., 0.1 mm thickness). 1 M LiPF<sub>6</sub> in ethylene carbonate (EC), dimethyl carbonate (DMC), diethyl carbonate (DEC) organic solvent at 1:1:1 volume ratio is used as electrolyte as received (MTI corp.). Since electrolyte is very sensitive to moisture, electrolyte package is opened in argon (Purity 99.999%) filled glove box (LABstar, MBraun).

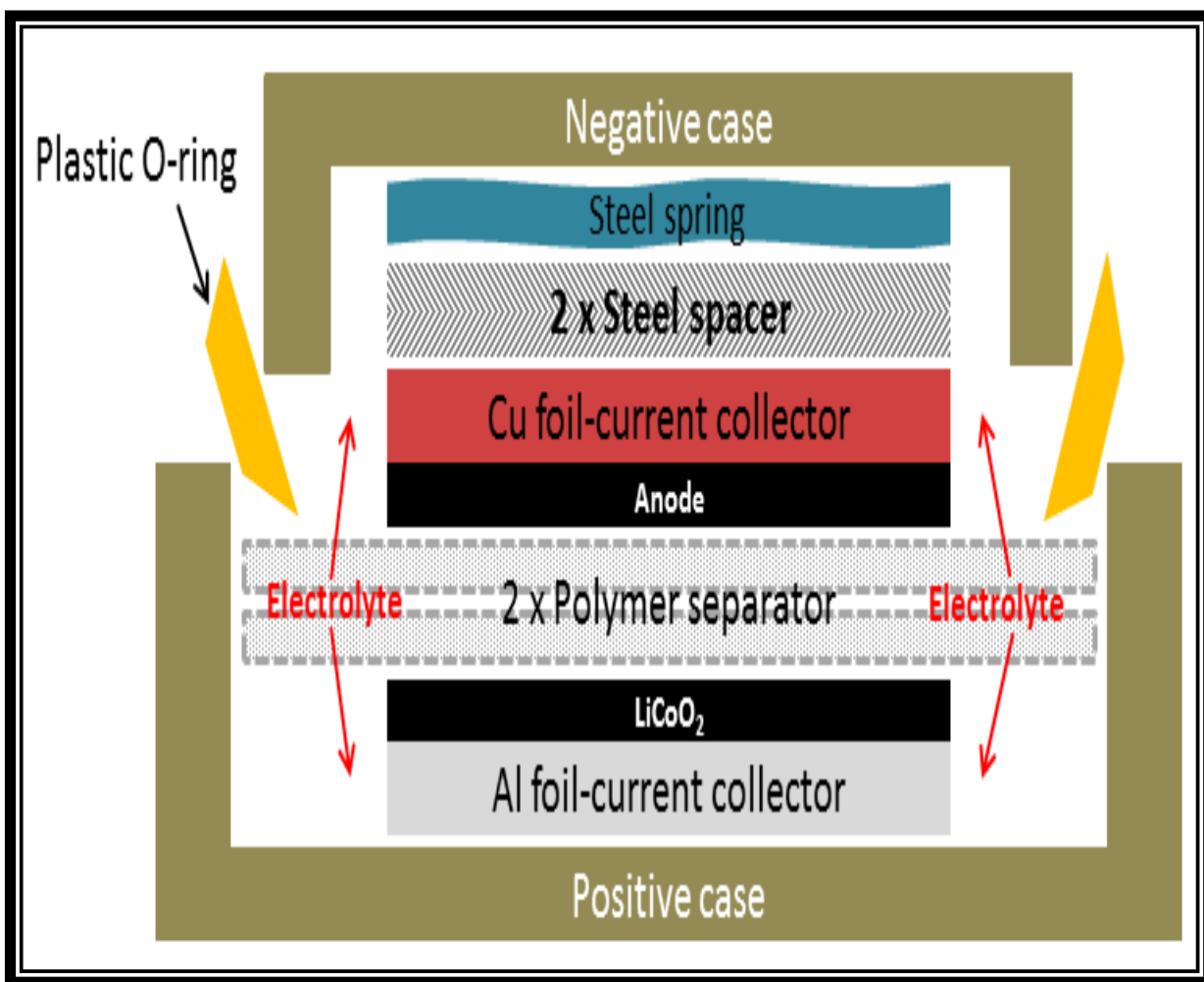


Figure 4.7 Cross sectional view of LIB coin cell shows the sequence of components

The moisture and oxygen content inside glove box is maintained less than 0.01 ppm during the assembly of coin cell. As prepared electrodes are used as anode against LiCoO<sub>2</sub> cathode. Microporous

polyethylene (MTI corp., 0.025 mm thickness, 36-44 % porosity) cut into 19 mm diameter disk is used as separator. Commercial battery cases, spacer and spring are used as received (MTI corp.).

A very specific sequence is followed for the assembly of LIB shown in figure 4.7. Cathode is placed on positive case facing the active material up. Three drops of electrolyte are added on cathode followed by two separators and in between them another two drops of electrolyte is added. After that two more drops of electrolyte and anode facing active material down are added. Copper foil cut in 12 mm diameter is placed on carbon cloth anodes. The rest of the sequence is as follows: two spacers, spring and negative case. Coin cells are sealed by applying 750 psi pressure with a crimping machine (MTI corp.). After assembly excess electrolyte is wiped by tissue and plastic tweezer is used for holding batteries to avoid shorting.

#### **4.7 LEAD TITANATE NANOWIRES**

PTO nanowires were synthesized using a hydrothermal method similar to those previously reported [150, 151]. The process can be simplified into two steps which are described as follows.

##### **4.7.1 Gel Preparation**

Titanium (IV) n-butoxide (TNBT) (Acros Organics, 99%) is dissolved in ethanol (200 proof, purity

#### 4.7.2 PTO Nanowire Growth

The gel is dispersed in 100 ml of DI water followed by an inclusion of lead (II) nitrate ( $\text{Pb}(\text{NO}_3)_2$ ) (Fischer Chemical, 99%) of 5.465 grams and potassium hydroxide (KOH) (Acros, pellets, 85%) of 4.208 grams. Polyvinyl alcohol (PVA) (Aldrich chemistry, 99+% hydrolized) of 0.06 grams is dissolved in DI water at 80 °C for 30 minutes. After PVA DI water solution is cooled to room temperature, mixed with gel solution under vigorous stirring for 30 minutes. Final solution has concentrations of 0.11 M  $\text{Pb}(\text{NO}_3)_2$ , 0.5 M KOH and 0.4 g/L PVA. After continuous stirring for 30 minutes, solution is transferred into a 200 mL Teflon lined stainless steel autoclave with a fill factor of 80%.

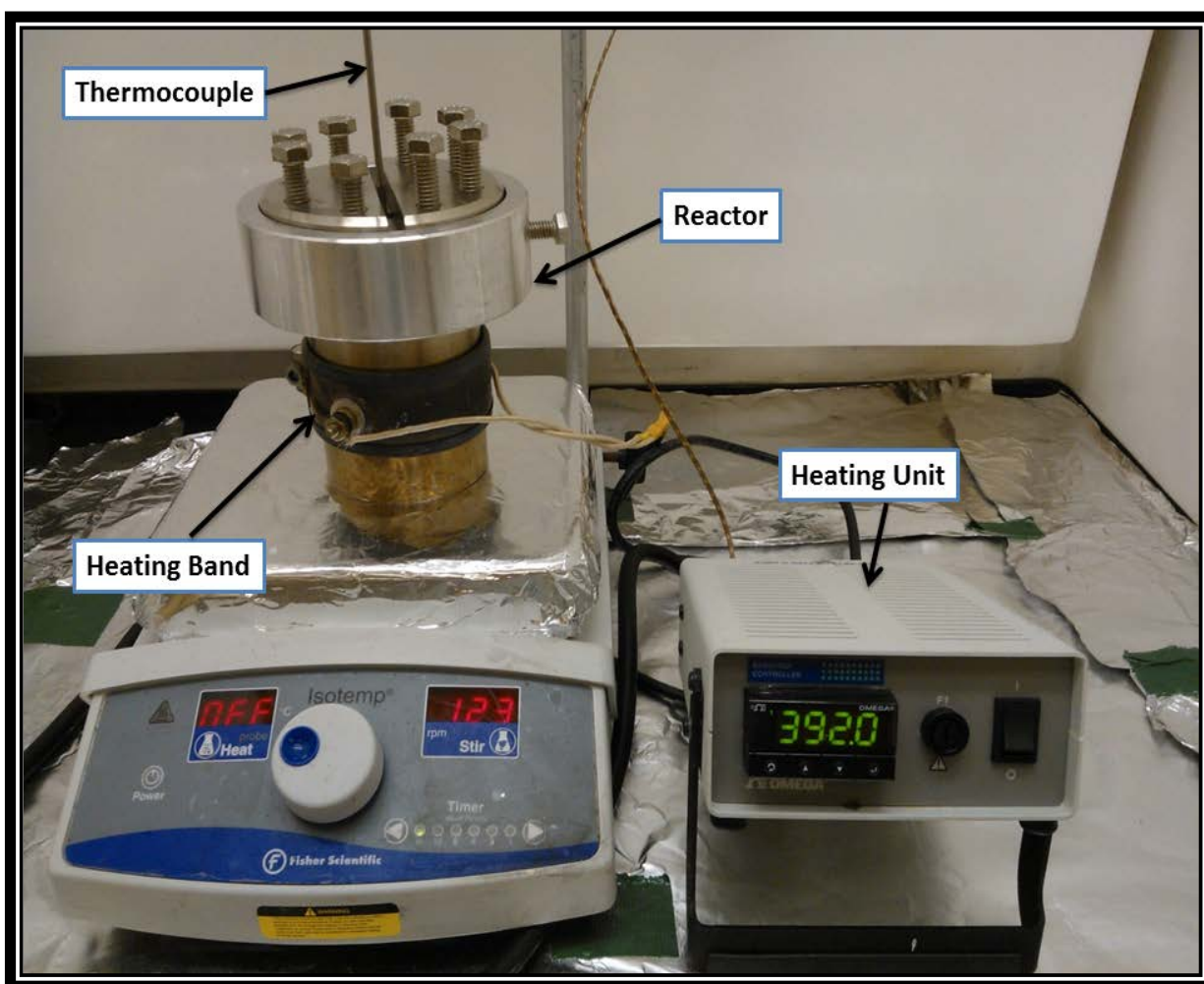


Figure 4.8 Setup for PTO nanowire growth by hydrothermal method

The reactor is placed on a hot plate with a heating band to undergo hydrothermal reaction at 200 °C (392° F) for 4 h under vigorous stirring. A heating unit (Omega benchtop controller) is used to maintain the reactor temperature. After cooling down to room temperature, PTO powder is recovered through vacuum filtration, washed with DI water and ethanol for three times, and dried at 80 °C for 12 h. Finally, PTO powder is placed inside an alumina crucible with lid to cover the top and annealed at 600 °C for 2 h in a high temperature furnace (Lindburg/blue M, Max. 1100 °C) to obtain crystallized PTO nanowires.

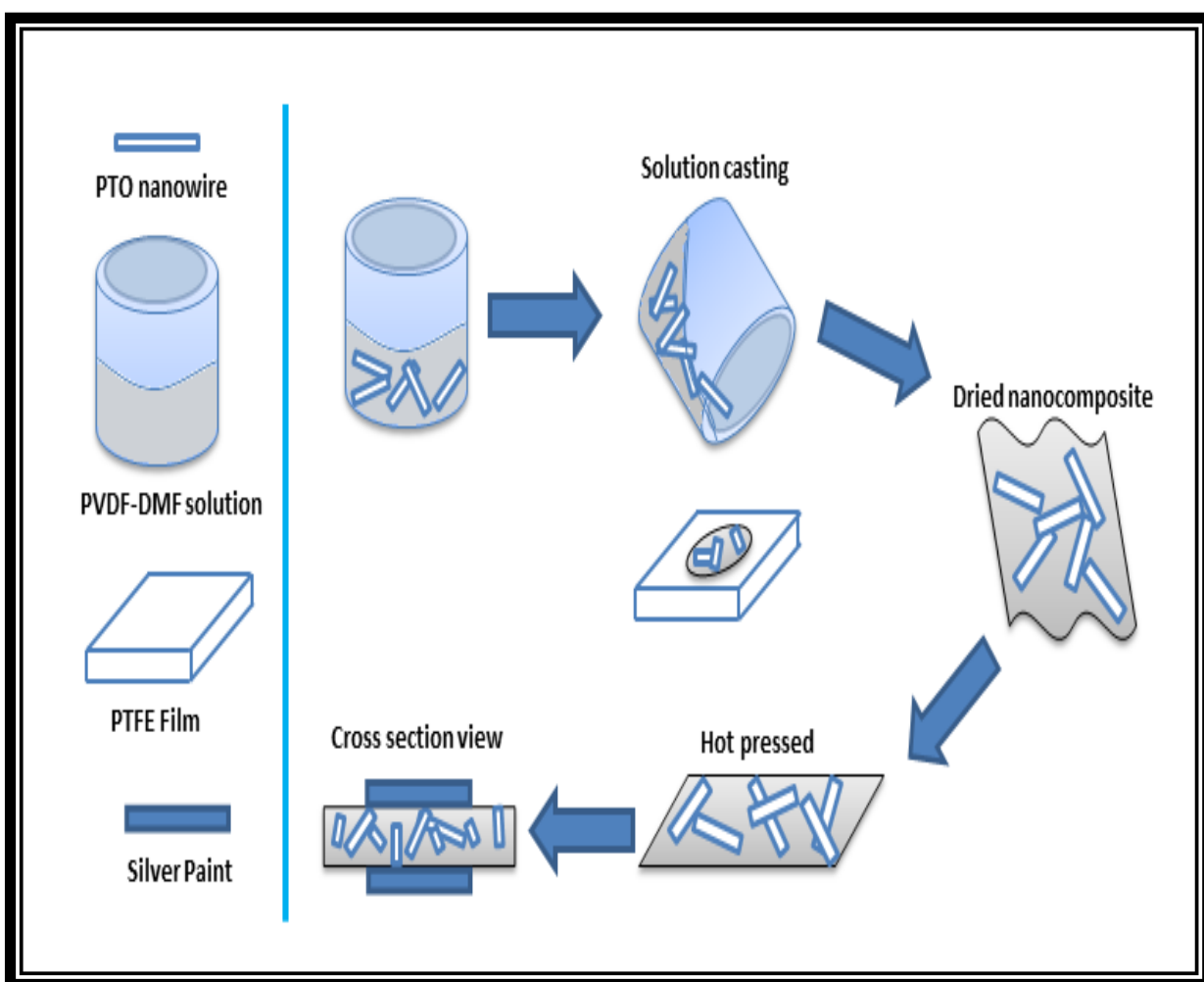


Figure 4.9 Schematic diagram of the manufacturing process of nanocomposites

#### **4.8 PTO NWS-PVDF NANOCOMPOSITE**

Polyvinylidene difluoride (PVDF) (Aldrich, Mw~53,4000) and DMF (Acros, 99.8%) are measured at a 1:10 weight ratio inside a glass vial. The vial is put inside a glass beaker filled with water and water is maintained at 80 °C for 30 minutes to fully dissolve the PVDF. Nanocomposites are prepared by dispersing PTO nanowires into PVDF/DMF solution by manual stirring and horn sonication (Branson, S-450A) until nanowires are dispersed uniformly throughout the solution. Subsequently, solution is casted onto a PTFE film and dried at 80 °C for 12 h. In order to achieve a uniform and small thickness over the entire film, nanocomposites are hot pressed at 160 °C for 15 minutes under a constant pressure of 1 ton (Carver, 3850). Nanocomposites are kept under 1 ton of pressure as they cool down to room temperature. Finally, top and bottom surfaces of nanocomposites are coated with silver paint to make electrodes for electrical testing.

#### **4.9 SAMPLE CHARACTERIZATION**

Surface structures of synthesized samples are analyzed by scanning electron microscope (Hitachi S4800). Crystal structures of the samples are studied by X-ray diffractometer (Bruker D8 Discover) using Cu K $\alpha$  radiation ( $\lambda=1.54056 \text{ \AA}$ ) at RT.

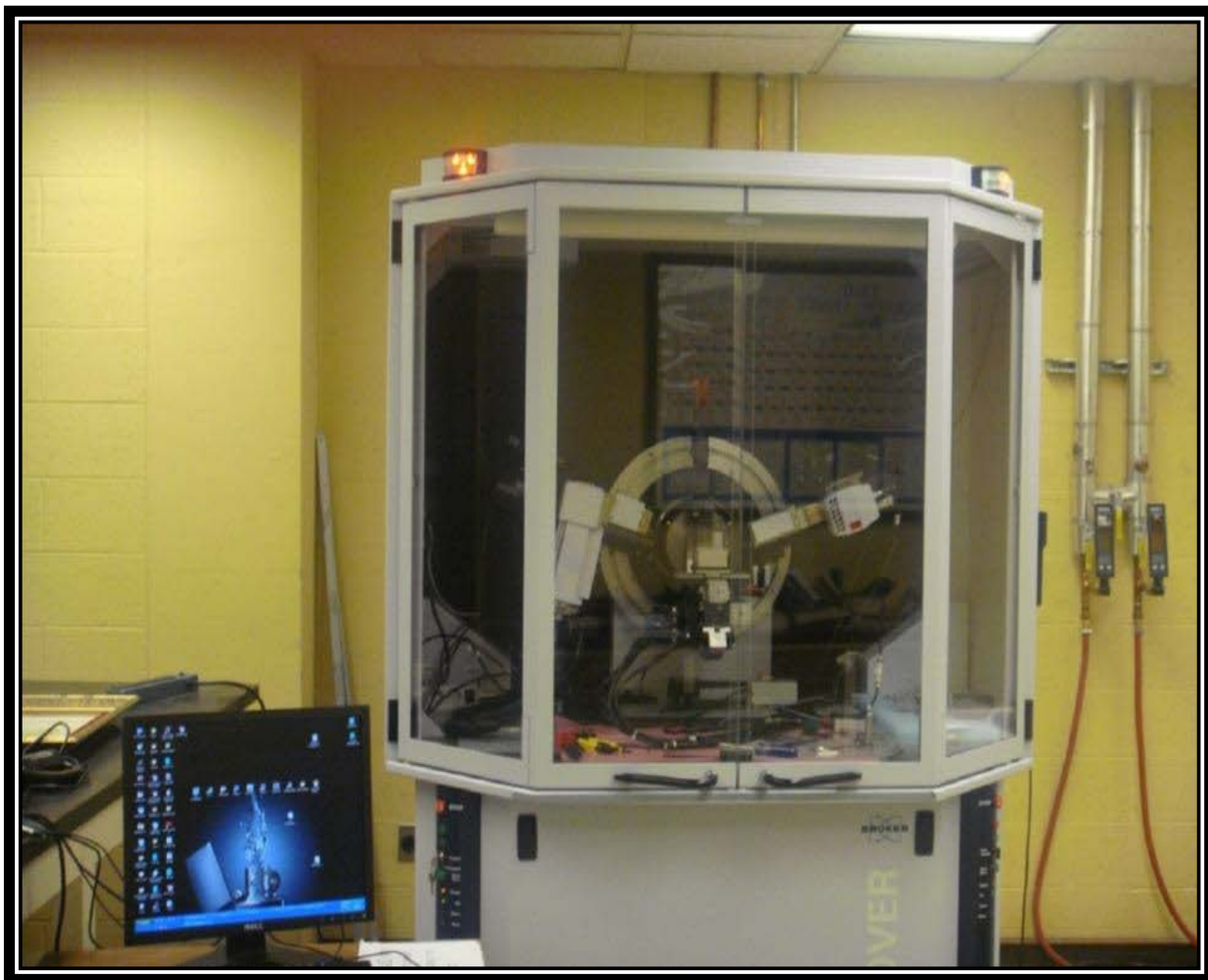


Figure 4.10 Bruker D8 Advance X-ray diffractometer used to characterize samples





Figure 4.11 Hitachi S-4800 Scanning Electron Microscope used to characterize samples

#### 4.9.1 Calculating Active Materials of Electrodes

Weights of carbon cloth and graphene are measured before synthesizing ZnO NWs on them by a high precision weighing machine (Sartorius, MC 210S). After growing NWs their weights are measured again. From the difference of weights, the percentage of weight increased because of NWs is calculated. The percentages of weight increase of carbon cloth and graphene because of NWs grown on them is 1.53 % and 34.23% respectively. The total weights of bare carbon cloth and graphene are used as active material. For ZnO NWs coated carbon fiber and graphene, the active material is calculated by subtracting the weight of NWs for individual case.

#### 4.9.2 Characterizing as Prepared Electrodes

The performances of LIBs assembled are analyzed by an 8 channel battery analyzer (MTI).



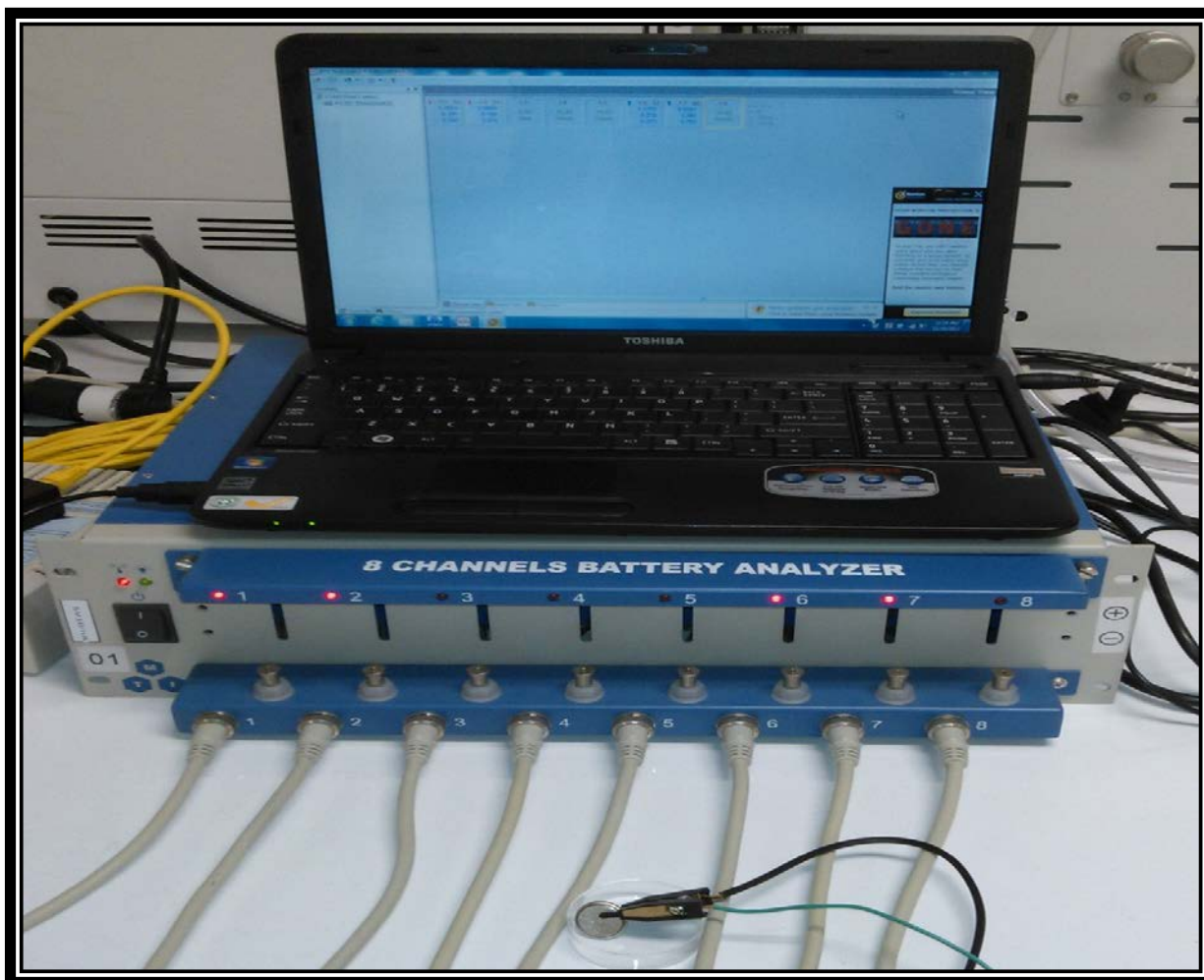


Figure 4.12 Performance analyzing LIB by battery analyzer

The battery is connected to the analyzer with clip which has two metal terminals. Batteries are placed on a plastic petridish to void any metal contact while testing.

#### 4.9.3 Characterizing Nanocomposites

Dielectric constant and dielectric loss tangent of the nanocomposites are measured by HP 4284A LCR meter at 1 Vrms with a parallel equivalent circuit setup which has a frequency range from 100 Hz to 1 MHz. Breakdown voltage of nanocomposites are measured using high voltage power supply (30 KV, PO3HP2, Acopian), digital oscilloscope (DS1102E, Rigol), digital multimeter and function/arbitrary waveform generator (20 MHz, 33220A, Agilent) and all the test is done according to ASTM standard (ASTM D149-09) [152].

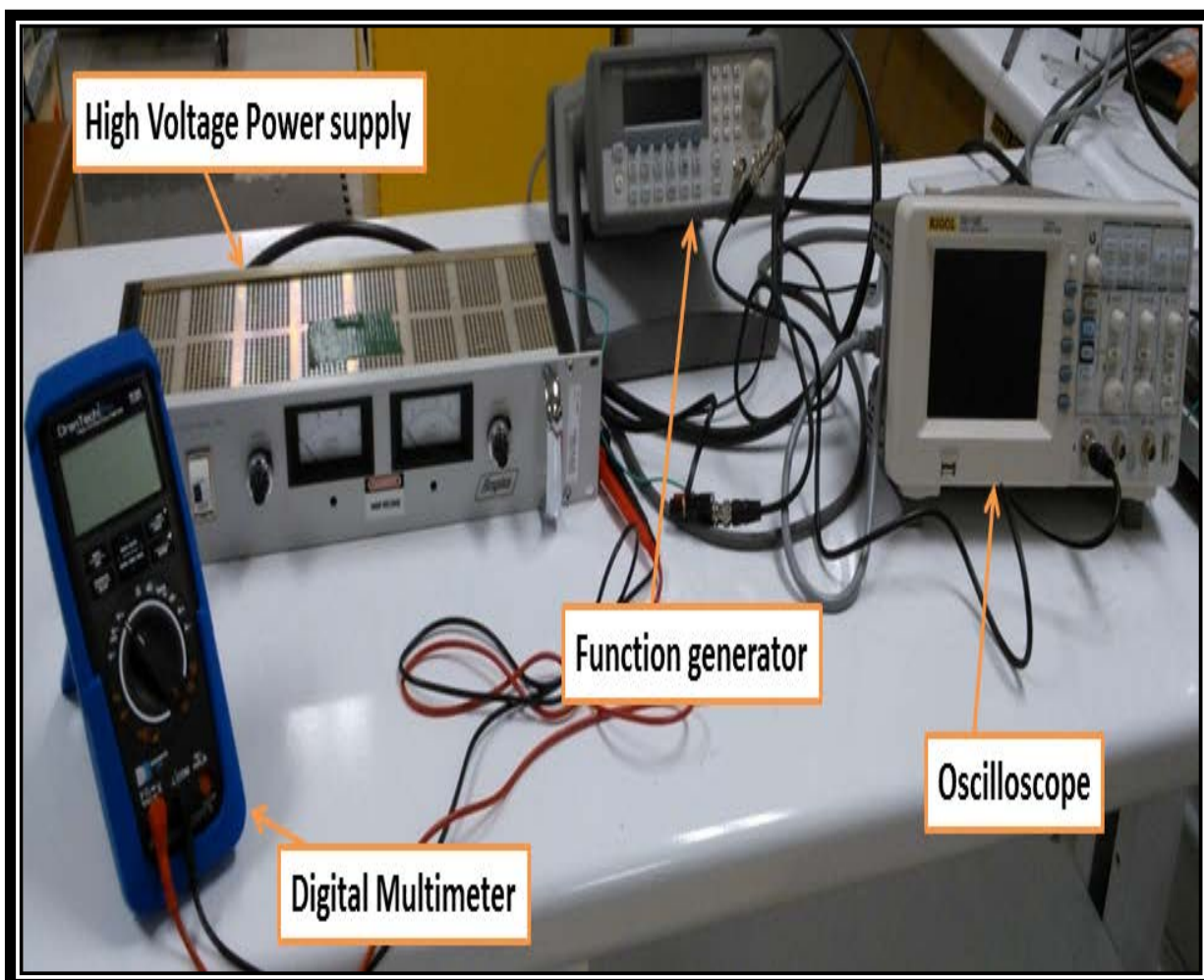


Figure 4.13 Experimental setup to measure breakdown voltage of nanocomposites

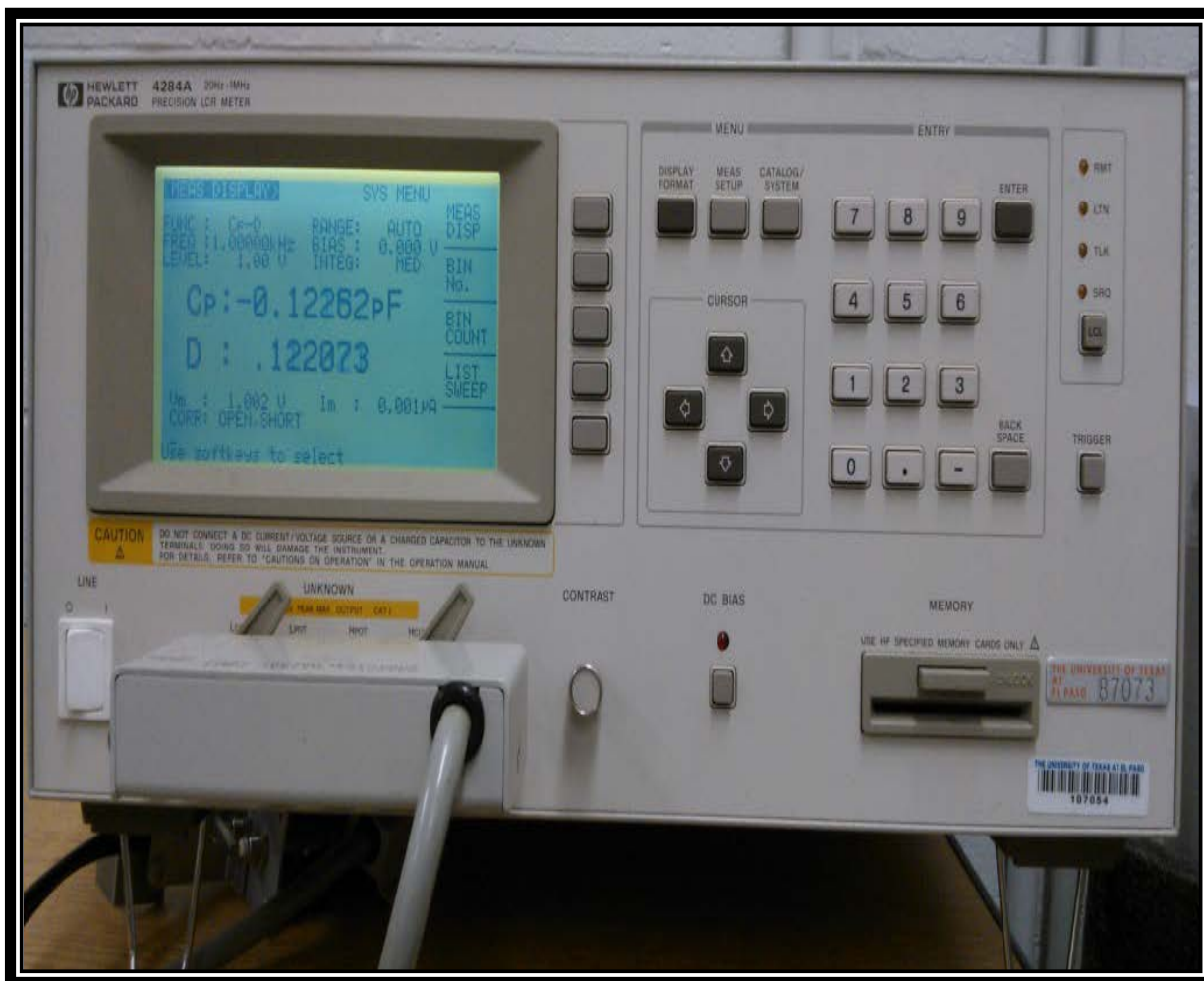


Figure 4.14 LCR meter used to measure dielectric constant and dielectric tangent loss of nanocomposites

In order to measure the dielectric constant and dielectric loss tangent at different temperature and breakdown voltage, silicon oil which has very dielectric constant is used to dip the composites into and the beaker holding the silicon oil is kept on hot plate while the thermocouple connected to the hot plate is used to control the temperature.

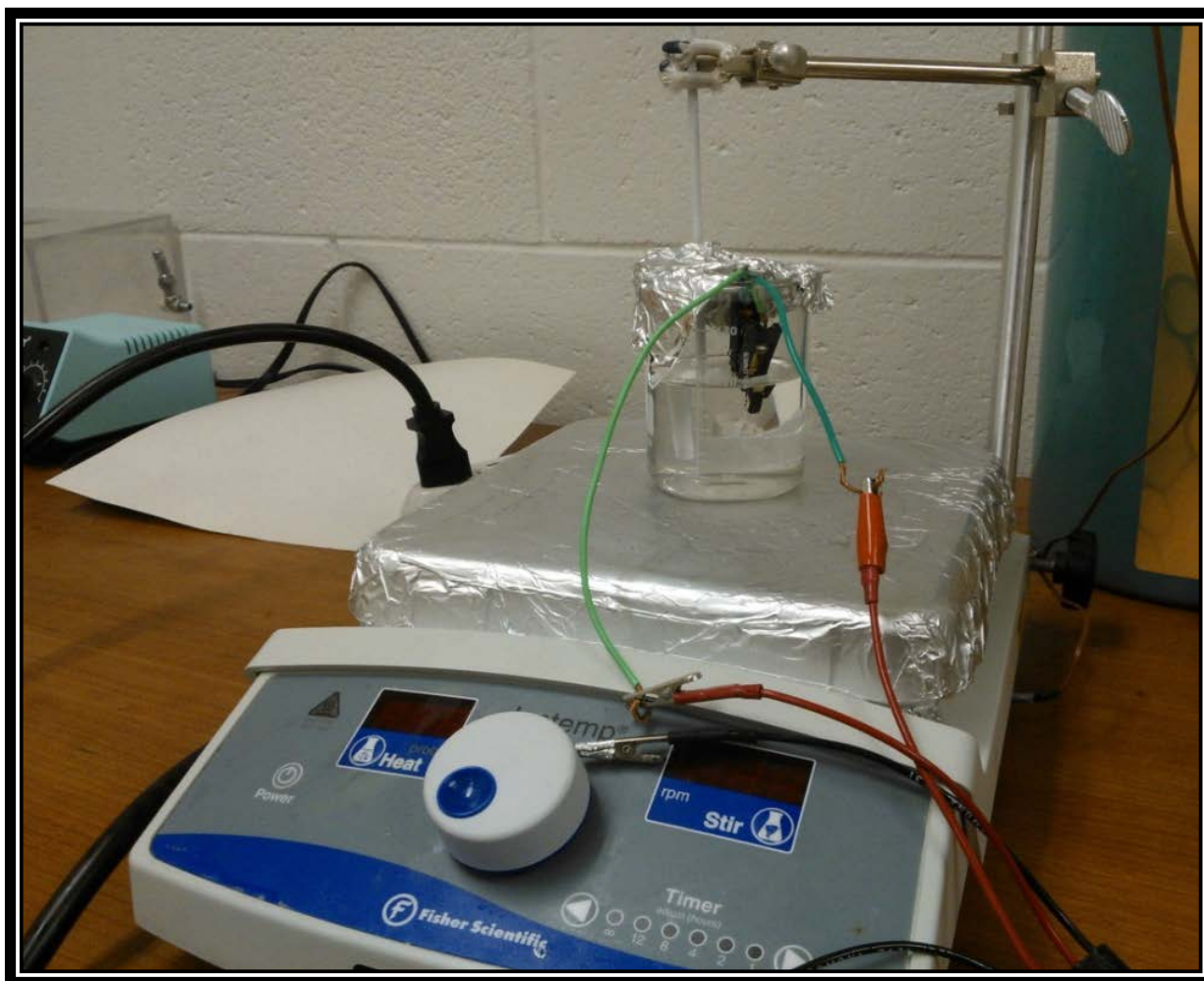


Figure 4.15 Nanocomposite inside silicon oil for electrical testing



## Chapter 5: Results and discussion

### 5.1 ZnO NWS COATED ELECTRODES FOR LIB

The morphology of zinc oxide nanowires grown on carbon cloth are analyzed with scanning electron microscope as shown in figure 5.1. The diameters are 40 to 110 nm and lengths are 1-3.14  $\mu\text{m}$  of the nanowires. Any other residue is not observed in the sample.

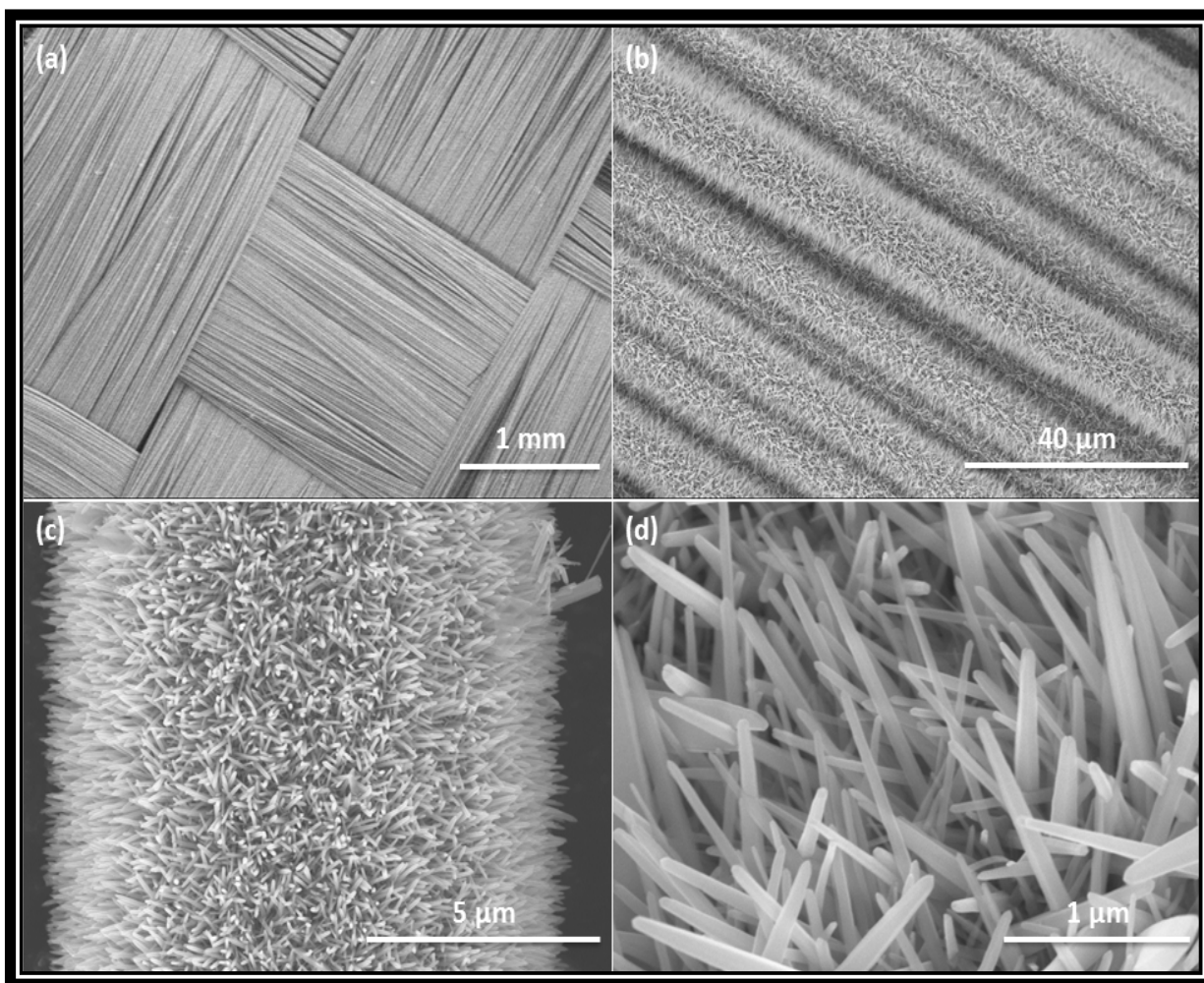


Figure 5.1 SEM images of ZnO nanowires on carbon cloth at different scale (a) 1 mm, (b) 40  $\mu\text{m}$ , (c) 5  $\mu\text{m}$ , (d) 1  $\mu\text{m}$

SEM images of ZnO nanowires grown on graphene are shown in figure 5.2. Good coverage of nanowires is observed on graphene. Residue particles are not seen on the sample. The approximate diameter of the nanowires is 35 to 40 nm.

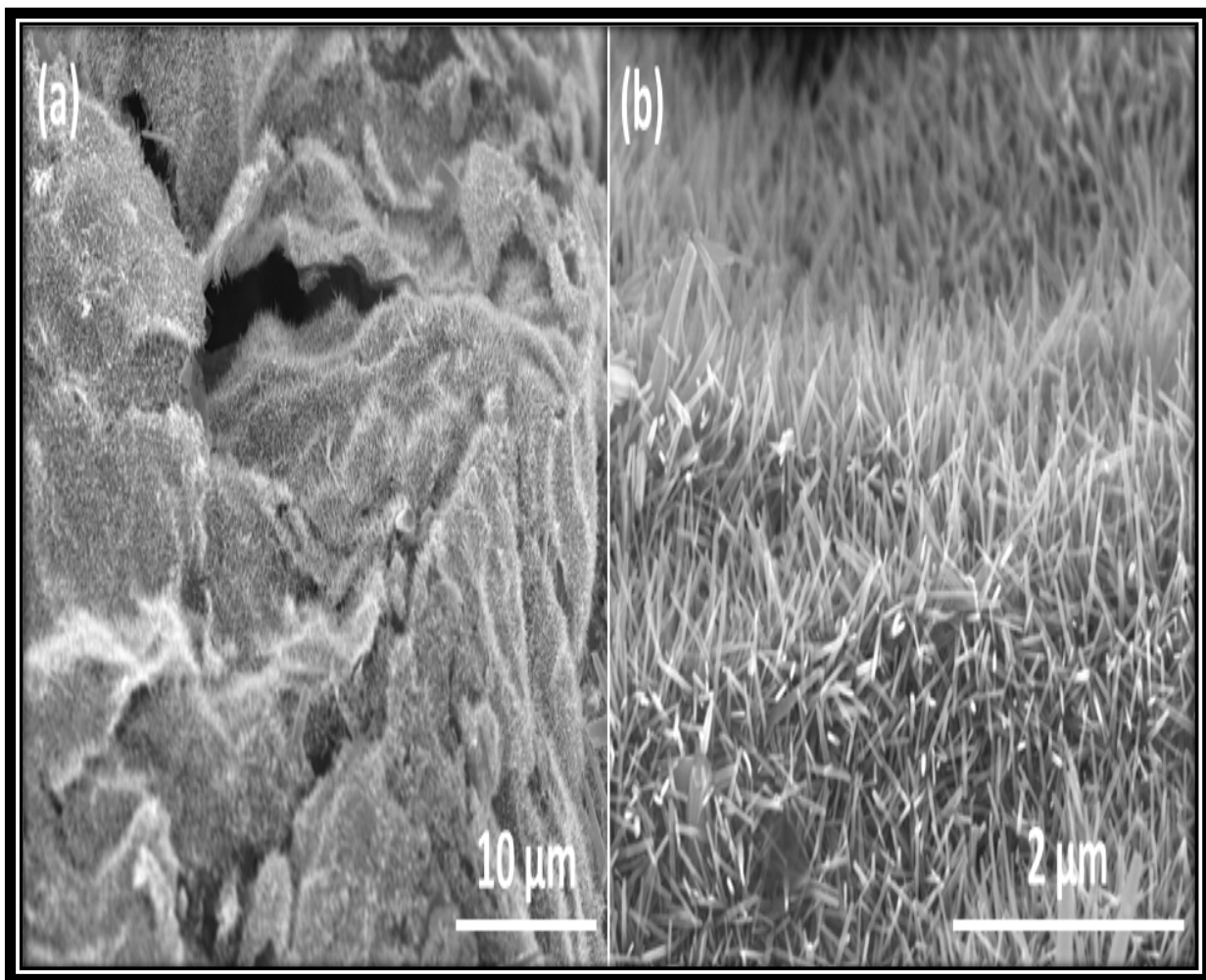


Figure 5.2 SEM images of ZnO nanowires on graphene at different scale (a) 10  $\mu\text{m}$ , (d) 2  $\mu\text{m}$

The electrode is analyzed in SEM after drying overnight. SEM images of prepared electrode are shown in figure 5.3. It is obvious that the nanowires are standing on graphene and increasing the surface area as desired.

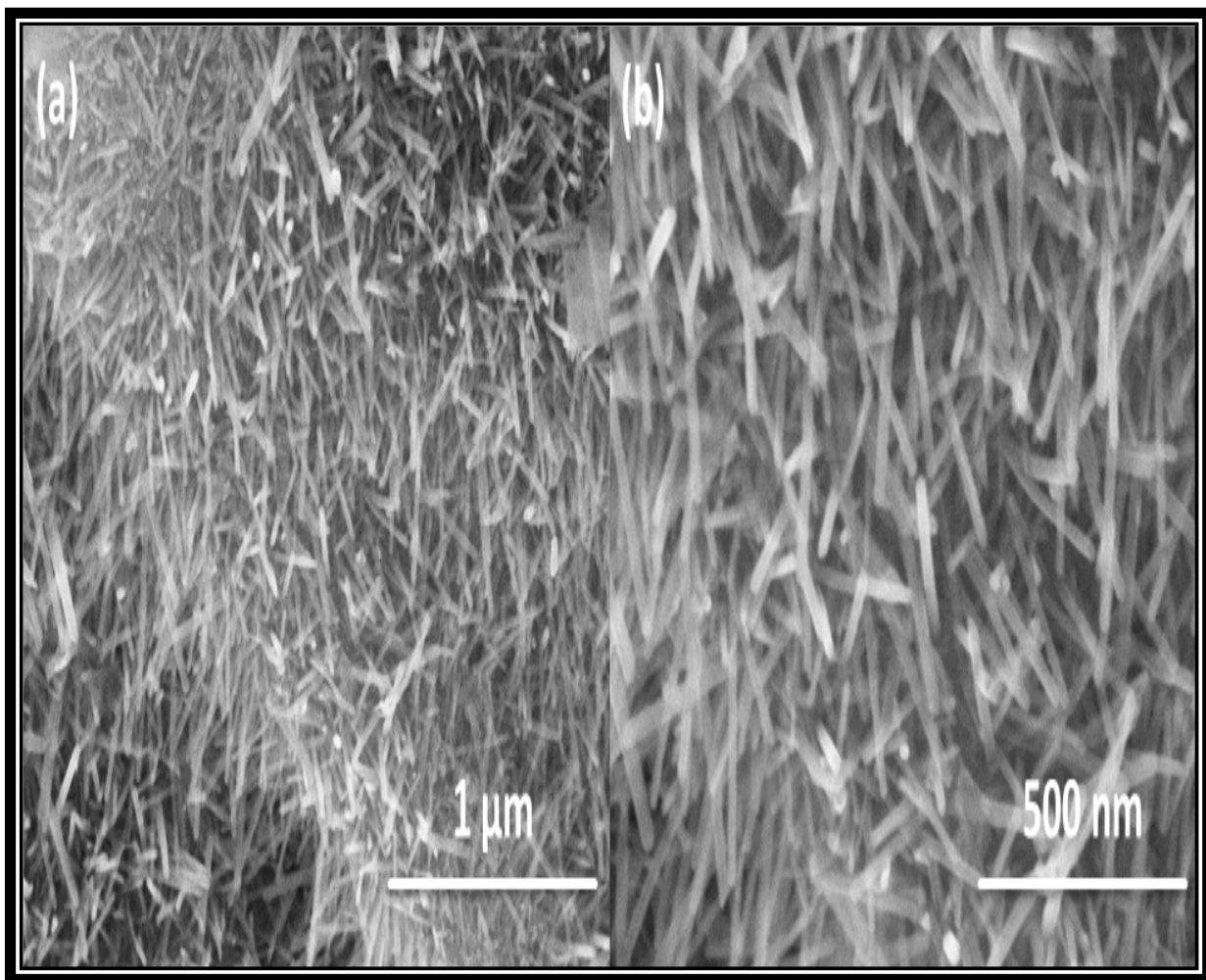


Figure 5.3 SEM images of ZnO NWs/graphene anode surface at different scale (a) 1  $\mu\text{m}$ , (b) 500 nm

The Xrd scan results of the ZnO nanowires on carbon cloth are shown in figure 5.4. The asterisk (\*) mark peak represent carbon of rhombohedral crystal structure. The scan result matches with the standard card JCPDS (01-075-0444) and has lattice parameters of  $a=2.29597$ ,  $b=2.29597$  and  $c=10.15404$ . The rest of the peaks other than the asterisk marked represent zinc oxide which match with the standard card JCPDS (01-070-8070). The lattice parameters for hexagonal zinc oxide are  $a=3.24890$ ,  $b=3.24890$  and  $c=5.20490$ . No other peaks are found which indicates the sample has only zinc oxide and carbon. The sharp peaks with good intensity assure high quality crystals.

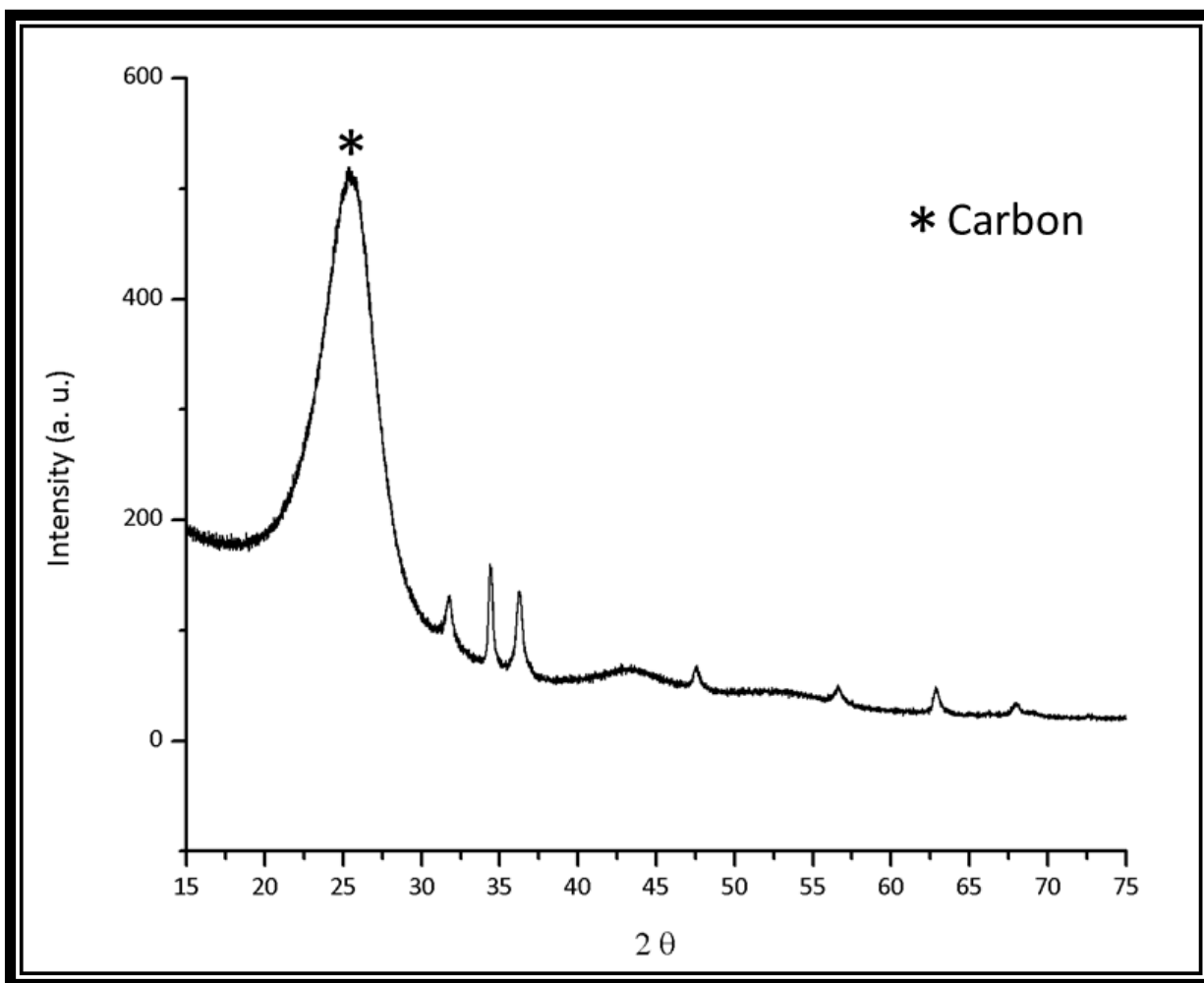


Figure 5.4 Xrd result for ZnO NWs coated carbon cloth. Asterisk (\*) peak is for carbon. The rest of the peaks belong to ZnO

The Xrd scan results of graphene and ZnO NWs/graphene in figure 5.5. The asterisk peak around 26 two theta belongs to graphene as shown in the result. For ZnO/graphene rest of the peaks other than asterisk marked belongs to ZnO which matches to standard card JCPDS (01-070-8070).



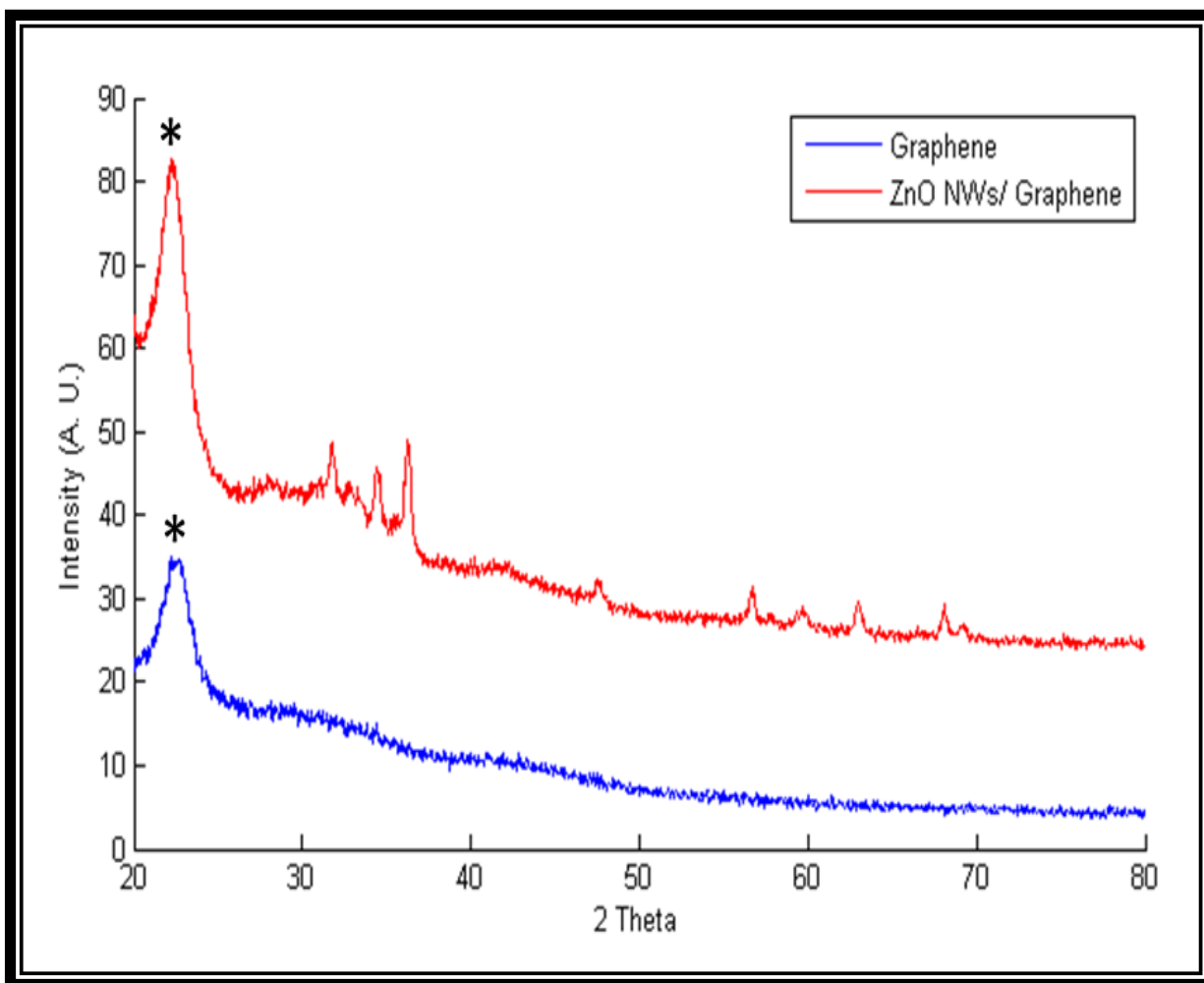


Figure 5.5 Xrd results for graphene and ZnO NWs/graphene. Asterisk (\*) peak is for graphene. The rest of the peaks belong to ZnO

Bare carbon cloth is used as anode against  $\text{LiCoO}_2$  cathode to analyze the specific capacity and cycle performance. Figure 5.6 shows the specific capacity Vs voltage curve found at 100 mA/g current rate in a voltage range of 0.01-3.4 V. The capacity does not very significantly after 20 cycles.

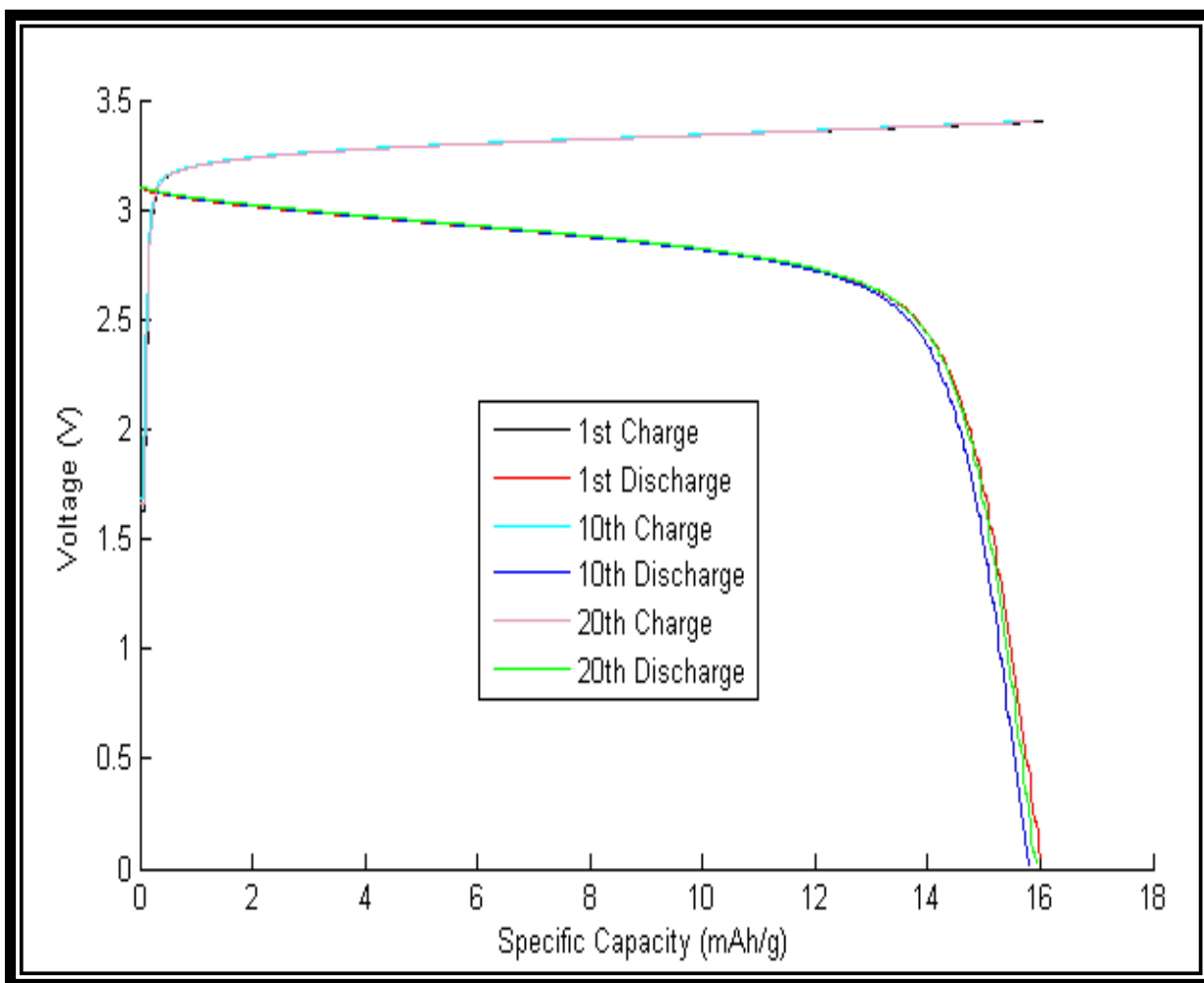


Figure 5.6 Voltage Vs Specific Capacity plot for carbon cloth electrode against LiCoO<sub>2</sub> at 100 mA/g current rate

ZnO NWs coated carbon cloth is also analyzed at the same current rate of 100 mA/g in the voltage range of 0.01-3.5 V against LiCoO<sub>2</sub> cathode and shown in figure 5.7. ZnO NWs/ carbon cloth electrode can be charged in higher voltage window than bare carbon cloth electrode and shows higher specific capacity also. The charge and discharge curves show little decrease in specific capacity after 20 cycles.

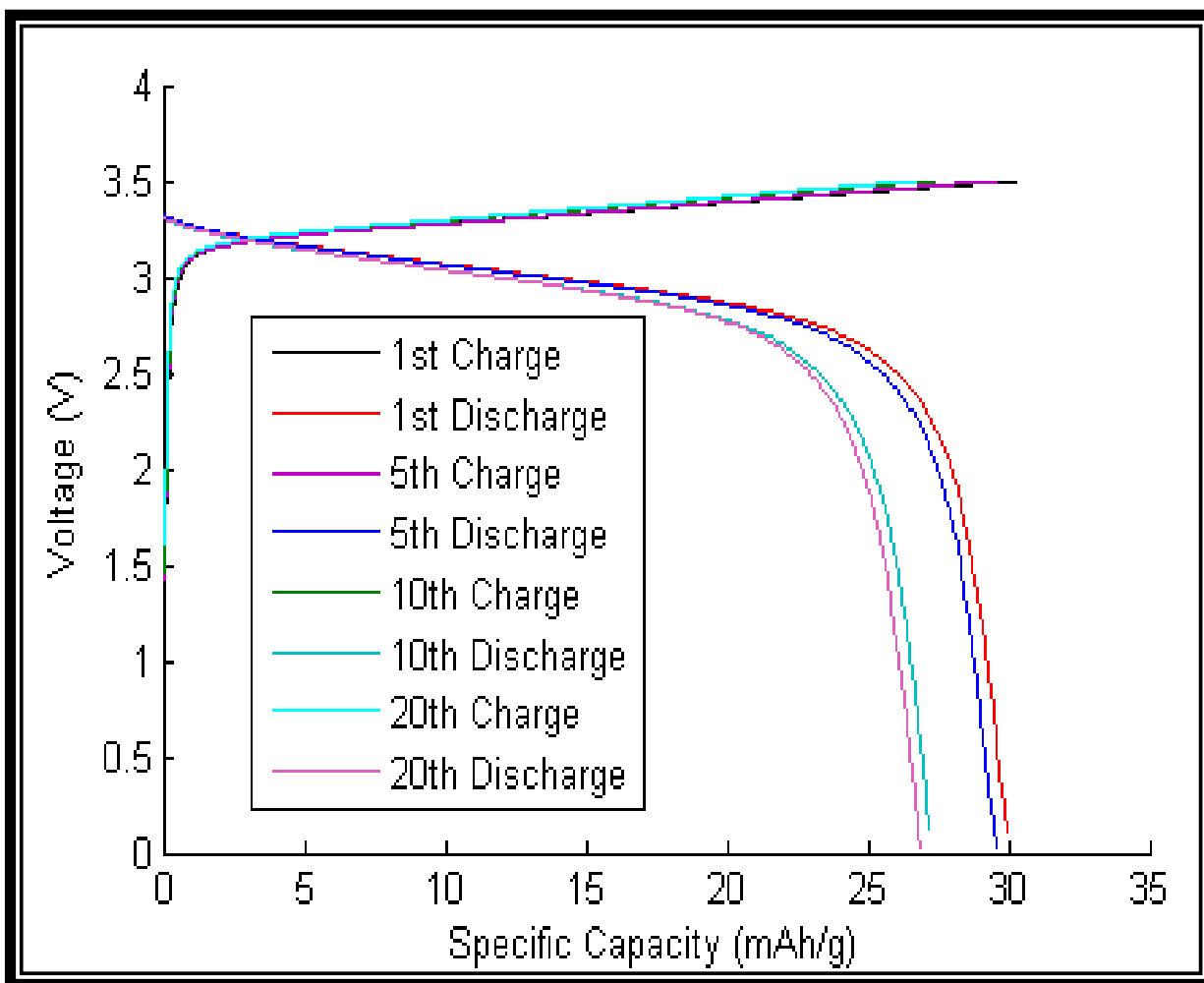


Figure 5.7 Voltage Vs Specific Capacity plot for ZnO NWs/carbon cloth electrode against LiCoO<sub>2</sub> at 100 mA/g current rate

The specific capacities of carbon cloth and ZnO NWs/carbon cloth at charging Vs cycle number are shown in figure 5.8. The figure shows that specific capacities of ZnO NWs/carbon cloth are higher than bare carbon cloth and do not decrease much over operating cycle as expected. The improvement of cyclic performance of carbon cloth for ZnO NWs is very obvious from the results.

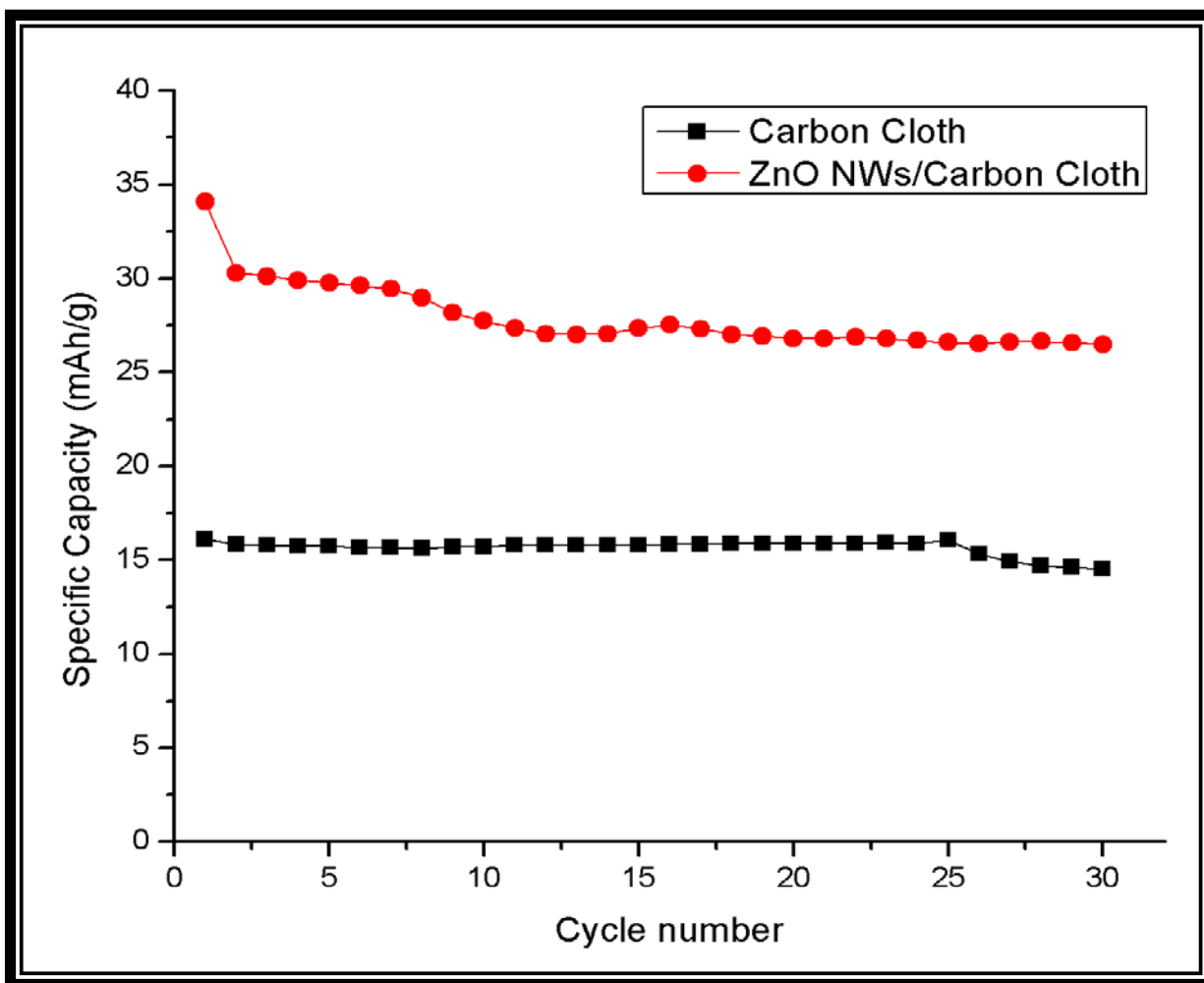


Figure 5.8 Specific Capacity Vs cycle number for carbon cloth and ZnO NWs/ carbon cloth against  $\text{LiCoO}_2$  at charging at 100 mAh/g

The specific capacity of graphene anode is analyzed against  $\text{LiCoO}_2$  cathode at 100 mA/g in voltage window of 0.01-3.7 V and results are shown in figure 5.9. The 1<sup>st</sup> charging cycle shows highest specific capacity of 690 mAh/g but low reversibility because of solid electrolyte interface (SEI). But graphene anode shows good reversibility after 20 operating cycle.

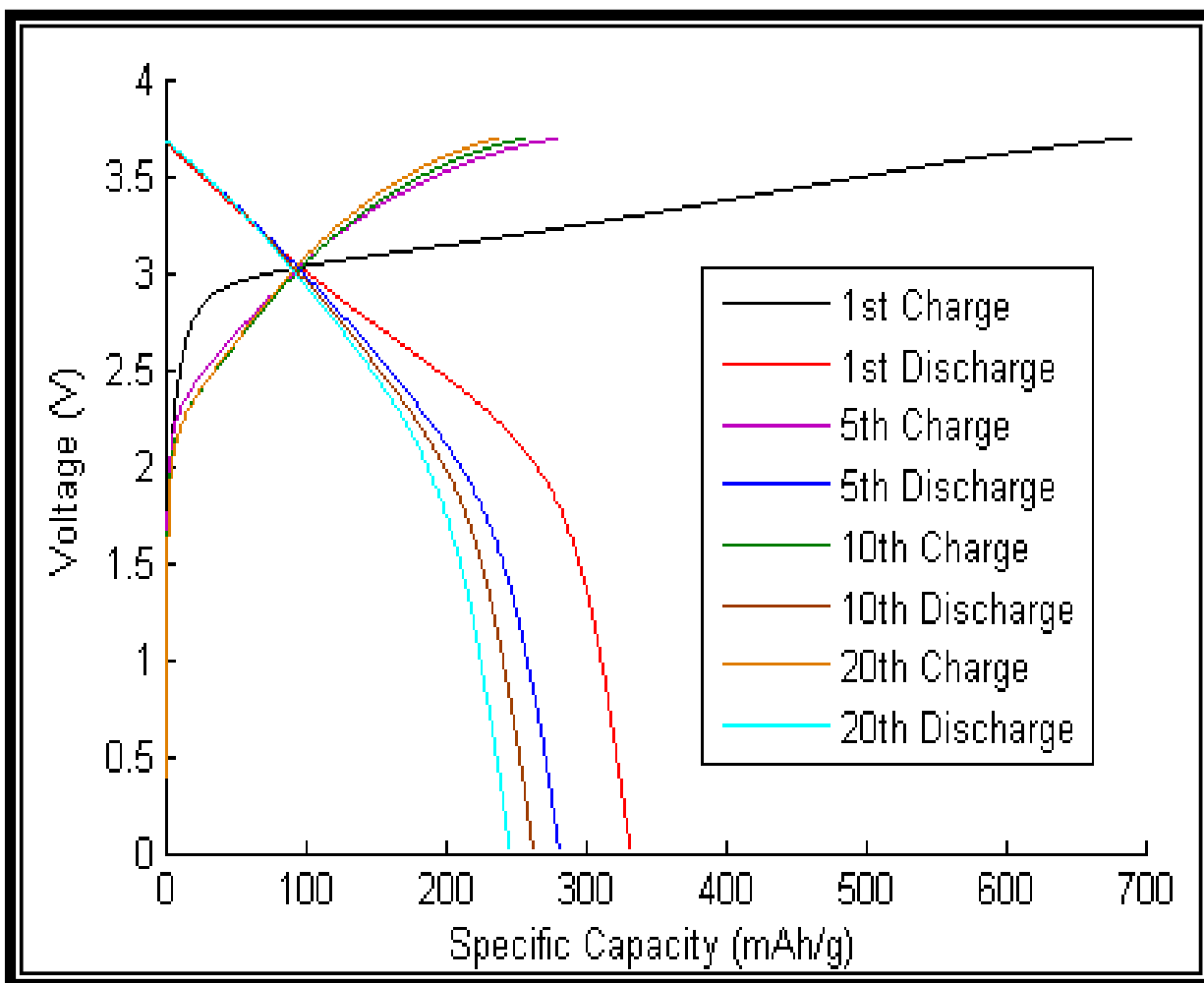


Figure 5.9 Voltage Vs specific capacity of graphene anode against LiCoO<sub>2</sub> cathode at 100 mA/g current rate

ZnO NWs/ graphene anode is also analyzed against LiCoO<sub>2</sub> cathode at 100 mAh/g current rate in 0.01-3.7 voltage range. ZnO NWs/graphene anode shows lower specific capacity in the first charge discharge cycle than graphene anode as shown in figure 5.10. The reason might be the ZnO NWs, they are preventing the graphene layers to form AA stage which decreases the specific capacity. It is observed that the specific capacity of ZnO NWs/graphene anode increases as the operating cycle number increases and highest specific capacity is found 305 mAh/g after 37 cycle.

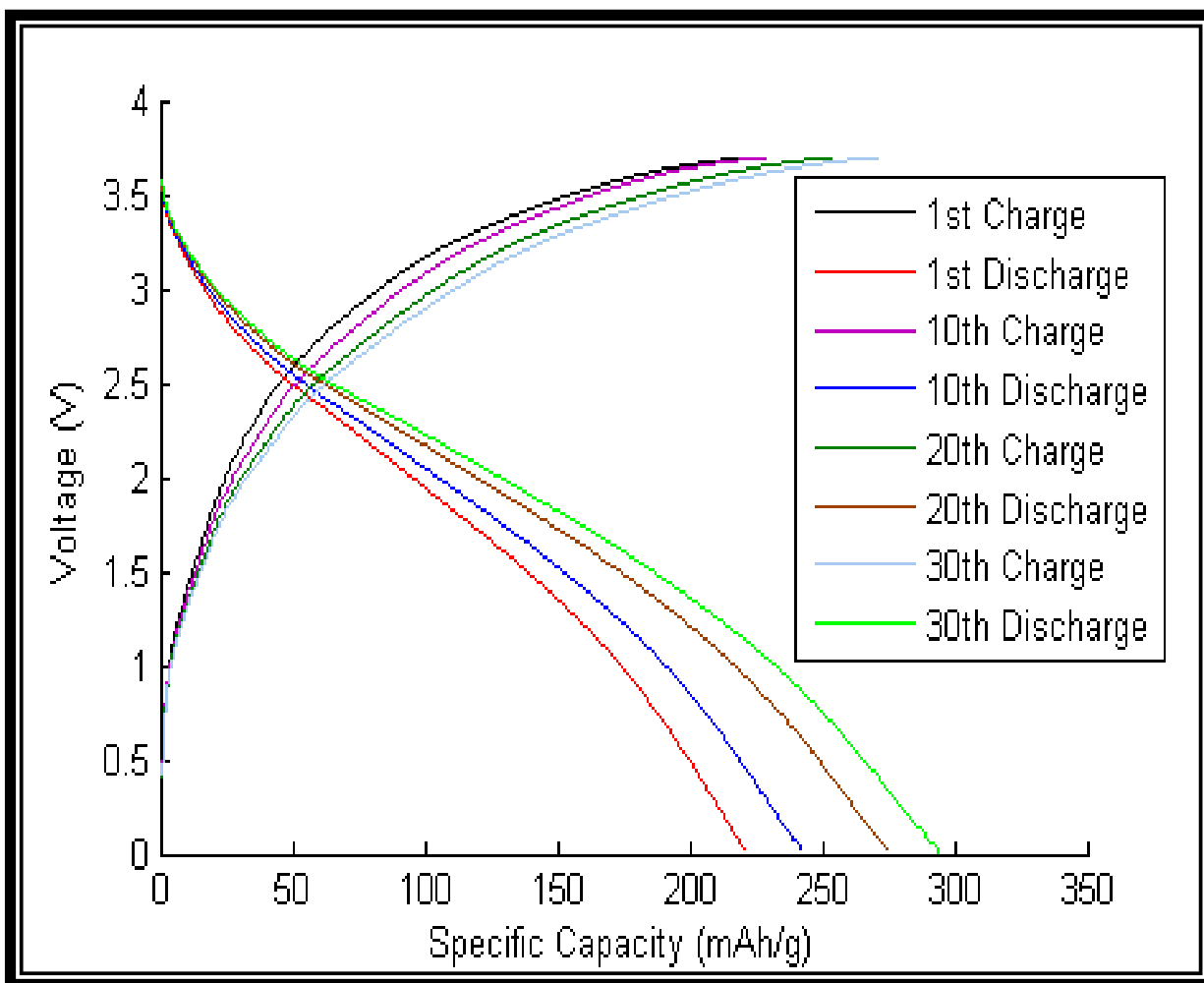


Figure 5.10 Voltage Vs Specific capacity plot for ZnO NWs/graphene anode against LiCoO<sub>2</sub> cathode at 100 mAh/g current rate

The change of specific capacities of graphene anode and ZnO NWs/graphene anode over cycle number are shown in figure 5.11. The specific capacity of graphene decreases as the operating cycle increases which means the decrease in reversibility of graphene. For ZnO NWs/graphene anode, specific capacity decreases in 2<sup>nd</sup> cycle but gradually increases after that with the increase of cycle number. This is due to the ZnO NWs since all the equipment for assembling both the batteries are same and same testing parameter is used. One explanation could be the ZnO NWs which increased the diffusion rate and more Li<sup>+</sup> can diffuse in the graphene as the cycle number increases.

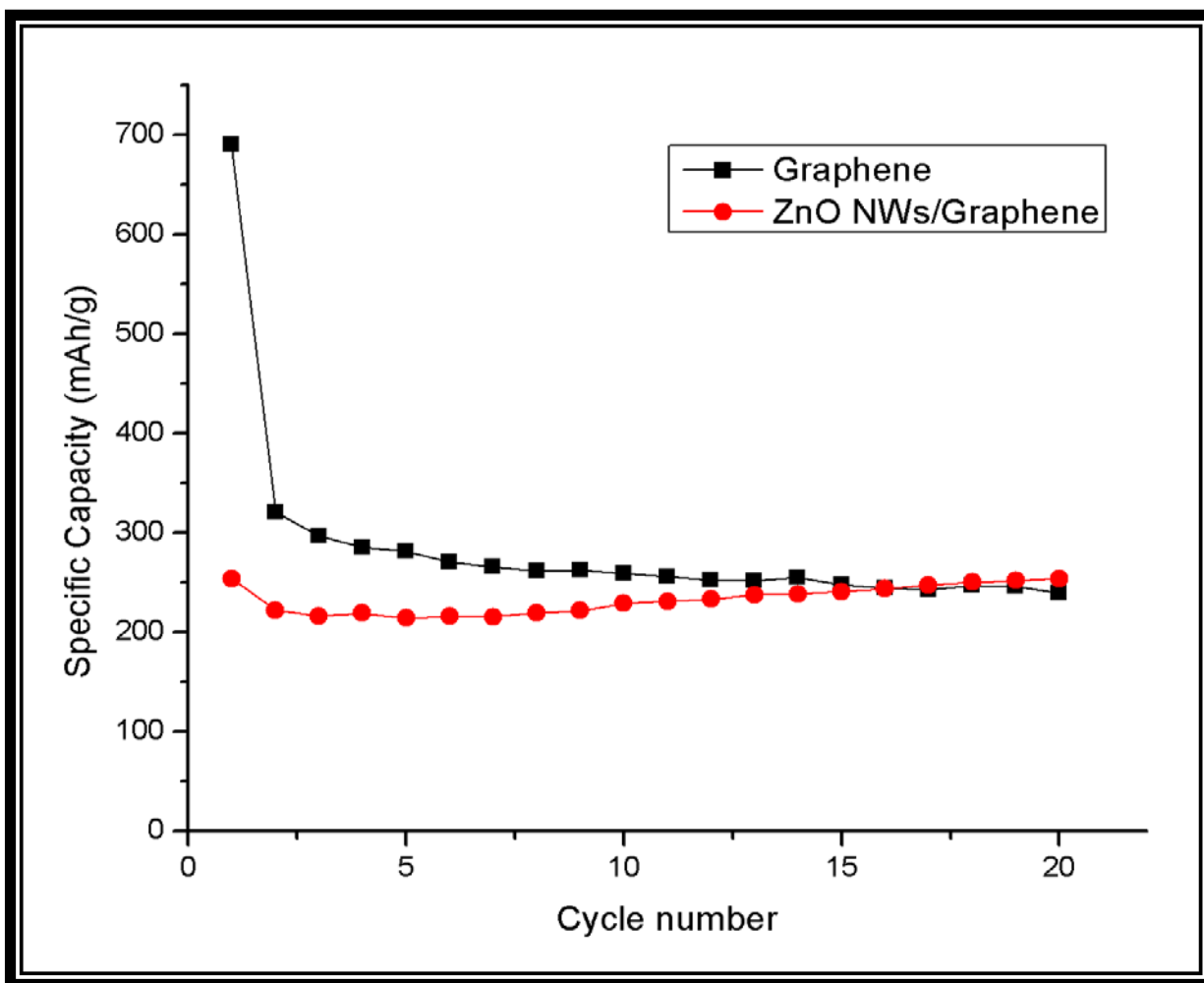


Figure 5.11 Specific capacity Vs cycle number for graphene and ZnO NWs/ graphene anode at 100 mA/g current in 0.01-3.7 V range

## 5.2 PTO-PVDF NANOCOMPOSITES

The morphology of synthesized PTO nanowires both before and after annealing is analyzed by scanning electron microscopy as shown in figure 5.12. The diameter of PTO nanowires is 100 nm and length is 10  $\mu\text{m}$  approximately.

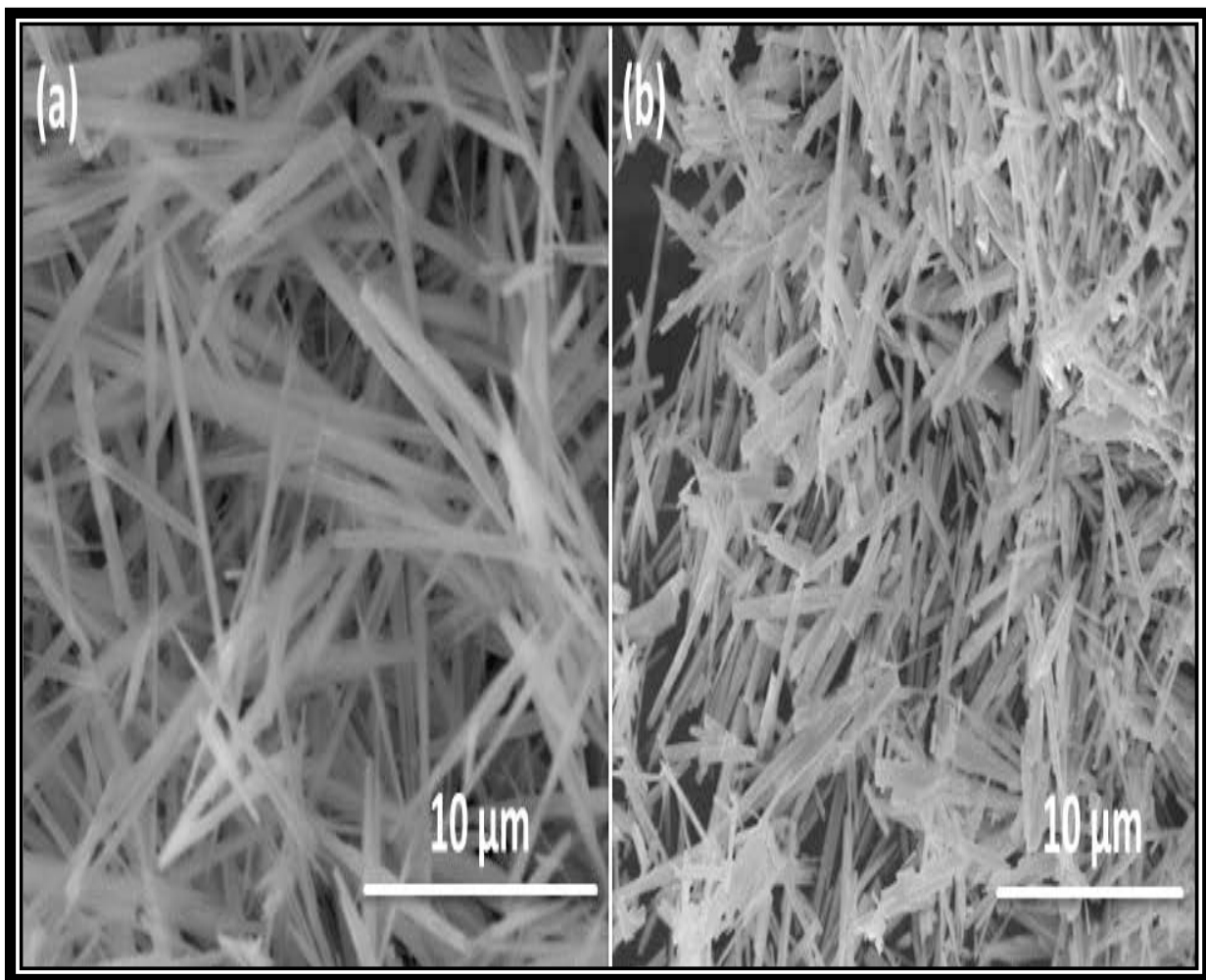


Figure 5.12 SEM images of PTO nanowires (a) Before annealing (b) After annealing at 600 °C for 2 h

The X-ray diffraction patterns of lead titanate nanowires before and after the annealing at 600 °C for 2 hours are shown in figure 5.13. The scan result before annealing shows the lattice parameters of PTO nanowires are  $a=b=12.358 \text{ \AA}$ ,  $c=14.541 \text{ \AA}$  and has tetragonal crystal structure which matches with standard card JCPDS of PTO (No. 00-048-0105). This scan result shows that pure perovskite phase is absent which indicates the significance of annealing. The XRD scan has been done on PTO nanowires after annealing at 600 °C for 2 hours. There are significant changes in peaks before and after the annealing. The increased intensity of the scan result after the annealing indicates improvement of crystallinity. After the annealing XRD scan shows that PTO nanowires has tetragonal structure and lattice parameters are  $a = b = 3.9024 \text{ \AA}$  and  $c = 4.1583 \text{ \AA}$  which matches with standard card JCPDS of PTO (No. 01-074-3218) as found in previous work [84, 153].



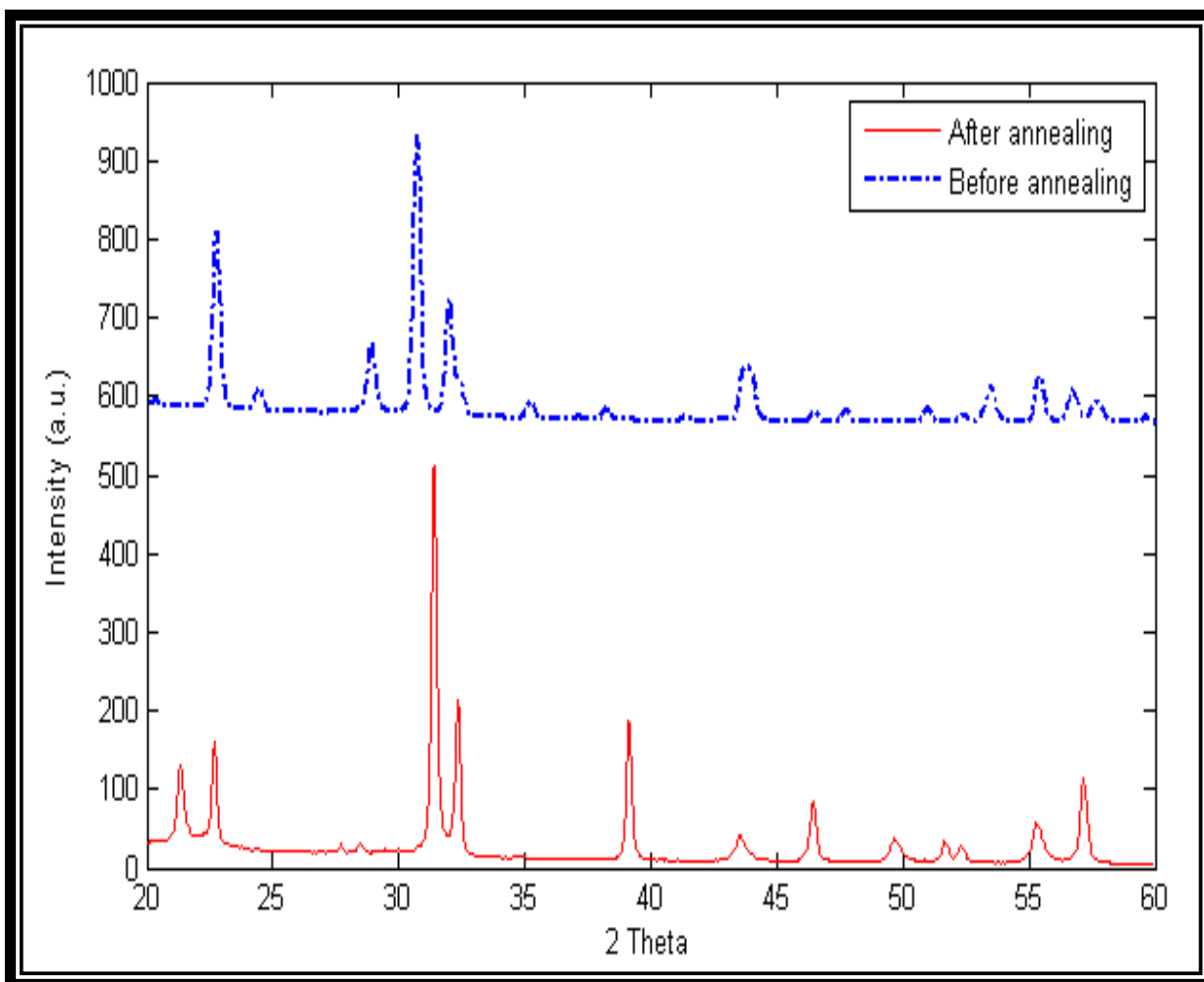


Figure 5.13 XRD pattern of PTO nanowires before and after annealing at 600 °C for 2 hours

The SEM images of PTO-PVDF nanocomposites are shown in figure 5.14. The volume fractions of PTO nanowires in PVDF are 5, 10, 20 and 30 % . The figure shows the random dispersion of PTO nanowires in the PVDF matrix and nanocomposites are free of voids. The amount of nanowires is increased as the volume fraction increases in the same magnification of SEM images.

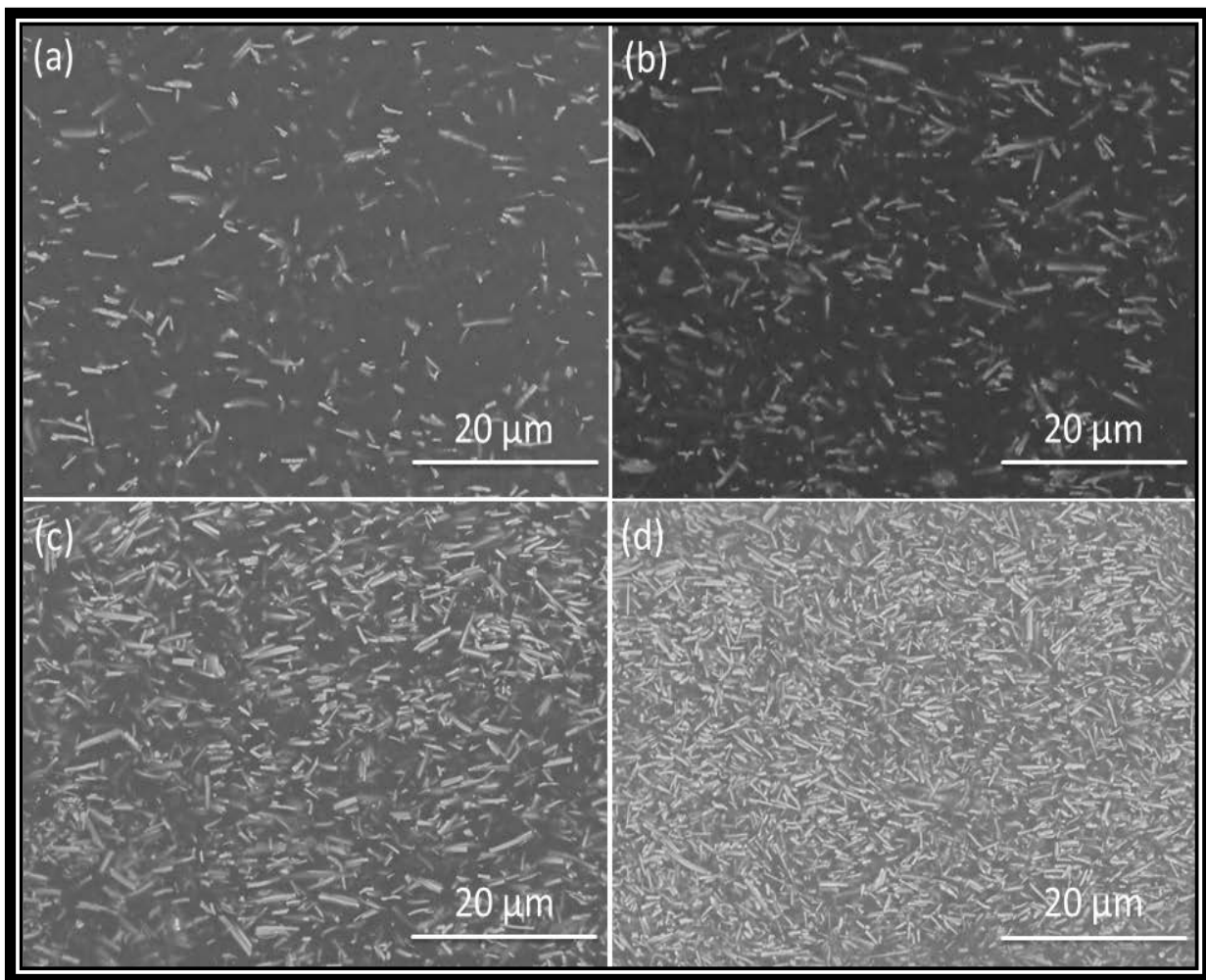


Figure 5.14 SEM images of PTO-PVDF nanocomposites of different volume fraction of PTO nanowires (a) 5 %, (b) 10 %, (c) 20 % and (d) 30 %

The dielectric permittivity is different for each volume fraction of nanocomposites. At least five different samples are made for each volume fraction and average has been taken into account. In order to measure dielectric constant the following equation is used,

dependency of dielectric permittivity. The tests to measure dielectric constants of different volume fractions are performed at room temperature (21.67 °C), 40 °C, 60 °C and 80 °C.

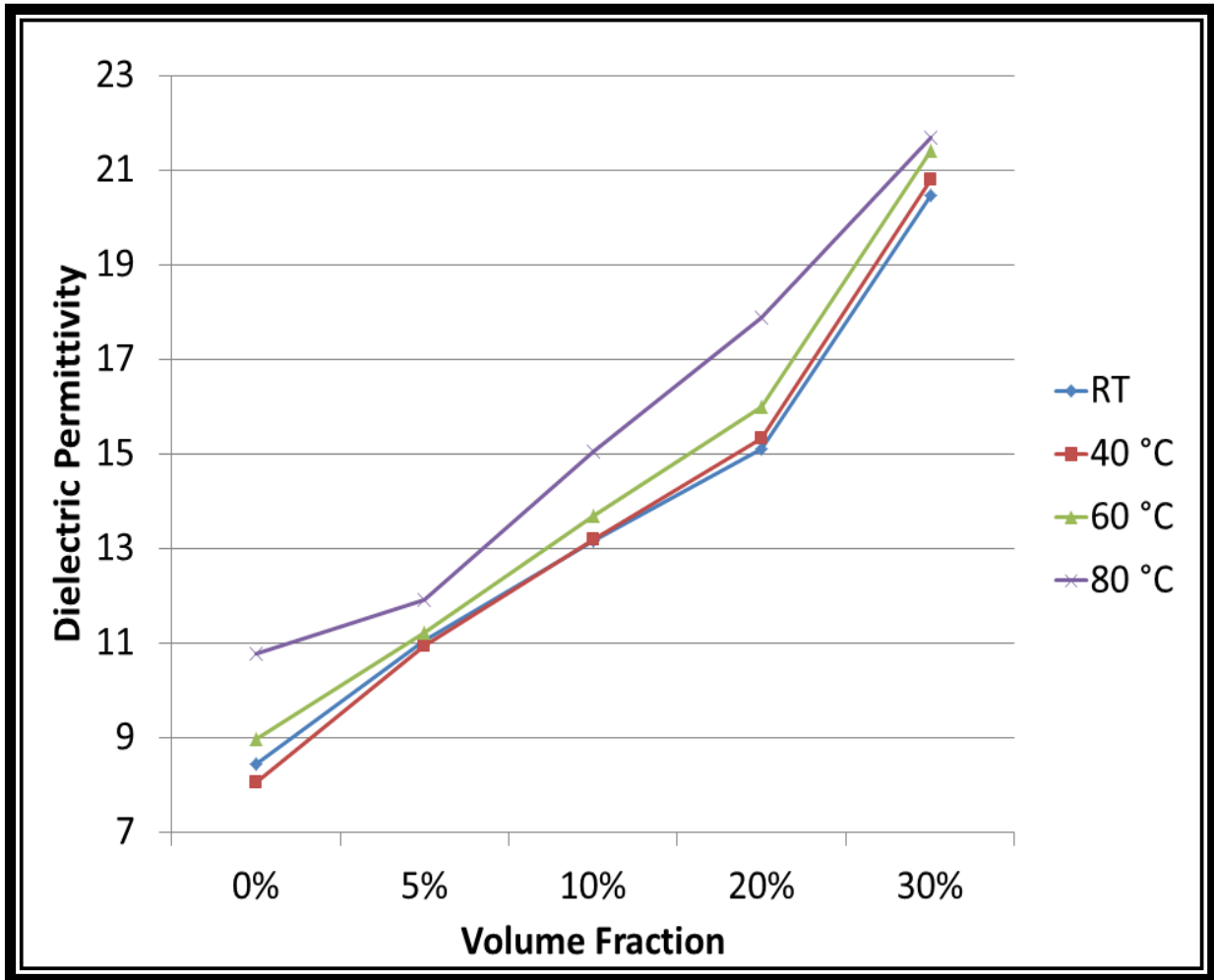


Figure 5.15 Dielectric permittivity at 1 kHz of nanocomposites at different temperature as a function of PTO NWs volume fractions

The dielectric constant increases as the volume fraction increases because dielectric constants of PTO NWs is about two orders of magnitude higher than that of PVDF matrix [154]. Here 0 % volume fraction is the pure PVDF without any NWs inclusion. The dielectric constant increases with increase of temperature also. The dielectric constant of bulk PTO is 180 at 1 kHz [120] but for nanocomposites the highest dielectric constant obtained is 21.67 for 30 % volume fraction at 80 °C.

The dielectric constants of nanocomposites are measured for 100 Hz to 1 MHz frequency which is shown in figure 5.16. Dielectric permittivity decreases with increase of frequency and for 100 Hz to 1

kHz, the decrease is sharp but not for 1 kHz to 1 MHz frequency. All this results are obtained at room temperature.

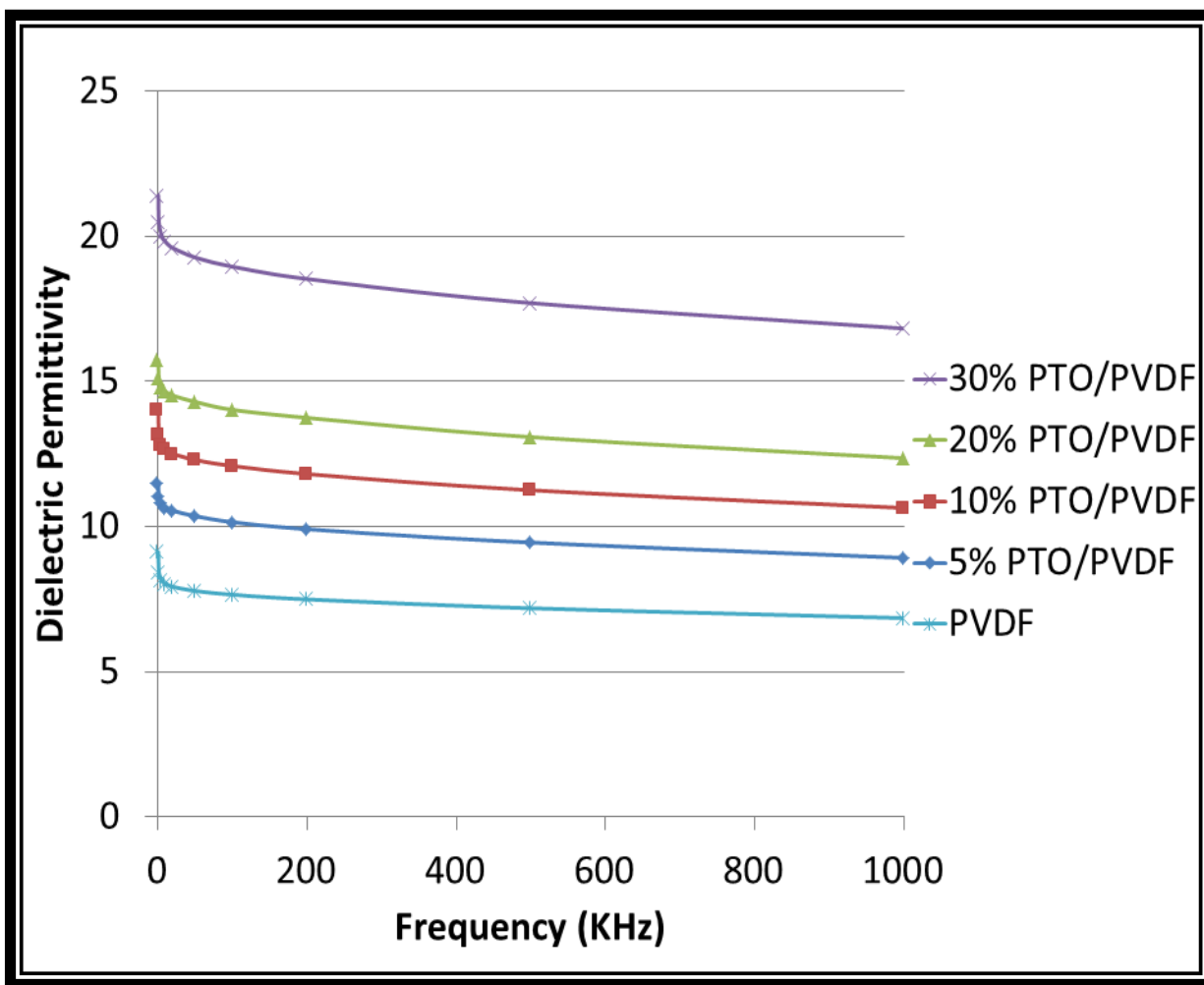


Figure 5.16 Dielectric permittivity of nanocomposites for different frequency at room temperature

Dielectric losses of nanocomposites of different volume fractions at various temperatures are shown in figure 5.17. All these results are obtained at 1 kHz frequency. Dielectric loss tangents are decreased as the volume fraction increased at room temperature, 40 °C, 60 °C as expect but shows different trend at 80 °C. It might be because of high temperature the PVDF matrix gets soft and loses its electrical properties. It has been observed that the dielectric constants and dielectric loss tangents show consistent results at less than 60 °C.

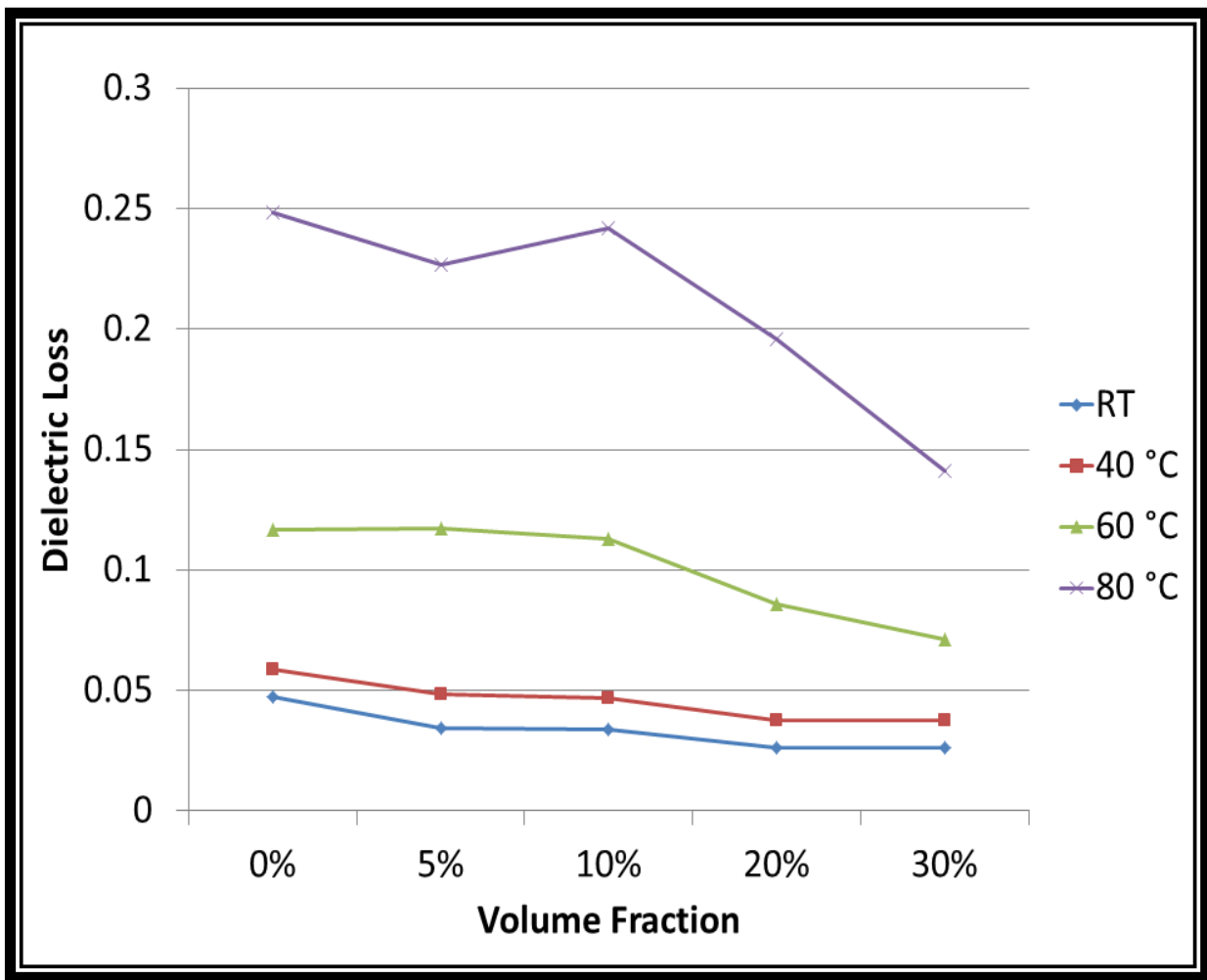


Figure 5.17 Dielectric loss tangent of different volume fraction nanocomposites at different temperature

Breakdown strengths of nanocomposites of various volume fractions at different temperatures are shown graphically in figure 5.18. Breakdown strength is breakdown voltage divided by thickness of the sample. The maximum voltage that the sample can withstand until it becomes conductive is called the breakdown voltage. From this curve, it is observed that pure PVDF composite has the highest breakdown strength of 299.7421 MV/m at room temperature. As the volume fraction of PTO NWs increases the breakdown strength decreases because the NWs create channel for current to flow through the sample. Also at higher temperature the breakdown strengths get lower because of the thermal energy which assists the current flow.

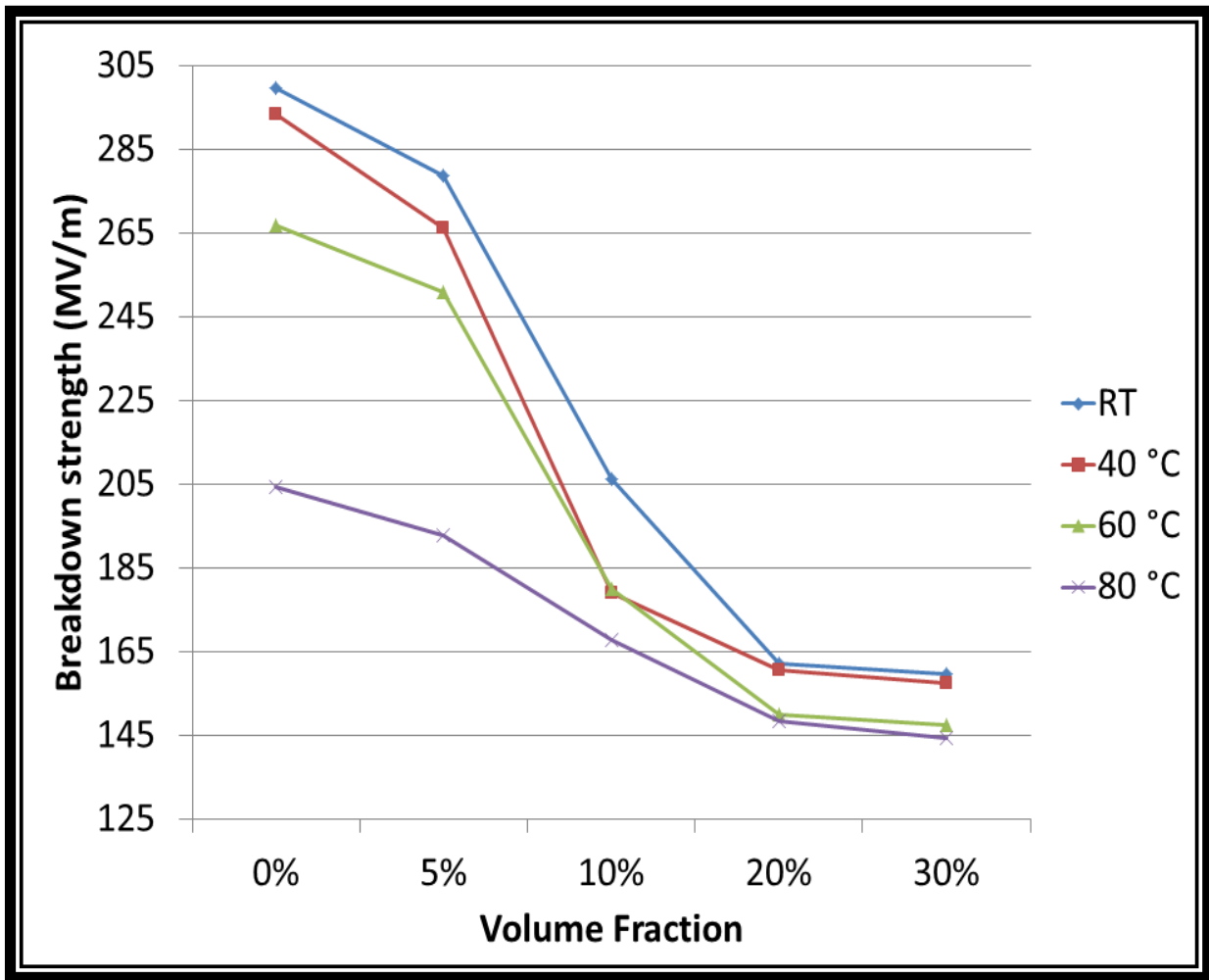


Figure 5.18 Breakdown strengths of nanocomposites at various temperatures

Energy densities of nanocomposites of various volume fractions at different temperatures are shown in figure 5.19. Energy density is a function of dielectric permittivity and breakdown strength. The dielectric constants of nanocomposites at 1 kHz is considered to calculate energy densities. Even though pure PVDF matrix shows highest breakdown strength has low energy density than 5 % volume fraction PTO-PVDF nanocomposites. As the energy densities for 10 and 20 % volume fraction get lower because of the lower breakdown strengths and gets higher for 30 % volume fraction even though lowest breakdown strength is found for 30 % volume fraction sample. Highest energy density is found for 5 % volume fraction PTO-PVDF sample at room temperature which is 3.80 J/cc. It is observed that energy density is decreased as the temperature of the nanocomposites increased. That's because breakdown

strength has second order in the energy equation but dielectric constant has one order. For this reason energy density is lower at higher temperature.

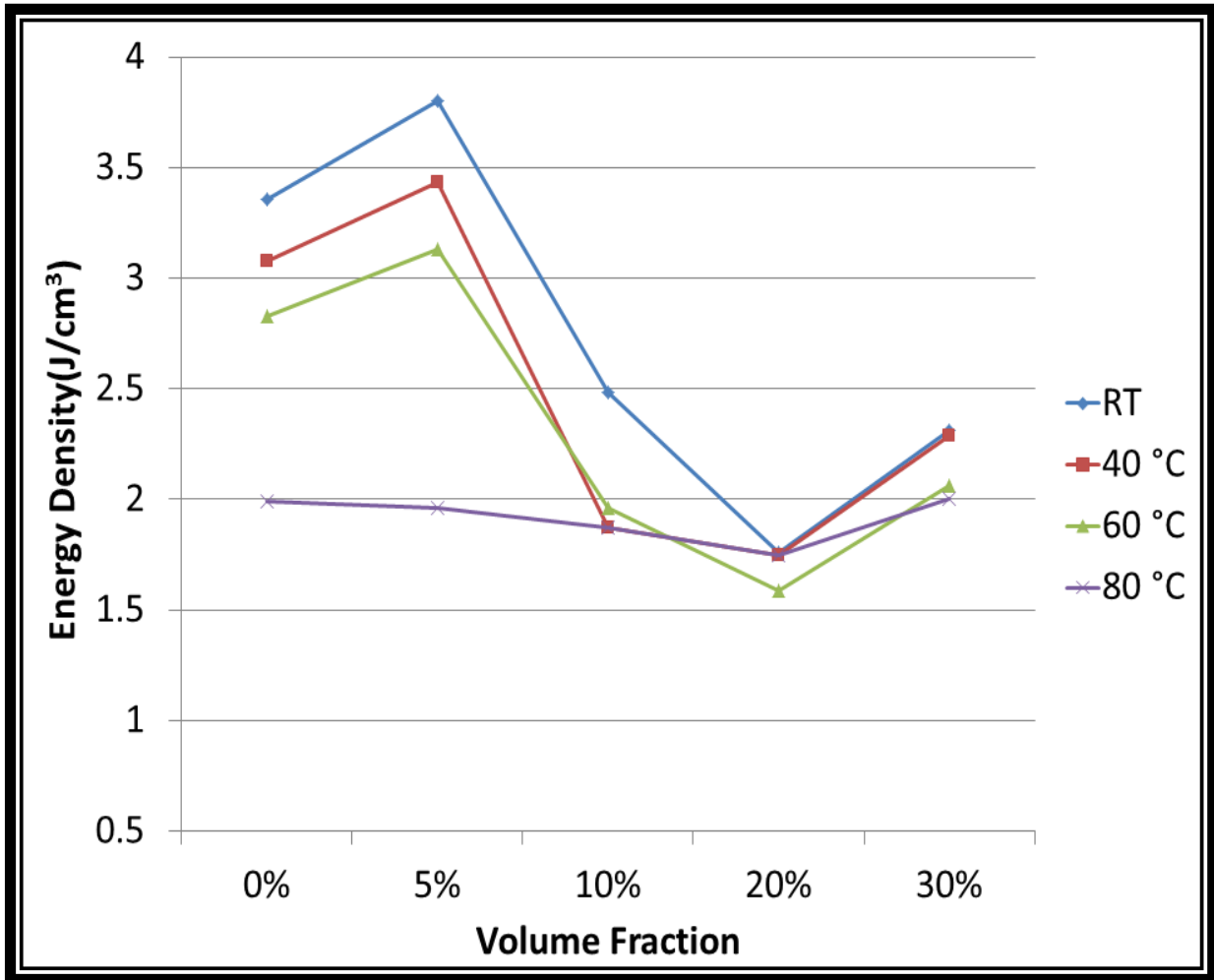


Figure 5.19 Energy density of nanocomposites at different temperatures at 1 kHz frequency

Specific energy of nanocomposites at 1 kHz frequency is shown in figure 5.20. The results are obtained at room temperature. The highest specific energy of 1.84 J/g is obtained for 5 % volume fraction of PTO nanocomposites. The specific energy of nanocomposites decrease with the increase of volume fraction of PTO nanowires but start increasing at 30 % volume fraction nanocomposites. The specific energies at higher temperatures are not shown because the maximum energy is found at room temperature.

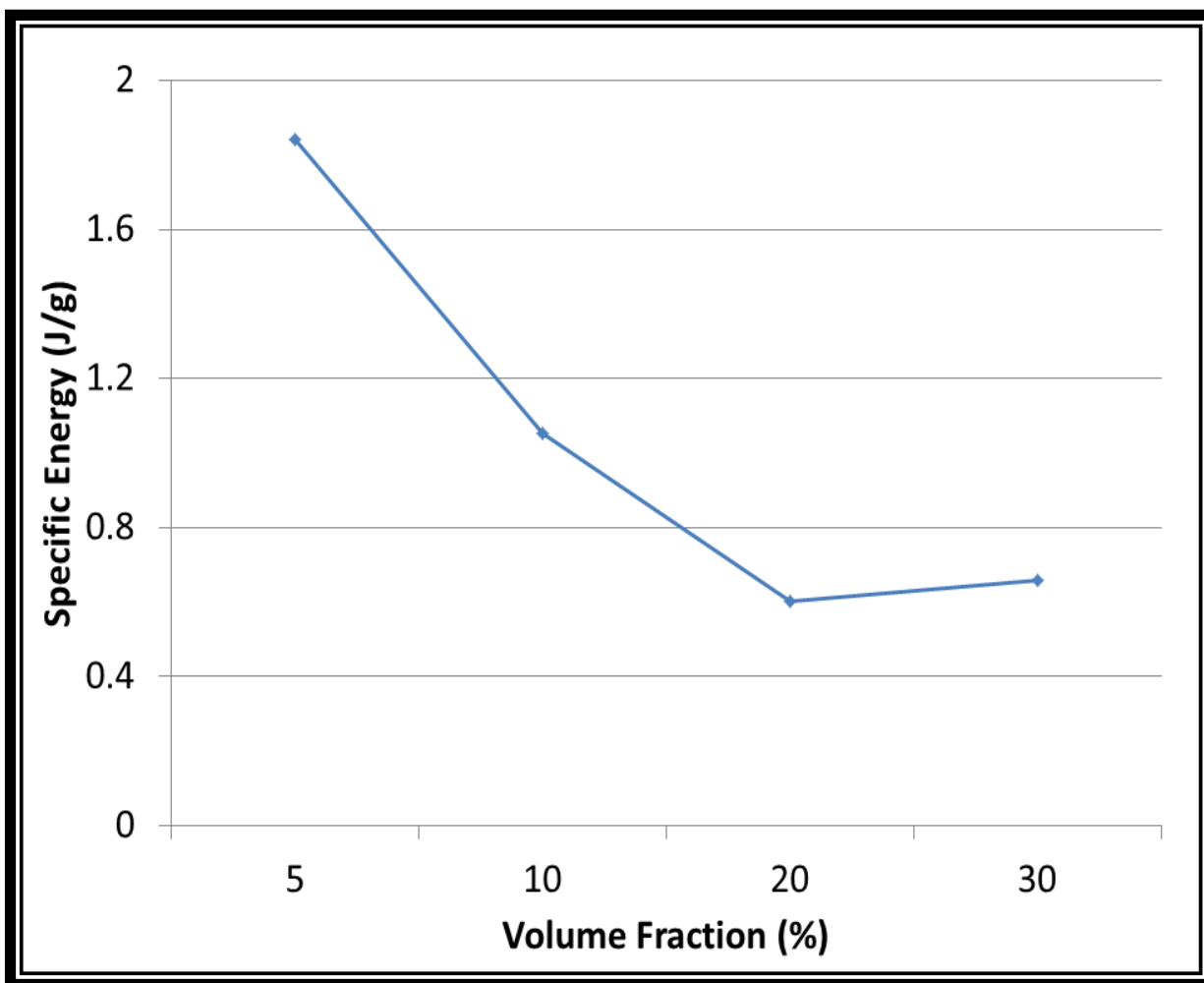


Figure 5.20 Specific energy of nanocomposites of different volume fractions at 1 kHz at room temperature



## Chapter 6: Conclusion

Zinc oxide nanowires have improved the performance of carbon cloth anode and graphene anode of lithium ion battery. The specific capacity of LIB has increased for the zinc oxide nanowire coated anode than anodes without nanowires. The cyclic performances of zinc oxide nanowire coated carbon cloth and graphene are also better than bare carbon cloth and graphene. The specific capacity of graphene anode decreases as the operation cycle increase but reverse happens for zinc oxide nanowire coated graphene.

Energy densities of PTO NWs/PVDF dielectric capacitor at different temperature has determined. The energy densities decrease as the o

## References

1. Long, J.W., et al., *Three-dimensional battery architectures*. Chem Rev, 2004. 104(10): p. 4463-92.
2. Tarascon, J.M. and M. Armand, *Issues and challenges facing rechargeable lithium batteries*. Nature, 2001. 414(6861): p. 359-67.
3. Whittingham, M.S., *Electrical energy storage and intercalation chemistry*. Science (New York, N.Y.), 1976. 192(4244): p. 1126-1127.
4. Rao, B.M.L., R.W. Francis, and H.A. Christopher, *Lithium-Aluminum Electrode*. Journal of The Electrochemical Society, 1977. 124(10): p. 1490-1492.
5. Broadhead, J.N.-A.B.U.U.S.P.N., 864,167. 1975., Broadhead, John. "NON-AQUEOUS BATTERY USING." U.S. Patent No. 3,864,167. 1975. 1975.
6. Mizushima, K., et al., *LixCoO2 (0<x<-1): A new cathode material for batteries of high energy density*. Materials Research Bulletin, 1980. 15(6): p. 783-789.
7. Thackeray, M.M., et al., *Lithium insertion into manganese spinels*. Materials Research Bulletin, 1983. 18(4): p. 461-472.
8. Murphy, D.W., et al., *Topochemical reactions of rutile related structures with lithium*. Materials Research Bulletin, 1978. 13(12): p. 1395-1402.
9. Lazzari, M. and B. Scrosati, *A Cyclable Lithium Organic Electrolyte Cell Based on Two Intercalation Electrodes*. Journal of The Electrochemical Society, 1980. 127(3): p. 773-774.
10. Nagaura, T.T., K., *Lithium ion rechargeable battery*. Prog. Batteries Solar Cells. 1990. 9: p. 209.
11. Arora, P., R.E. White, and M. Doyle, *Capacity Fade Mechanisms and Side Reactions in Lithium-Ion Batteries*. Journal of The Electrochemical Society, 1998. 145(10): p. 3647-3667.
12. Whittingham, M.S., *Lithium batteries and cathode materials*. Chemical Reviews-Columbus, 2004. 104(10): p. 4271-4302.
13. Ceder, G., et al., *Thermodynamics of oxides with substitutional disorder: a microscopic model and evaluation of important energy contributions*. Journal of the American Ceramic Society, 2005. 81(3): p. 517-525.

14. Koksang, R., et al., *Cathode materials for lithium rocking chair batteries*. Solid state ionics, 1996. 84(1): p. 1-21.
15. Megahed, S. and B. Scrosati, *Lithium-ion rechargeable batteries*. Journal of Power Sources, 1994. 51(1): p. 79-104.
16. Wilk, G.D., R.M. Wallace, and J. Anthony, *High- $\kappa$  gate dielectrics: Current status and materials properties considerations*. Journal of Applied Physics, 2001. 89(10): p. 5243-5275.
17. Winter, M. and R.J. Brodd, *What Are Batteries, Fuel Cells, and Supercapacitors?* Chem Rev, 2004. 104(10): p. 4245-4270.
18. Guyomard, D., T. Osaka, and M. Datta, *New Trends in Electrochemical Technology: Energy Storage Systems in Electronics*. Gordon & Breach Science Publishers, 2000. 9: p. 253-350.
19. Cho, J., et al., *A breakthrough in the safety of lithium secondary batteries by coating the cathode material with  $\text{AlPO}_4$  nanoparticles*. Angewandte Chemie International Edition, 2003. 42(14): p. 1618-1621.
20. Scrosati, B., *Recent advances in lithium ion battery materials*. Electrochimica Acta, 2000. 45(15): p. 2461-2466.
21. Osaka, T. and M. Datta, *Energy Storage Systems in Electronics*. Vol. 1. 2000: CRC.
22. Im, D. and A. Manthiram, *Lithium manganese oxide–conductive carbon nanocomposite cathodes for rechargeable lithium batteries*. Solid state ionics, 2003. 159(3): p. 249-255.
23. Ohzuku, T. and R.J. Brodd, *An overview of positive-electrode materials for advanced lithium-ion batteries*. Journal of Power Sources, 2007. 174(2): p. 449-456.
24. Ritchie, A., et al., *Future cathode materials for lithium rechargeable batteries*. Journal of Power Sources, 1999. 80(1): p. 98-102.
25. Park, S.B., et al., *An alternative method to improve the electrochemical performance of a lithium secondary battery with  $\text{LiMn}_{2}\text{O}_4$* . Journal of Power Sources, 2007. 166(1): p. 219-225.
26. Aurbach, D., et al., *Design of electrolyte solutions for Li and Li-ion batteries: a review*. Electrochimica Acta, 2004. 50(2): p. 247-254.

27. Ye, H., et al., *Li ion conducting polymer gel electrolytes based on ionic liquid/PVDF-HFP blends*. Journal of The Electrochemical Society, 2007. 154(11): p. A1048-A1057.
28. Aurbach, D., et al., *A short review of failure mechanisms of lithium metal and lithiated graphite anodes in liquid electrolyte solutions*. Solid state ionics, 2002. 148(3): p. 405-416.
29. Soo, P.P., et al., *Rubbery Block Copolymer Electrolytes for Solid-State Rechargeable Lithium Batteries*. Journal of The Electrochemical Society, 1999. 146(1): p. 32-37.
30. Blazejczyk, A., et al., *Novel solid polymer electrolytes with single lithium-ion transport*. Journal of The Electrochemical Society, 2004. 151(10): p. A1762-A1766.
31. Jeon, J.D., B.W. Cho, and S.Y. Kwak, *Solvent-free polymer electrolytes based on thermally annealed porous P (VdF-HFP)/P (EO-EC) membranes*. Journal of Power Sources, 2005. 143(1): p. 219-226.
32. Song, J., Y. Wang, and C. Wan, *Review of gel-type polymer electrolytes for lithium-ion batteries*. Journal of Power Sources, 1999. 77(2): p. 183-197.
33. Kanno, R., et al., *Carbon as negative electrodes in lithium secondary cells*. Journal of Power Sources, 1989. 26(3): p. 535-543.
34. Mohri, M., et al., *Rechargeable lithium battery based on pyrolytic carbon as a negative electrode*. Journal of Power Sources, 1989. 26(3): p. 545-551.
35. Winter, M., et al., *Insertion electrode materials for rechargeable lithium batteries*. Advanced Materials, 1999. 10(10): p. 725-763.
36. Billaud, D., E. McRae, and A. Hérold, *Synthesis and electrical resistivity of lithium-pyrographite intercalation compounds (stages I, II and III)*. Materials Research Bulletin, 1979. 14(7): p. 857-864.
37. Song, X.Y., K. Kinoshita, and T.D. Tran, *Microstructural Characterization of Lithiated Graphite*. Journal of The Electrochemical Society, 1996. 143(6): p. L120-L123.
38. Yoo, E.J., et al., *Large reversible Li storage of graphene nanosheet families for use in rechargeable lithium ion batteries*. Nano Lett, 2008. 8(8): p. 2277-2282.

39. Hass, J., W. De Heer, and E. Conrad, *The growth and morphology of epitaxial multilayer graphene*. Journal of Physics: Condensed Matter, 2008. 20(32): p. 323202.
40. Schedin, F., et al., *Detection of individual gas molecules adsorbed on graphene*. Nat Mater, 2007. 6(9): p. 652-655.
41. Maurin, G., et al., *Electrochemical intercalation of lithium into multiwall carbon nanotubes*. Chemical physics letters, 1999. 312(1): p. 14-18.
42. Maurin, G., et al., *Lithium doping of multiwalled carbon nanotubes produced by catalytic decomposition*. Nano Lett, 2001. 1(2): p. 75-79.
43. Frackowiak, E., et al., *Electrochemical storage of lithium in multiwalled carbon nanotubes*. Carbon, 1999. 37(1): p. 61-69.
44. Ishihara, T., et al., *Effects of synthesis condition of graphitic nanocarbon tube on anodic property of Li-ion rechargeable battery*. Journal of Power Sources, 2001. 97-98(0): p. 129-132.
45. Claye, A.S., et al., *Solid-State Electrochemistry of the Li Single Wall Carbon Nanotube System*. Journal of The Electrochemical Society, 2000. 147(8): p. 2845-2852.
46. Gao, B., et al., *Electrochemical intercalation of single-walled carbon nanotubes with lithium*. Chemical physics letters, 1999. 307(3): p. 153-157.
47. Gao, B., et al., *Enhanced saturation lithium composition in ball-milled single-walled carbon nanotubes*. Chemical physics letters, 2000. 327(1): p. 69-75.
48. Kar, T., J. Pattanayak, and S. Scheiner, *Insertion of lithium ions into carbon nanotubes: an ab initio study*. The Journal of Physical Chemistry A, 2001. 105(45): p. 10397-10403.
49. Zhou, Z., et al., *Do composite single-walled nanotubes have enhanced capability for lithium storage?* Chemistry of Materials, 2005. 17(5): p. 992-1000.
50. Dubot, P. and P. Cenedese, *Modeling of molecular hydrogen and lithium adsorption on single-wall carbon nanotubes*. Physical Review B, 2001. 63(24): p. 241402.
51. Shimoda, H., et al., *Lithium intercalation into opened single-wall carbon nanotubes: storage capacity and electronic properties*. Physical Review Letters, 2001. 88(1): p. 15502.
52. Geim, A.K. and K.S. Novoselov, *The rise of graphene*. Nat Mater, 2007. 6(3): p. 183-191.

53. Abouimrane, A., et al., *Non-annealed graphene paper as a binder-free anode for lithium-ion batteries*. The Journal of Physical Chemistry C, 2010. 114(29): p. 12800-12804.
54. Kim, H., et al., *Highly reversible  $\text{Co}_3\text{O}_4$ /graphene hybrid anode for lithium rechargeable batteries*. Carbon, 2011. 49(1): p. 326-332.
55. Wu, Z.S., et al., *Graphene anchored with  $\text{Co}_3\text{O}_4$  nanoparticles as anode of lithium ion batteries with enhanced reversible capacity and cyclic performance*. ACS Nano, 2010. 4(6): p. 3187-3194.
56. Choi, D., et al., *Li-ion batteries from  $\text{LiFePO}_4$  cathode and anatase/graphene composite anode for stationary energy storage*. Electrochemistry Communications, 2010. 12(3): p. 378-381.
57. Yao, J., et al., *In situ chemical synthesis of  $\text{SnO}_2$ -graphene nanocomposite as anode materials for lithium-ion batteries*. Electrochemistry Communications, 2009. 11(10): p. 1849-1852.
58. Wang, H., et al.,  *$\text{Mn}_3\text{O}_4$ -Graphene Hybrid as a High Capacity Anode Material for Lithium Ion Batteries*. arXiv preprint arXiv:1009.3923, 2010.
59. Lee, J.K., et al., *Silicon nanoparticles-graphene paper composites for Li ion battery anodes*. Chemical Communications, 2010. 46(12): p. 2025-2027.
60. Zhou, G., et al., *Graphene-wrapped  $\text{Fe}_3\text{O}_4$  anode material with improved reversible capacity and cyclic stability for lithium ion batteries*. Chemistry of Materials, 2010. 22(18): p. 5306-5313.
61. Courtney, I.A. and J. Dahn, *Electrochemical and In Situ X-Ray Diffraction Studies of the Reaction of Lithium with Tin Oxide Composites*. Journal of The Electrochemical Society, 1997. 144(6): p. 2045-2052.
62. Liu, W., et al., *Studies of Stannic Oxide as an Anode Material for Lithium-Ion Batteries*. Journal of The Electrochemical Society, 1998. 145(1): p. 59-62.
63. Brousse, T., et al., *Composite negative electrodes for lithium ion cells*. Solid state ionics, 1998. 113: p. 51-56.

64. Idota, Y., et al., *Tin-based amorphous oxide: A high-capacity lithium-ion-storage material*. Science, 1997. 276(5317): p. 1395-1397.
65. Belliard, F., P. Connor, and J. Irvine, *Novel tin oxide-based anodes for Li-ion batteries*. Solid state ionics, 2000. 135(1): p. 163-167.
66. Belliard, F. and J. Irvine, *Electrochemical performance of ball-milled ZnO–SnO<sub>2</sub> systems as anodes in lithium-ion battery*. Journal of Power Sources, 2001. 97: p. 219-222.
67. Shenouda, A.Y. and H.K. Liu, *Studies on electrochemical behaviour of zinc-doped LiFePO<sub>4</sub> for lithium battery positive electrode*. Journal of Alloys and Compounds, 2009. 477(1): p. 498-503.
68. Liu, J., et al., *Carbon/ZnO nanorod array electrode with significantly improved lithium storage capability*. The Journal of Physical Chemistry C, 2009. 113(13): p. 5336-5339.
69. Liu, B., et al., *Hierarchical Three-Dimensional ZnCo<sub>2</sub>O<sub>4</sub> Nanowire Arrays/Carbon Cloth Anodes for a Novel Class of High-Performance Flexible Lithium-Ion Batteries*. Nano Lett, 2012. 12(6): p. 3005-3011.
70. Egashira, M., et al., *Properties of containing Sn nanoparticles activated carbon fiber for a negative electrode in lithium batteries*. Journal of Power Sources, 2002. 107(1): p. 56-60.
71. Halper, M.S. and J.C. Ellenbogen, *Supercapacitors: A brief overview*. Report No. MP 05W0000272, The MITRE Corporation, McLean, Virginia, 2006.
72. Albina, A., et al., *Influence of carbonaceous electrodes on capacitance and breakdown voltage for hybrid capacitor*. Microelectronics Journal, 2007. 38(4): p. 642-648.
73. M. Lanagan, T.S., B. Rangarajan, C. Pantano, and S. Conzone, *Glass Based Dielectrics for High Temperature Capacitors*. Proc. of the IMAPS High Temperature Electronics Conf., 2008. Albuquerque NM,: p. 78-83.
74. Slenes, K.M., et al., *Pulse power capability of high energy density capacitors based on a new dielectric material*. Magnetics, IEEE Transactions on, 2001. 37(1): p. 324-327.

75. Huebner, W., et al. *High breakdown strength, multilayer ceramics for compact pulsed power applications*. in *Pulsed Power Conference, 1999. Digest of Technical Papers. 12th IEEE International*. 1999. IEEE.
76. Michalczyk, P. and M. Bramouille, *Ultimate properties of the polypropylene film for energy storage capacitors*. *Magnetics, IEEE Transactions on*, 2003. 39(1): p. 362-365.
77. Nalwa, H.S., *Handbook of Low and High Dielectric Constant Materials and Their Applications, Two-Volume Set* 1999: Academic Press.
78. Rabuffi, M. and G. Picci, *Status quo and future prospects for metallized polypropylene energy storage capacitors*. *Plasma Science, IEEE Transactions on*, 2002. 30(5): p. 1939-1942.
79. Reed, C. and S. Cichanowskil, *The fundamentals of aging in HV polymer-film capacitors*. *Dielectrics and Electrical Insulation, IEEE Transactions on*, 1994. 1(5): p. 904-922.
80. McPherson, J.W., et al., *Trends in the ultimate breakdown strength of high dielectric-constant materials*. *Electron Devices, IEEE Transactions on*, 2003. 50(8): p. 1771-1778.
81. Fang, H.-B., et al., *Fabrication and performance of MEMS-based piezoelectric power generator for vibration energy harvesting*. *Microelectronics Journal*, 2006. 37(11): p. 1280-1284.
82. Sodano, H.A., D.J. Inman, and G. Park, *Generation and Storage of Electricity from Power Harvesting Devices*. *Journal of Intelligent Material Systems and Structures*, 2005. 16(1): p. 67-75.
83. Sodano, H.A., D.J. Inman, and G. Park, *Comparison of Piezoelectric Energy Harvesting Devices for Recharging Batteries*. *Journal of Intelligent Material Systems and Structures*, 2005. 16(10): p. 799-807.
84. Lu, X., et al., *Large-Scale Synthesis of Necklace-Like Single-Crystalline PbTiO<sub>3</sub> Nanowires*. *Macromol Rapid Commun*, 2006. 27(1): p. 76-80.
85. Huang, M.H., et al., *Room-Temperature Ultraviolet Nanowire Nanolasers*. *Science*, 2001. 292(5523): p. 1897-1899.
86. Thurn-Albrecht, T., et al., *Ultrahigh-Density Nanowire Arrays Grown in Self-Assembled Diblock Copolymer Templates*. *Science*, 2000. 290(5499): p. 2126-2129.



87. Bockrath, M., et al., *Resonant Electron Scattering by Defects in Single-Walled Carbon Nanotubes*. Science, 2001. 291(5502): p. 283-285.
88. Yang, J., M. Winter, and J. Besenhard, *Small particle size multiphase Li-alloy anodes for lithium-ionbatteries*. Solid state ionics, 1996. 90(1): p. 281-287.
89. Yang, J., et al., *SnSb<sub>x</sub>-based composite electrodes for lithium ion cells*. Solid state ionics, 2000. 135(1): p. 175-180.
90. Li, N., C.R. Martin, and B. Scrosati, *A High-Rate, High-Capacity, Nanostructured Tin Oxide Electrode*. Electrochemical and Solid-State Letters, 2000. 3(7): p. 316-318.
91. Jagadish, C. and S.J. Pearton, *Zinc Oxide Bulk, Thin Films and Nanostructures*. Elsevier, 2006.
92. Heo, Y.W., et al., *ZnO nanowire growth and devices*. Materials Science and Engineering: R: Reports, 2004. 47(1–2): p. 1-47.
93. Wang, Z.L., *Splendid one-dimensional nanostructures of zinc oxide: a new nanomaterial family for nanotechnology*. ACS Nano, 2008. 2(10): p. 1987-92.
94. Pan, Z.W., Z.R. Dai, and Z.L. Wang, *Nanobelts of semiconducting oxides*. Science, 2001. 291(5510): p. 1947-9.
95. Fan, Z. and J.G. Lu, *Zinc oxide nanostructures: synthesis and properties*. J Nanosci Nanotechnol, 2005. 5(10): p. 1561-73.
96. Dal Corso, A., et al., *Ab initio study of piezoelectricity and spontaneous polarization in ZnO*. Physical Review B, 1994. 50(15): p. 10715-10721.
97. Wang, Z.L., *Zinc oxide nanostructures: growth, properties and applications* Journal of Physics: Condensed Matter, 2004 Volume 16 (Issue 25): p. R829–R858.
98. Wang, Z.L. and J. Song, *Piezoelectric nanogenerators based on zinc oxide nanowire arrays*. Science, 2006. 312(5771): p. 242-6.
99. Lu, M.P., et al., *Piezoelectric nanogenerator using p-type ZnO nanowire arrays*. Nano Lett, 2009. 9(3): p. 1223-7.
100. Gao, P.X., et al., *Nanowire Piezoelectric Nanogenerators on Plastic Substrates as Flexible Power Sources for Nanodevices*. Advanced Materials, 2007. 19(1): p. 67-72.

101. Greene, L.E., et al., *Low-temperature wafer-scale production of ZnO nanowire arrays*. Angew Chem Int Ed Engl, 2003. 42(26): p. 3031-4.
102. Thostenson, E.T., et al., *Carbon nanotube/carbon fiber hybrid multiscale composites*. Journal of Applied Physics, 2002. 91(9): p. 6034-6037.
103. Tseng, Y.K., et al., *Characterization and Field-Emission Properties of Needle-like Zinc Oxide Nanowires Grown Vertically on Conductive Zinc Oxide Films*. Advanced Functional Materials, 2003. 13(10): p. 811-814.
104. Huang, M.H., et al., *Catalytic Growth of Zinc Oxide Nanowires by Vapor Transport*. Advanced Materials, 2001. 13(2): p. 113-116.
105. Jeong, J.S. and J.Y. Lee, *Investigation of initial growth of ZnO nanowires and their growth mechanism*. Nanotechnology, 2010. 21(47): p. 475603.
106. Yu, D., et al., *ZnO Nanowires Synthesized by Vapor Phase Transport Deposition on Transparent Oxide Substrates*. Nanoscale Res Lett, 2010. 5(8): p. 1333-1339.
107. Lin, Y., G. Ehlert, and H.A. Sodano, *Increased Interface Strength in Carbon Fiber Composites through a ZnO Nanowire Interphase*. Advanced Functional Materials, 2009. 19(16): p. 2654-2660.
108. Luo, L., B.D. Sosnowchik, and L. Lin, *Room temperature fast synthesis of zinc oxide nanowires by inductive heating*. Applied Physics Letters, 2007. 90(9): p. 093101-3.
109. Greene, L.E., et al., *Solution-grown zinc oxide nanowires*. Inorg Chem, 2006. 45(19): p. 7535-43.
110. Ko, S.H., et al., *Nanoforest of hydrothermally grown hierarchical ZnO nanowires for a high efficiency dye-sensitized solar cell*. Nano Lett, 2011. 11(2): p. 666-671.
111. Xu, C., et al., *Preferential growth of long ZnO nanowire array and its application in dye-sensitized solar cells*. The Journal of Physical Chemistry C, 2009. 114(1): p. 125-129.
112. Qiu, J., et al., *Solution-derived 40  $\mu\text{m}$  vertically aligned ZnO nanowire arrays as photoelectrodes in dye-sensitized solar cells*. Nanotechnology, 2010. 21(19): p. 195602.
113. Law, M., et al., *Nanowire dye-sensitized solar cells*. Nat Mater, 2005. 4(6): p. 455-9.

114. Lewis, T., *Interfaces are the dominant feature of dielectrics at the nanometric level*. Dielectrics and Electrical Insulation, IEEE Transactions on, 2004. 11(5): p. 739-753.
115. Lewis, T., *Interfaces: nanometric dielectrics*. Journal of Physics D: Applied Physics, 2005. 38(2): p. 202.
116. Mao, Y.P., et al., *Size-dependences of the dielectric and ferroelectric properties of BaTiO<sub>3</sub>/polyvinylidene fluoride nanocomposites*. Journal of Applied Physics, 2010. 108(1): p. 014102-6.
117. Mohamadi, S., *Preparation and Characterization of PVDF/PMMA/Graphene Polymer Blend Nanocomposites by Using ATR-FTIR Technique*.
118. Raju, G.G., *Dielectrics in electric fields*. Vol. 19. 2003: CRC.
119. Gregorio, R. and E. Ueno, *Effect of crystalline phase, orientation and temperature on the dielectric properties of poly (vinylidene fluoride)(PVDF)*. Journal of materials science, 1999. 34(18): p. 4489-4500.
120. Hu, Y., et al., *Preparation of PbTiO<sub>3</sub> nanoceramics based on hydrothermal nanopowders and characterization of their electrical properties*. Materials Chemistry and Physics, 2010. 121(1–2): p. 10-13.
121. Shirane, G., S. Hoshino, and K. Suzuki, *X-Ray Study of the Phase Transition in Lead Titanate*. Physical Review, 1950. 80(6): p. 1105-1106.
122. Haun, M.J., et al., *Thermodynamic theory of PbTiO<sub>3</sub>*. Journal of Applied Physics, 1987. 62(8): p. 3331-3338.
123. Cohen, R.E., *Origin of ferroelectricity in perovskite oxides*. Nature, 1992. 358(6382): p. 136-138.
124. Fong, D.D., et al., *Ferroelectricity in Ultrathin Perovskite Films*. Science, 2004. 304(5677): p. 1650-1653.
125. Catalan, G., et al., *Polar Domains in Lead Titanate Films under Tensile Strain*. Physical Review Letters, 2006. 96(12): p. 127602.

126. Wang, et al., *Self-Assembled Growth of PbTiO<sub>3</sub> Nanoparticles into Microspheres and Bur-like Structures*. Chemistry of Materials, 2007. 19(9): p. 2213-2221.
127. Yang, W.-D., *PZT/PLZT ceramics prepared by hydrolysis and condensation of acetate precursors*. Ceramics International, 2001. 27(4): p. 373-384.
128. Shirane, G., S. Hoshino, and K. Suzuki, *X-ray study of the phase transition in lead titanate*. Physical Review, 1950. 80(6): p. 1105.
129. Yu.N. Venevtsev, G.S.Z., S.P. Solov'ev, V.V. Ivanova, Sov. Phys. Crystallogr., 1959. 4: p. 235.
130. Hernandez, B.A., et al., *Sol–Gel Template Synthesis and Characterization of BaTiO<sub>3</sub> and PbTiO<sub>3</sub> Nanotubes*. Chemistry of Materials, 2002. 14(2): p. 480-482.
131. Cai, Z., et al., *Morphology-Controlled Synthesis of Lead Titanate Powders*. Inorg Chem, 2007. 46(18): p. 7423-7427.
132. Hsu, M.C., et al., *Template synthesis and characterization of PbTiO<sub>3</sub> nanowire arrays from aqueous solution*. Journal of Solid State Chemistry, 2006. 179(5): p. 1421-1425.
133. Deng, Y., et al., *Synthesis and characterization of single-crystal PbTiO<sub>3</sub> nanorods*. Materials Letters, 2005. 59(26): p. 3272-3275.
134. Liu, L., et al., *Synthesis, characterization, photoluminescence and ferroelectric properties of PbTiO<sub>3</sub> nanotube arrays*. Materials Science and Engineering: B, 2008. 149(1): p. 41-46.
135. Deng, H., Y. Qiu, and S. Yang, *General surfactant-free synthesis of MTiO<sub>3</sub> (M = Ba, Sr, Pb) perovskite nanostrips*. Journal of Materials Chemistry, 2009. 19(7): p. 976-982.
136. Yu, G., et al., *Crystallization process and microstructure of sol–gel derived Pb<sub>0.9</sub>La<sub>0.1</sub>Ti<sub>0.875</sub>O<sub>3</sub> fine fibers with a novel heat-treatment process*. Solid State Sciences, 2008. 10(7): p. 859-863.
137. Luo, Y., et al., *Nanoshell tubes of ferroelectric lead zirconate titanate and barium titanate*. Applied Physics Letters, 2003. 83(3): p. 440-442.
138. Zhang, X.Y., et al., *Synthesis and piezoresponse of highly ordered Pb(Zr<sub>0.53</sub>Ti<sub>0.47</sub>)O<sub>3</sub> nanowire arrays*. Applied Physics Letters, 2004. 85(18): p. 4190-4192.

139. Limmer, S.J., et al., *Electrophoretic Growth of Lead Zirconate Titanate Nanorods*. Advanced Materials, 2001. 13(16): p. 1269-1272.
140. Hishinuma, A., et al., *Formation of silicon dioxide films in acidic solutions*. Applied Surface Science, 1991. 48–49(0): p. 405-408.
141. Yamada, T., et al., *Synchrotron X-ray diffraction study on a single nanowire of PX-phase lead titanate*. Journal of the European Ceramic Society, 2010. 30(15): p. 3259-3262.
142. Cheng, H., et al., *Hydrothermal Synthesis of Acicular Lead Titanate Fine Powders*. Journal of the American Ceramic Society, 1992. 75(5): p. 1123-1128.
143. M. Suzuki, S.U., H. Masuya, and H. Tamura, *Hydrothermal Synthesis of Lead Titanate Fine Powders*. American Ceramic Society, 1998. 1(Ceramic Powder Science II): p. 163–70.
144. Zhu, X., et al., *Perovskite Nanoparticles and Nanowires: Microwave–Hydrothermal Synthesis and Structural Characterization by High-Resolution Transmission Electron Microscopy*. Journal of the American Ceramic Society, 2008. 91(8): p. 2683-2689.
145. Morita, T., et al., *Ferroelectric properties of an epitaxial lead zirconate titanate thin film deposited by a hydrothermal method below the Curie temperature*. Applied Physics Letters, 2004. 84(25): p. 5094-5096.
146. Hu, Y., et al., *Photoluminescence and Raman scattering studies on PbTiO<sub>3</sub> nanowires fabricated by hydrothermal method at low temperature*. Applied Physics Letters, 2006. 88(19): p. 193120-3.
147. Wang, Y., et al., *Preparation of single-crystal PbTiO<sub>3</sub> nanorods by phase transformation from Pb<sub>2</sub>Ti<sub>2</sub>O<sub>6</sub> nanorods*. Journal of Alloys and Compounds, 2009. 481(1–2): p. L27-L30.
148. Camargo, E.R., et al., *Phase evolution of lead titanate from its amorphous precursor synthesized by the OPM wet-chemical route*. Journal of Solid State Chemistry, 2004. 177(6): p. 1994-2001.
149. Marcano, D.C., et al., *Improved synthesis of graphene oxide*. ACS Nano, 2010. 4(8): p. 4806.
150. Tang, H., et al., *Nanocomposites with increased energy density through high aspect ratio PZT nanowires*. Nanotechnology, 2011. 22(1): p. 015702.

151. Wang, J., C.S. Sandu, and N. Setter, *Large-scale fabrication of titanium-rich perovskite PZT submicro/nano wires and their electromechanical properties*. IEEE Trans Ultrason Ferroelectr Freq Control, 2009. 56(9): p. 1813-9.
152. D149-09, A.S., *Standard Test Method for Dielectric Breakdown Voltage and Dielectric Strength of Solid Electrical Insulating Materials at Commercial Power Frequencies*, in *ASTM International* 2009.
153. Cai, Z., et al., *Morphology-controlled synthesis of lead titanate powders*. Inorg Chem, 2007. 46(18): p. 7423-7.
154. Varadan, V.V., et al. *Measurement of all the elastic and dielectric constants of poled PVDF films*. in *Ultrasonics Symposium, 1989. Proceedings., IEEE 1989*. 1989.

## **Curriculum Vita**

Md Ashiqur Rahaman Khan was born on July 31 of 1988 in Dhaka, Bangladesh. He started his bachelor of science in Mechanical Engineering in year 2006 and graduated successfully in 2010. He got himself admitted at The University of Texas at El Paso in fall 2011. He was awarded Graduate Teaching Assistant and later Graduate Research Assistant scholarship. He conducted research on nanocomposite materials for energy storage devices under Dr. Yirong Lin's supervision and published one journal paper and six conference papers during his one and five months of master's degree.

Permanent address: Village-Satni, P. O.-Satni-Dhekra, Thana-Adamdeghi,  
District-Bogra Santahar, Bangladesh

This thesis report was typed by Md Ashiqur Rahaman Khan.